UNIVERSIDAD COMPLUTENSE DE MADRID

FACULTAD DE CIENCIAS FÍSICAS

DEPARTAMENTO DE FÍSICA DE LA TIERRA Y ASTROFÍSICA

TESIS DOCTORAL

Sudden Stratospheric Warmings and the Brewer-Dobson Circulation: diagnostics and interactions

Calentamientos Súbitos Estratosféricos y la Circulación de Brewer-Dobson: diagnósticos e interacciones

Presentada por
Froila María Palmeiro Núñez

Directores
David Barriopedro Cepero
Natalia Calvo Fernández

Madrid, 2017

Dedicado a

mi familia

Agradecimientos (Acnowledgements)

En primer lugar, agradezco a mis directores Natalia y David el haberme guiado los últimos años. A Natalia por tu esfuerzo y por poder siempre con todo, eres un ejemplo para muchas. A David por tu inagotable paciencia y estar siempre dispuesto a ayudarme. Juntos os habéis convertido en unos Doktoreltern fantásticos. Ricardo, gracias por tus lecciones y sabios consejos. Siempre me acordaré de los tres por haberme regalado esta oportunidad que, sin duda, ha cambiado mi vida y mi forma de entenderla a partir de ahora.

Muchas gracias Rolando por tu cercanía, por trabajar conmigo antes de conocerme y seguir haciéndolo después. Por ser más que un supervisor durante mi estancia en NCAR y preocuparte siempre por mi bienestar, eres un gran maestro. Asimismo, gracias Agustín por acomodarme en mis primeros días de estancia, amenizarme las comidas y los cafés y ser tan amable conmigo.

I am also very grateful to the people in NCAR and GEOMAR that hosted my visits. Special thanks to Katja Matthes for supervising my work during my stay in Kiel and to the whole "Physics of the Atmosphere" research team, for making me feel as just one more, danke. Bernat, por haber sido un gran apoyo, Merci.

Contents

Summary

Introduction

The polar winter stratosphere is dominated by strong thermally-driven westerly winds (Andrews et al. 1987). Every two years on average (Charlton and Polvani 2007), this polar vortex is disrupted by a Sudden Stratospheric Warming (SSW), whereby the polar stratosphere warms rapidly (McInturff 1978). SSWs are related with enhanced planetary wave (PW) activity reaching the polar stratosphere and depositing momentum to the zonal mean flow (Matsuno 1971). Also wave-driven, the Brewer-Dobson Circulation (BDC) is responsible for the equator-to-pole mass transport (e.g., Andrews et al. 1987), specially its deep branch, in the middle and upper stratosphere (Plumb 2002). SSWs and BDC are the most illustrative examples of the polar stratospheric variability. However, there are still open questions regarding their underlying processes, mutual interactions and the expected trends under climate change scenarios. Some of them are explored in this thesis.

Objectives

1. To assess the discrepancies in SSW frequencies and signatures across different SSW definitions.

2. To understand how new model developments, and in particular the Turbulent Mountain Stress (TMS) parameterization influences SSW occurrence.

3. To explore the relationship between SSWs and the polar downwelling of the deep

branch of the BDC.

4. To investigate the driving processes of the BDC and its future trends under climate change scenarios.

Results

This thesis is presented in four chapters with the following results:

1. Eight SSW definitions were applied to reanalysis data for the 1958-2014 period. Dynamical benchmarks were constructed to compare the climatological characteristics of the SSWs across definitions. The comparison showed that the stratospheric signatures of SSWs are not sensitive to the detection method, and case-to-case variability among SSWs is larger than the inter-method spread. However, the decadal distribution of SSWs is method-dependent, and only the traditional definition based on the wind reversal at 60°N displays a minimum occurrence in the 1990s. The largest differences among definitions are due to the detection of minor warmings, which show weaker stratosphere-troposphere coupling and non-robust surface signals. Conversely, major warmings, which are commonly detected by most definitions, show consistent surface responses during the month following SSWs. These results are robust for three analyzed reanalyses.

2. Two historical simulations, TMS-on and TMS-off, of the Whole Atmosphere Community Climate Model (WACCM4) differing only in the TMS implementation were compared to understand the differences in SSW frequency between them. PW drag and Orographic Gravity Wave drag (OGWD) in the northern stratosphere are found to vary to compensate each other, so that the total forcing remains unchanged. In early winter, when the surface winds are stronger in TMS-off, the OGWD increases at mid and high latitudes of the stratosphere, compared to TMS-on. Then, by compensation, there is less PW forcing at these latitudes to perturb the polar vortex and trigger SSWs. In late winter (March), when the OGWD is reduced in TMS-off, the

2

PW forcing increases and reaches similar values in both simulations, consistent with their comparable frequencies of SSWs.

3. The BDC and SSW relationship was analyzed using a fixed-GHGs and increasing GHGs (RCP8.5) simulations of WACCM4 for 1955-2099. Composites of the BDC and the Eliassen-Palm (EP) flux reveal that enhanced PW convergence induces an acceleration of the polar downwelling of the deep branch of the BDC during the month before SSWs. Conversely, PW propagation is inhibited and the BDC decelerates for several weeks after SSW occurrence. On the other hand, March SSWs and early (March) SFWs (referred to as March warmings) lead to an anticipated winter-to-summer transition of the BDC. In the RCP8.5, the BDC transition to a summer regime is delayed, but winters with March warmings show not delay in such transition. Consequently, the net effect of March warmings becomes stronger in the future.

4. The climatology (1960-2005) and trends (2005-2100) of the BDC in three climate change scenarios (RCP2.6, RCP4.5 and RCP8.5) are studied using WACCM4. The shallow and the less investigated deep branch of the BDC are similar to Reanalysis (Seviour et al. 2012). Both branches accelerate in response to increasing greenhouse gases, and the tropical upwelling of the deep branch displaces upward to the stratopause. Analysis of the forcings reveals that PWs dominate the climatological-mean tropical upwelling in the lower and upper stratosphere as well as the trends in the lower stratosphere. The role of Gravity Waves (GWs) associated with fronts becomes dominant in the trends of the upper stratosphere. The strengthening and upward displacement of the subtropical tropospheric jets in the future inhibit the propagation of the westerly part of the spectrum of frontal GWs into the upper stratosphere, so that the deep branch of the BDC accelerates.

Conclusions

1. The SSW signatures in the stratosphere are captured similarly by all methods but there are differences in the stratosphere-troposphere coupling when minor SSWs are considered. SSW detection should include a range of latitudes around 60°N.

2. The underestimation of SSWs in TMS-off is associated with compensation between PWs and GWs, with weaker PW forcing in response to stronger OGWD. In TMS-on, OGWD diminishes, thus enhanced PW drag occurs in the stratosphere and SSWs are more likely.

3. The deep branch of the BDC accelerates before and decelerates after SSWs. The winter-to-summer transition of the BDC is modulated by the timing of SSWs and early SFWs, and is projected to be delayed in the future.

4. There is an upward expansion of the tropical upwelling as a consequence of the BDC acceleration under climate change in WACCM4. Frontal GWs dominate this trend in the BDC deep branch, and their changes are related to the enhancement of the subtropical jets.

Resumen

Introducción

La estratosfera polar de invierno está dominada por vientos del oeste forzados térmicamente (Andrews et al. 1987). Cada dos años aproximadamente, este vórtice polar se ve perturbado por un calentamiento súbito estratosférico (SSW, del inglés) (Charlton and Polvani 2007) que produce un rápido aumento de la temperatura polar (McInturff 1978). Los SSWs se relacionan con un aumento de actividad de ondas planetarias (PW, del inglés) en la estratosfera polar que ceden momento al flujo medio (Matsuno 1971). La rama profunda de la circulación de Brewer-Dobson (BDC, del inglés) en la media y alta estratosfera (Plumb 2002), también forzada por ondas, es responsable del transporte de masa entre el ecuador y el polo (e.g., Andrews et al. 1987). Ambos fenómenos suponen los ejemplos más ilustrativos de la variabilidad de la estratosfera polar. Sin embargo, todavía hay preguntas abiertas sobre los procesos que los modulan, sus interacciones y sus posibles cambios en un clima futuro. Algunas de estas cuestiones son exploradas en esta tesis.

Objetivos

1. Evaluar las características de los SSWs y su robustez al aplicar diferentes definiciones de SSWs.

2. Entender cómo la parametrización TMS (del inglés, Turbulent Mountain Stress) afecta a la ocurrencia de SSWs en el modelo Whole Atmosphere Community Cli-

mate Model (WACCM4).

3. Investigar la relación entre SSWs y la rama profunda polar de la BDC.

4. Caracterizar la climatología de la BDC en WACCM4 e investigar sus cambios en el futuro en diferentes escenarios de cambio climático.

Resultados

La tesis se presenta en cuatro capítulos con los siguientes resultados:

1. Utilizando datos de reanálisis y ocho definiciones distintas de SSWs en el período 1958-2014, se han comparado sus distintas climatologías asi como un conjunto de diagnósticos. Los resultados indican que las características estratosféricas de los SSWs son insensibles al método, siendo la variabilidad entre casos es mayor que entre métodos. Sin embargo, la distribución decadal de SSWs sí depende del método, y solo cuando se usa la inversión del viento en 60°N aparece un mínimo en la década de 1990. Las principales diferencias entre definiciones se deben a los SSW menores, que muestran un acoplamiento estratosfera-troposfera más débil y señales poco robustas en superficie. Por el contrario, los SSW mayores, que detectan la mayoría de métodos, presentan respuestas consistentes en superficie durante un mes después del SSW. Los resultados son coherentes en los tres reanálisis utilizados.

2. Se han comparado dos simulaciones históricas con (TMS-on) y sin (TMS-off) la parametrización TMS de WACCM4 para analizar los mecanismos que explican sus diferencias en la frecuencia de SSWs a principios del invierno. Se ha constatado que los forzamientos de PWs y ondas de gravedad orográficas (OGWD, del inglés) se compensan el uno con el otro de forma que el forzamiento total no varía. Al principio del invierno, cuando los vientos en superficie son más fuertes en TMS-off, hay más OGWD . Por compensación, se reduce el forzamiento de PWs en el vórtice y la probabilidad de generar SSWs. A finales de invierno, como el OGWD disminuye

en TMS-off, el forzamiento de PWs es similar en TMS-on y TMS-off, y las frecuencias de SSWs son comparables.

3. Se ha analizado la relación entre la BDC y los SSWs en simulaciones (1955-2099) de WACCM4 con y sin cambios en el forzamiento antropogénico. El análisis de la BDC y el flujo de Eliassen-Palm (EP) muestran que la convergencia de PWs antes del SSW induce una aceleración de la rama profunda de la BDC. Por el contrario, la propagación de PWs se inhibe y la BDC se debilita durante varias semanas después del SSW. Además, los calentamientos de marzo, que incluyen SSWs y calentamientos súbitos finales (SFWs, del inglés) tempranos adelantan la transición del invierno al verano de la BDC. Con un aumento del forzamiento antropogénico (RCP8.5), la transición de la BDC se retrasa, pero las fechas de transición durante los calentamientos de marzo no cambian, haciendo que su efecto neto aumente en el futuro.

4. Se ha estudiado la climatología (1960-2005) y tendencias (2005-2100) de la BDC en tres escenarios de cambio climático (RCP2.6, RCP4.5 y RCP8.5) con WACCM4. El modelo reproduce las ramas somera y profunda de la BDC de forma similar al Reanálisis. Como respuesta al aumento de gases de efecto invernadero, ambas ramas de la BDC se aceleran y el upwelling tropical de la rama profunda se eleva hacia la estratopausa. El análisis de forzamiento de ondas revela que la climatología del upwelling tropical en la baja y alta estratosfera está dominado por PWs, así como las tendencias en la baja estratosfera. Sin embargo, las ondas de gravedad (GWs, del inglés) asociadas a frentes dominan las tendencias de la alta estratosfera. El ascenso y fortalecimiento de los jets subtropicales en el futuro inhibe la propagación vertical de la parte occidental del espectro de las GWs, permitiendo que la rama profunda se acelere.

Conclusiones

1. Todos los métodos capturan de forma similar los rasgos estratosféricos de los SSWs, pero existen diferencias en el acoplamiento estratosfera-troposfera cuando se consideran SSW menores. La detección de SSWs debería incluir un rango de latitudes alrededor de 60°N.

2. La infraestimación de SSWs en TMS-off se asocia a una compensación entre PWs y GWs. Como en TMS-on el OGWD disminuye en la estratosfera, el forzamiento de PWs aumenta y los SSWs son más probables.

3. La rama profunda de la BDC se acelera antes de la ocurrencia de SSWs, y se debilita en la fase de recuperación del vórtice. La transición al verano de la BDC está modulada por los calentamientos de marzo, y se retrasa en el futuro.

4. Como consecuencia de la aceleración de la BDC bajo cambio climático, el upwelling tropical de la rama profunda se expande hacia la estratopausa. Los cambios en las FGWs dominan la tendencia en la rama profunda de la BDC, y se asocian al fortalecimiento de los jets subtropicales.

Chapter 1

Introduction

1.1   Background

The measurements of L. Teisserenc de Bort in 1896 based on paper balloons revealed an inversion of the temperature above 11 km. This was the beginning of the studies on the stratosphere. This layer extends from the isothermal tropopause ($\sim$10 km) up to stratopause ($\sim$50 km). Different from the troposphere, the temperature profile in the stratosphere rises with height. Given its temperature stratification, vertical motions are very slow compared to those in the troposphere and are limited to upwelling and down-welling regions located in the tropics and the poles, respectively.

The stratosphere contains 90% of the atmospheric ozone, while only 10% stays in the troposphere. This makes the stratosphere essential for life sustainability since ozone absorbs the incoming ultraviolet radiation from the Sun (e.g., van der Leun et al. 1995). On the other hand, it contains low concentrations of water vapor and only $\sim$15% of the total mass of the atmosphere, so that clouds are no commonly developed in the stratosphere, with the exception of polar stratospheric clouds (PSCs), which favor ozone depletion.

1.2 The winter stratosphere

Since there is no radiative heating over the pole during winter, the stratosphere cools, and a negative temperature gradient sets up between the tropics and high latitudes. Assuming the atmosphere in geostrophic and hydrostatic balance, the zonal-mean wind and temperature are balanced by the thermal wind relation in the steady-state state (Equation 1.1).

$$\frac{\partial u_g}{\partial z} = -\frac{R}{f \cdot H}\frac{\partial T}{\partial y} \qquad u_g = -\frac{1}{f}\frac{\partial Z}{\partial y} \qquad (1.1)$$

being Z the geopotential height, f the Coriolis parameter ($f = 2\Omega sin\phi$, where Ω is the Earth's angular velocity), R the specific gas constant and H the scale height. Thus, a westerly wind circulation is induced in the stratosphere due to the equator-to-pole temperature difference during the extended winter. The distribution of zonal-mean temperature and zonal-mean zonal wind is illustrated in Figure 1 in a latitude-altitude cross section for boreal (December-January-February, DJF) and austral (June-July-August, JJA) winters. In the winter hemisphere, westerly winds in the stratosphere extend from the subtropics to the pole, with the strongest winds located in the polar latitudes. This results in the stratospheric polar vortex or the so-called polar night jet, which dominates the circulation of the polar stratosphere in winter. The largest positive values of the wind in the stratosphere correspond to the vortex edge, which is located around 60° and extends from 20 km to 50 km approximately. The stratospheric polar vortex develops at the northernmost latitudes of the stratosphere during late fall, is maximum in midwinter, and persists until the next spring. In the summer hemisphere, the polar vortex is replaced by weak easterlies.

There are hemispheric differences in the polar vortex strength and variability that must be highlighted. Comparison between the boreal and austral winter in Figure 1 shows a stronger and colder polar vortex in the Southern Hemisphere (SH) than in the Northern Hemisphere (NH). For a more clear comparison, Figure 2 shows the seasonal cycle of the zonal-mean zonal wind at 10hPa averaged over the 50°-70° latitudinal belt of each hemisphere. The maximum strength of the polar vortex in the SH is more than twice than in the

10

NH (cf. blue lines in Figure 2). Stronger wind speeds in the Antarctic are consistent with the cold polar vortex, which is crucial for the formation of PSCs and ozone depletion, as will be discussed later in Section 1.4. Moreover, the transition to easterlies occurs earlier in the Arctic than in the Antarctic, resulting in a longer lifespan of the Antarctic polar vortex.
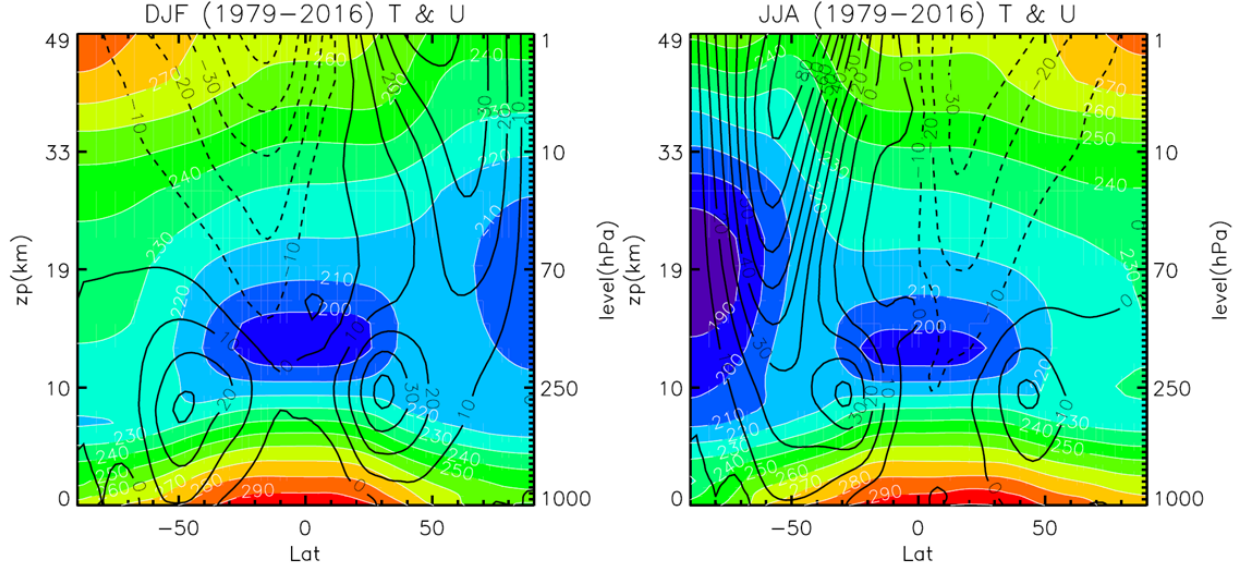
Figure 1: Zonal-mean temperature (shading) and zonal wind (contours) climatology from the [1]ERA-Interim reanalysis for the period 1979-2016 in DJF (left) and JJA (right). Shaded contour intervals are every 10 K and black contour intervals are every 10 ms^-1. Solid: eastward flow, dotted: westward flow.

The Artic vortex shows large variability on both intraseasonal and interannual time scales (cf. top and bottom panels of Figure 2). Interannual variability is associated with natural external forcings such as the solar cycle or volcanic eruptions (Chiodo et al. 2012), and also with internal variations of the Earth's climate such as the Quasi-Biennial Oscillation (QBO), El Niño-Southern Oscillation (ENSO) and their nonlinear interactions (e.g., Calvo et al. 2009). The observational record of the stratosphere is too short to isolate the statistical influence of some forcings. This is particularly true for the case of the 11-year solar cycle and volcanic eruptions as there are only stratospheric measurements for

---

[1]Interim European Centre for Medium-Range Weather forecasts Reanalysis (Dee et al. 2011): https://www.ecmwf.int/en/research/climate-reanalysis/era-interim

about three solar cycles and three major eruptions (Matthes et al. 2010, Mitchell et al. 2011). Even more, there is superposition of different forcings in the observational record, with two or more factors operating at the same time, such as warm ENSO years with easterly phases of the QBO, or volcanic eruptions with solar maxima (e.g., Chiodo et al. 2014). This aliasing effect makes difficult to isolate the stratospheric response to a single forcing. Moreover, several studies found that signals of combined factors are non-additive, showing strong nonlinear responses on the stratosphere (e.g., Calvo et al. 2009; Richter et al. 2011). All these aspects illustrate the complex challenge of understanding polar stratospheric variability.
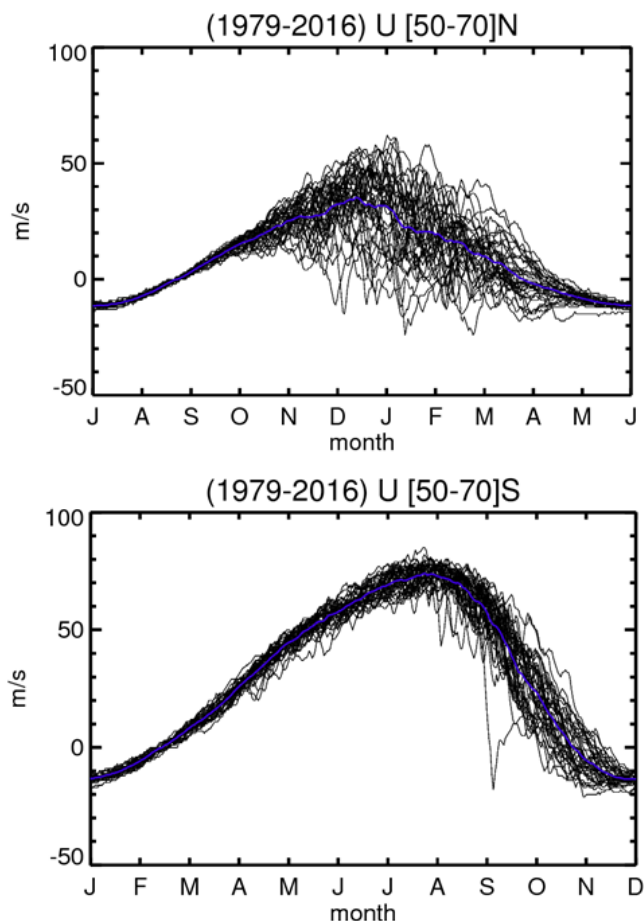
Figure 2: Time series of the daily zonal-mean zonal wind at 10 hPa in the NH (top) and the SH (bottom) averaged over 50°-70° latitudes. Black lines indicate daily values for each year of the 1979-2016 period from ERA-Interim and blue lines are the corresponding average.

On the other hand, Figure 2 also shows noticeable intraseasonal variability, which again is larger for the NH polar vortex than for its SH counterpart. The climatological spatial configuration of the two vortices can be compared in Figure 3, showing a more stable Antarctic polar vortex, with a stronger and less perturbed potential vorticity (PV) gradient (Figure 3b), compared to the Arctic one (Figure 3a). These differences are caused by the more pronounced large-scale topography and land-sea contrast in the NH, which lead to stronger tropospheric wave activity in the NH and enhanced upward wave propagation towards the stratosphere, where it can disturb the polar vortex from radiative equilibrium (e.g., Wexler 1959).
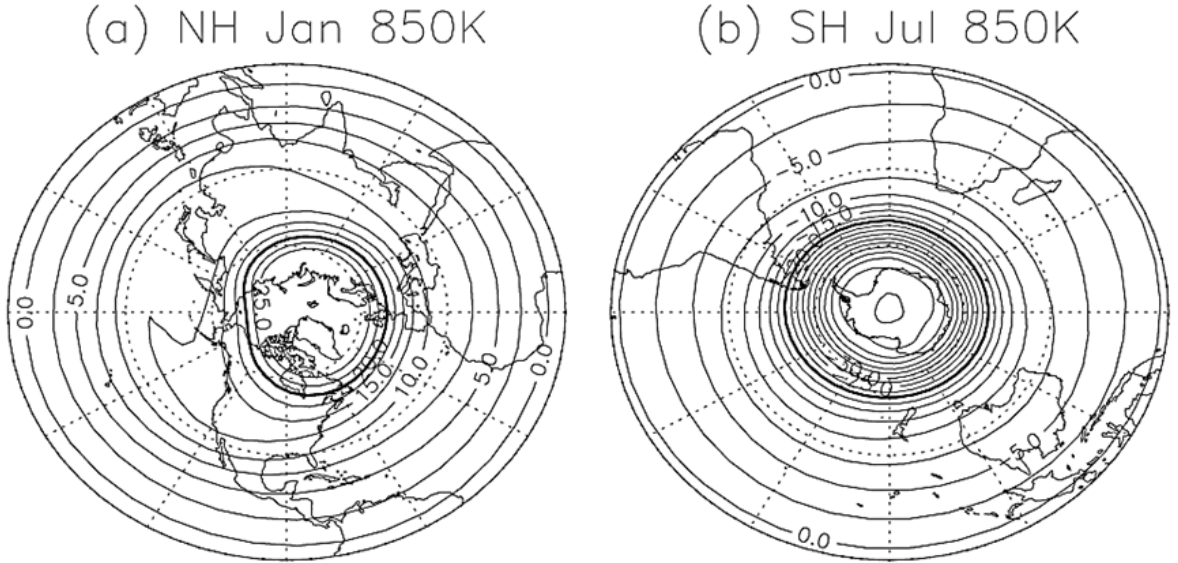
Figure 3: Climatological mean PV on the 850 K isentropic surface ($\sim$10 hPa) for NH in January (a) and SH in July (b). From Waugh and Polvani (2010)

1.3   Wave dynamics

The radiative time scales in the stratosphere are of the order of weeks, and hence its variability occurs on longer time scales than in the troposphere. However, under certain conditions, waves excited in the troposphere can propagate into the stratosphere in a few

days (e.g., Charney and Drazin 1961). Atmospheric waves are propagating disturbances resulting from a restoring force that acts to recover the balance over air parcels displaced from their equilibrium. Waves in the atmosphere can be classified depending on the restoring force. Particularly important for this thesis are Planetary Waves (PWs), induced by the poleward gradient of planetary vorticity, and Gravity Waves (GWs), generated by gravity or buoyancy. GWs are excited when air parcels are displaced vertically, usually due to the presence of obstacles as small-scale mountains (orographic GWs) or by frontal, convective systems or other instabilities (non-orographic GWs) (e.g., Fritts and Alexander 2003). The wave impact on the atmospheric flow is characterized by its angular momentum transfer, which is referred to as wave drag (Shepherd 1990). The sign of the wave drag is related to the phase speed of the waves relative to the mean flow. In this sense, PWs are always associated with a negative (westward) drag, while GWs can generate both, typically westward drag in winter and and eastward drag in summer.

Since the circulation in the stratosphere is zonally symmetric, it is usually characterized by a zonal mean $\overline{u}$, which results from the decomposition of the total field as: $u = \overline{u} + u'$, where the prime denotes the eddy components. Upward propagation of waves from the troposphere into the stratosphere is governed by the Charney-Drazin criterion (Equation 1.2; Charney and Drazin 1961):

$$0 < \overline{u} - c < U_c = \frac{\beta}{(k^2 + l^2) + f_0^2/4H^2N^2} \tag{1.2}$$

It states the conditions for upward propagation of waves with a certain phase speed (c) , where $\overline{u}$ is the background wind speed and U_c is the critical wind speed. This critical value is proportional to $\beta = \frac{\partial f}{\partial y}$, and depends on $f_0 = 2\Omega sin\phi_0$, the scale height (H), the buoyancy frequency (N) and the zonal and meridional wave numbers k and l. Rossby waves are mostly forced at the surface by static sources, and according to Eq. 1.2, stationary waves ($c = 0$) can only propagate in westerly winds ($\overline{u} > 0$) as long as they are weaker than the critical wind speed (U_c). This means that only large-scale Rossby waves

14

(zonal wavenumbers 1 - 3), also referred to as PWs, can propagate into the stratosphere in the winter hemisphere, while smaller-scale waves are filtered out at lower levels. Moreover, while propagation is favored in the NH, the strong westerlies of the SH winter prevent wave penetration and waves are often trapped vertically. This fact contributes to a more perturbed polar vortex in the NH, as shown in Figure 3.
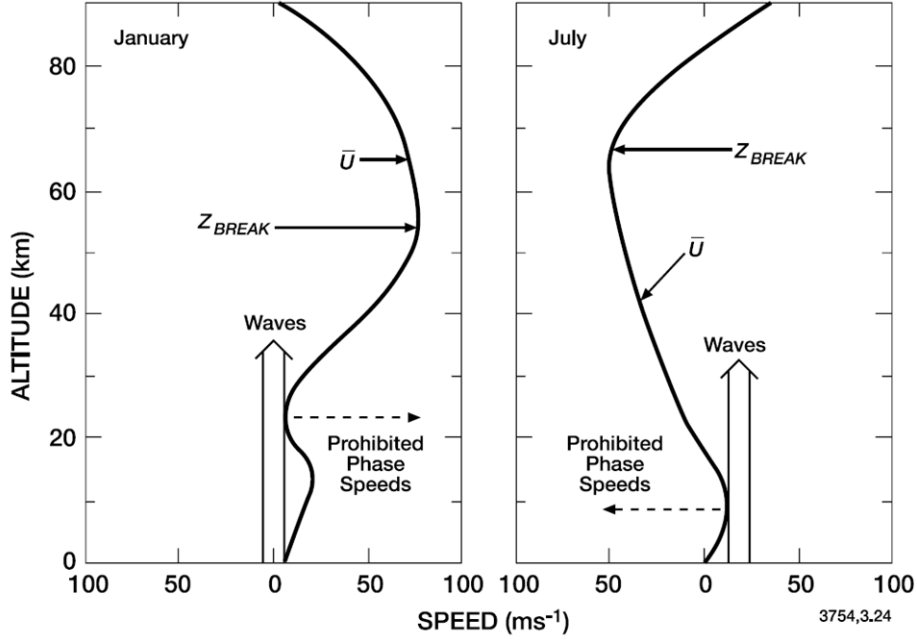
Figure 4: Approximated altitude profiles of the zonal-mean zonal wind in winter (left panel) and summer (right panel). The permitted phase speeds for the propagation of GWs and their breaking levels are also shown. From Brasseur and Solomon (2006).

Figure 4 illustrates the upward propagation of GWs in both hemispheres. At a certain altitude (called the critical level), the wave phase speed is equal to the zonal wind background, and the wave is absorbed by the mean flow. Otherwise, as they continue to move upwards, their amplitude grows as the inverse square of the density, and at some altitude they become convectively unstable and break (Brasseur and Solomon 2006). The role of GWs in the global momentum budget increases with altitude (as atmospheric density decreases and their amplitude increases) so their largest effects occur above the mesosphere (>50 km). Nevertheless, they can also play a role in the stratospheric circulation and the

PW propagation into the stratosphere, as it will be illustrated in this thesis.

In the atmosphere, the strength and distribution of the zonal-mean flow that governs wave propagation varies with latitude and height, Matsuno (1970) introduced the so-called refractive index to diagnose the characteristics of Rossby wave propagation. For a zonal wave number, k, the squared refractive index is given by:

$$n_k^2 = \frac{1}{a\overline{u}}\frac{\partial\overline{q}}{\partial\phi} - \frac{k^2}{a^2cos^2\phi} - \frac{f^2}{4N^2H^2} \tag{1.3}$$

where $\frac{\partial\overline{q}}{\partial\phi}$ is the latitudinal gradient of PV, which mostly depends on the zonal and vertical shear of u. Following Matsuno's interpretation, planetary waves tend to propagate to regions of high values of n^2 and be refracted away from regions of low n^2 values.

Similar to GWs, the amplitude of PWs increases exponentially as they propagate upwards, and when the phase velocity of the wave approaches to that of the background flow, wave breaking occurs. Then, propagation is prohibited close to critical surfaces (e.g., $c = \overline{u}$). When PWs reach those regions, they break transferring momentum to the zonal flow. Since PWs transfer westward momentum to the background westerlies their breaking acts to decelerate the mean flow in the stratosphere (Shepherd 2007). This feature was observed by McIntyre and Palmer (1983) as deformations in the PV contours. The regions where this occurs are referred to as the surf zone by analogy with waves on a shoreline. PW wave breaking also causes turbulence and mixes chemical constituents (Fritts and Alexander 2003).

1.4   Stratosphere-troposphere coupling

Until the early 1990s, interactions between the troposphere and the stratosphere were assumed to be one way, consisting in upward wave perturbations from the troposphere per-

16

turbing the stratosphere (e.g., Matsuno 1971). Studies about the influence of the stratosphere on the troposphere (also known as downward coupling or stratosphere-troposphere coupling) have increased exponentially in the last two decades. A major step into the stratosphere-troposphere coupling was the introduction of annular modes to describe the state of the atmosphere at hemispheric scale (e.g., Thompson and Wallace 1998). These studies started with those on the Artic Oscillation (AO), which is the first mode of variability of the NH sea level pressure field (e.g., Ambaum et al. 2001). When it is extended to all vertical levels in the troposphere and the stratosphere using geopotential height, the result is known as the Northern Annular Mode (NAM, e.g., Thompson and Wallace 2000), and it is often used as a measure of the stratosphere-troposphere coupling. In the stratosphere, positive (negative) NAM values consist of a strong meridional pressure gradient and then a strong (weak) polar vortex, whereas in the troposphere, the NAM index is associated with fluctuations of the eddy-driven jet stream (e.g., Gerber et al. 2012). Using NAM-based composites, Baldwin and Dunkerton (2001) illustrated that stratospheric anomalies can propagate downwards from the stratosphere into the troposphere and even the surface in their well-known "dripping paint" (Figure 5).
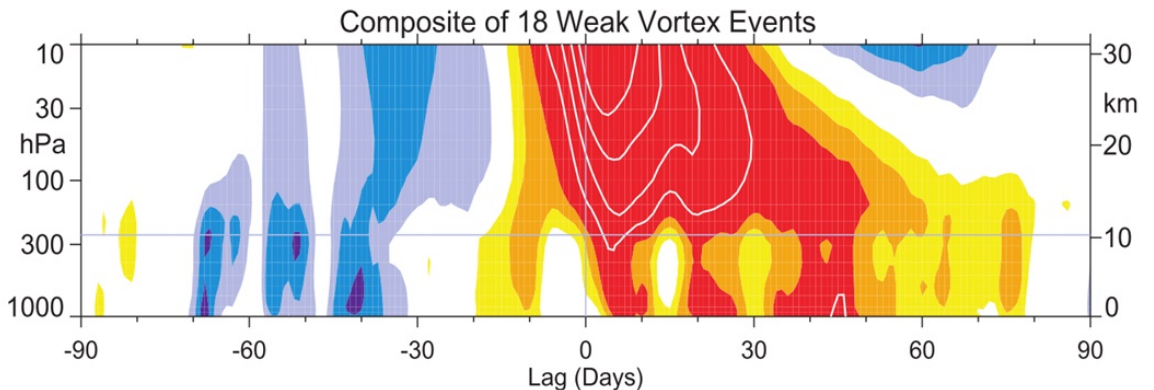
Figure 5: Composite of time-height sections of the NAM index (dimensionless) for 18 weak vortex events. The events are determined by the dates on which the 10-hPa daily NAM index crosses –3.0. The contour interval for the color shading is 0.25, and 0.5 for the white contours. Values between -0.25 and 0.25 are unshaded. The thin horizontal line indicates the approximate boundary between the troposphere and the stratosphere. From Baldwin and Dunkerton (2001).

The set of events composited in Figure 5 reflects extreme conditions in the strength of the stratospheric polar vortex, more specifically anomalously weak vortex events, identified as large negative NAM values at 10 hPa. Although these phenomena have received many names in the literature, they are usually referred to as Sudden Stratospheric Warmings (SSWs) and represent one of the clearest examples of the stratospheric influence on the tropospheric circulation through downward coupling on intraseasonal time-scales.

Stratosphere-troposphere coupling also appears on longer time-scales. Thus, it is known that ENSO, which operates on interannual scales, has an impact on European weather through the stratosphere (e.g., Ineson and Scaife 2009, Bell et al. 2009, Cagnazzo and Manzini 2009, Palmeiro et al. 2017a) favored by the occurrence of SSWs ocurrence. A well-resolved stratosphere in climate models is also been shown to be key to reproduce other atmosphere-ocean coupled phenomena, such as the relationship between the sea surface temperatures of the North Atlantic Ocean and the North Atlantic Oscillation (NAO), which is often considered as the regional manifestation of the AO over the Euro-Atlantic sector (e.g., Omrani et al. 2014).

1.4.1 SSWs in observations

SSWs are the most impressive phenomena of the stratosphere on intraseasonal time scales. They occur during the extended winter (from November to March), mainly in the NH, and are associated with polar cap temperature increases above 20 K in less than one week (Nakagawa and Yamazaki 2006) and a weakening of the polar vortex, which might even break down.

The major interest on SSWs arises from their influence on tropospheric weather, which can potentially be exploited for seasonal predictions of the extended winter in extratropical regions of the NH (e.g., Sigmond et al. 2013). Some studies argued that the morphology

of the polar vortex during these events is important for their surface responses. For instance, Mitchell et al. (2013) showed a more robust signal after SSWs when the vortex splits in two pieces (the so-called splitting SSWs) compared to the events in which the one-piece polar vortex is shifted off the pole (displacement SSWs). However, Maycock and Hitchcock (2015) argued that differences between the impacts of splits and displacements were not consistent. Later, Kodera et al. (2016) classified SSWs depending on whether they were or not followed by a reflection of PWs in the stratosphere (i.e., reflective and absorptive events, respectively), concluding that only absorptive SSWs are characterized by robust annular responses in the tropospheric flow. Recently, Karpechko et al. (2017) suggested that more important than these differentiations are the conditions of the lower stratosphere during the first days after SSW occurrence. If there is wave propagation to the stratosphere at the SSW onset, and the NAM index is negative in the lower stratosphere, the probability for the SSW to be followed by tropospheric impacts increases.

SSWs are also essential to understand the Arctic ozone variability (Schoeberl and Hartmann 1991). When SSWs occur, the polar vortex dissipates, and ozone-rich air enters into the polar stratosphere (Madhu 2016). This occurs frequently in the NH, whereas in the SH, SSWs rarely occur given the smaller PW amplitudes (e.g., van Loon et al. 1973). In September 2002, the first SSW was recorded in the SH (Kruger et al. 2005). The Antarctic ozone hole split in two pieces and a strong increase in the total ozone column was registered (Allen et al. 2003). Several studies associated this event with anomalous wave activity from the troposphere to the stratosphere (e.g., Allen et al. 2003, Nishii and Nakamura 2004), which highlights the key role of stratospheric dynamics in ozone depletion and recovery.

SSWs have been studied since 1952 (Scherhag 1952). Since then, the most extended theory behind SSW precursors refers to enhanced PW activity entering the stratosphere and breaking in the vicinity of the polar vortex (Matsuno 1971). However, the mechanisms behind their occurrence are not fully clear. Furthermore, a unified definition of SSWs

has not been established yet. The World Meteorological Organization (WMO) defined SSWs using the zonal-mean zonal wind and the meridional temperature gradient at 10 hPa (McInturff 1978), further distinguishing between minor SSWs (defined as a meridional temperature gradient reversal) and major warmings (when, in addition, there is a reversal of the zonal-mean zonal wind). However, some studies only use the wind criterion, while many others elaborated their own methods to detect what they called weak vortex events (e.g., Butler et al. 2015). The use of different definitions to analyze SSWs can imply discrepancies in the detection of events and their associated signals, with potential implications on the skill assessment of SSWs in seasonal predictions.
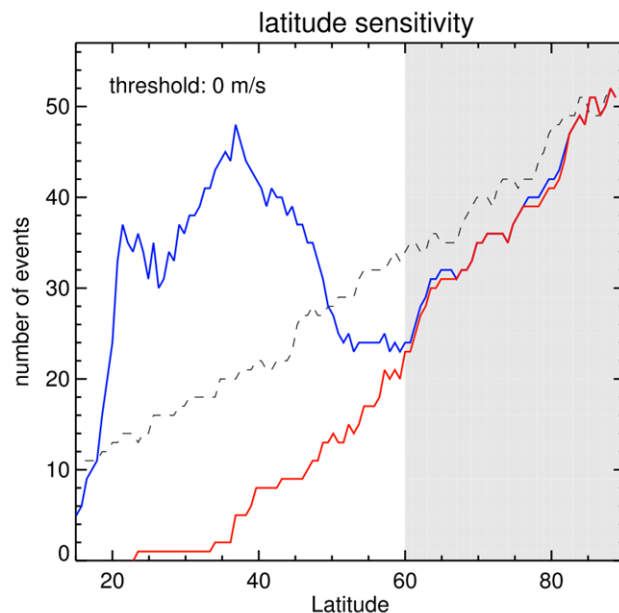
Figure 6: Total number of SSWs for 1979-2012 in ERA-Interim reanalysis as a function of the latitude where the zonal wind reverses from westerly to easterly (0 $ms^{-}1$ critical threshold). "Local" events (blue) occur when the zonal winds at one particular latitude fall below the critical threshold. "Coherent" reversals (red) occur when the zonal winds reverse at all latitudes poleward of the given latitude within 20 days. "Averaged" reversals (black dashed) occur when the zonal winds averaged from a particular latitude to 90°N fall below the critical threshold. From Butler et al. (2015).

Apart from the use of different fields to detect SSWs, the latitude factor is an important source of discrepancy among definitions. Figure 6 shows the number of SSWs obtained

20

using the concept of coherent reversals (e.g., McInturff 1978), which demands the wind reversal to occur everywhere north of a given latitude (red lines), as compared to those obtained using a single latitude (i.e., local reversals, blue line) or using an averaged latitude (black dashed lines). The similarities between the red and blue lines north of 60°N indicate that most SSWs obtained at 60°N are also coherent wind reversals. However, a latitudinal average can increase by ∼30% the obtained frequency of SSWs.

The dilemma of using an absolute criterion (such as the zero zonal-mean zonal wind threshold) or a criterion relative to the background conditions is also under discussion (e.g., McLandress and Shepherd 2009a, Butler et al. 2015, Kim et al. 2017). If the mean strength of the polar vortex changes, the absolute criterion might produce trends in the SSW frequency that might not be reproduced by a method based on anomalies.

The variety of the definitions found in the literature highlights the need to clarify which are the robust signatures among SSW definitions and to what extent their differences are important. In this concern, Chapter 3 (Palmeiro et al. 2015) reviews eight different SSW definitions found in the literature, based on different variables and methods, and compare the characteristics of the obtained catalogues of events using three reanalysis datasets. The study pays special attention to the differentiation between major and minor SSWs and their associated stratosphere-troposphere coupling.

1.4.2   SSWs in models

As SSWs impact the troposphere and surface weather for several months, they provide new opportunities for seasonal forecasting (e.g., Baldwin et al. 2003). The improvement of tropospheric forecasts when including a well-resolved stratosphere in models was already suggested in Boville and Baumhefner (1990). Charlton et al. (2004) noted the importance of the initial conditions in the stratosphere for the quality of short-term tropospheric

forecasts. The potential of SSWs as a predictive tool for seasonal forecasting was shown in Sigmond et al. (2013). They found that forecast runs initialized at the onset date of SSWs led to an improved forecast skill for certain regions during several months after the SSW. Figure 7 compares the surface climate responses of sea Level Pressure and temperature after SSWs in the model forecast and in observations. The forecasts were able to reproduce adequately the observed surface temperatures over northern Russia and eastern Canada as well as the precipitation anomalies over the North Atlantic.
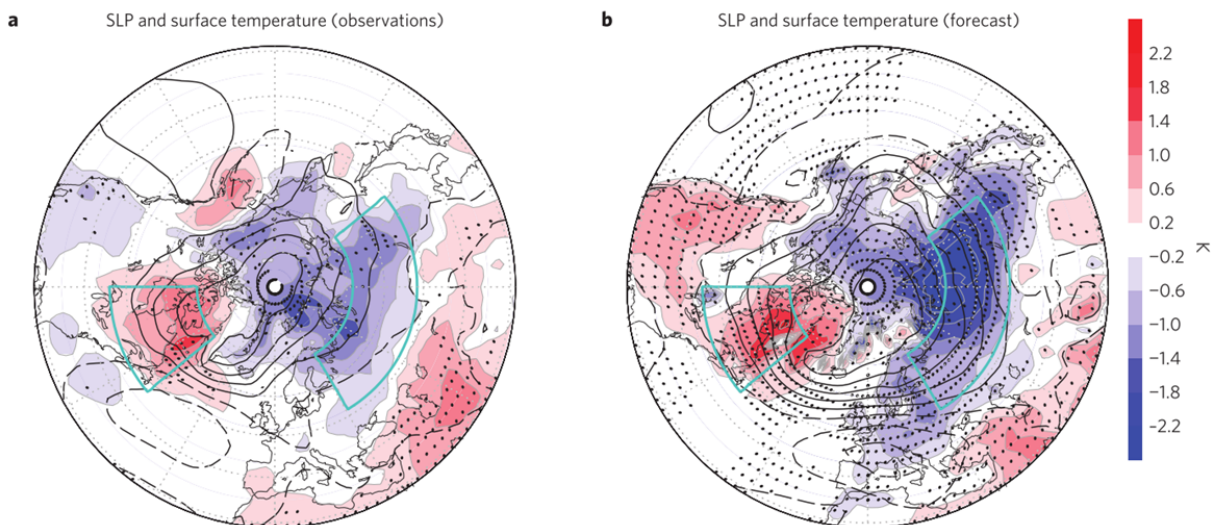
Figure 7: Composites of sea level pressure (contours, in hPa) and surface temperature (shading, in K) anomalies for 16–60 days after SSWs in the observations (a) and the model forecasts (b). Contour interval for sea level pressure is 1 hPa and solid (dashed) contours denote positive (negative) values starting at 0.5 (-0.5) hPa. Black dots represent statistical significance in temperature at the 90% confidence level determined by bootstrapping. From Sigmond et al. (2013).

In spite of this, there are still many uncertainties on the triggering processes of SSWs, so finding the best model configuration to obtain realistic frequencies of SSWs is still a challenge, particularly in global climate models (Charlton-Pérez et al. 2013). In this regard, the SPARC (Stratosphere-troposphere Processes And their Role in Climate) project, within the World Climate Research Programme, includes the Chemistry-Climate Modelling Initiative that aims to achieve a better representation of the atmospheric processes in Chemistry-Climate Models (CCMs). This collaborative activity uses global circulation

22

models with interactive chemistry and vertical extension from the surface to the strato-sphere and above (the so-called high-top models). Comparison of high- and low-top models is very useful to assess the impact of the stratosphere on tropospheric climate. In particular, several studies within the framework of the last Coupled Model Intercomparison Project phase 5 (CMIP5) have stressed the importance of a well-resolved stratosphere to properly account for the impact of the stratosphere-troposphere coupling from intra-seasonal (e.g., SSWs) to interannual (e.g., ENSO, QBO) time-scales (e.g., Gerber et al. 2012; Hardiman et al. 2012; Calvo et al. 2017). For example, Charlton-Pérez et al. (2013) evidenced the importance of a high model lid to obtain realistic SSW frequencies in CMIP5 models (Figure 8). High-top models in Figure 8 (red bars) are mostly within the 95% confidence interval of the reanalysis. However, there are still some high-top models that underestimate the observed frequency of SSWs and some low-top models that reproduce it reasonably well.
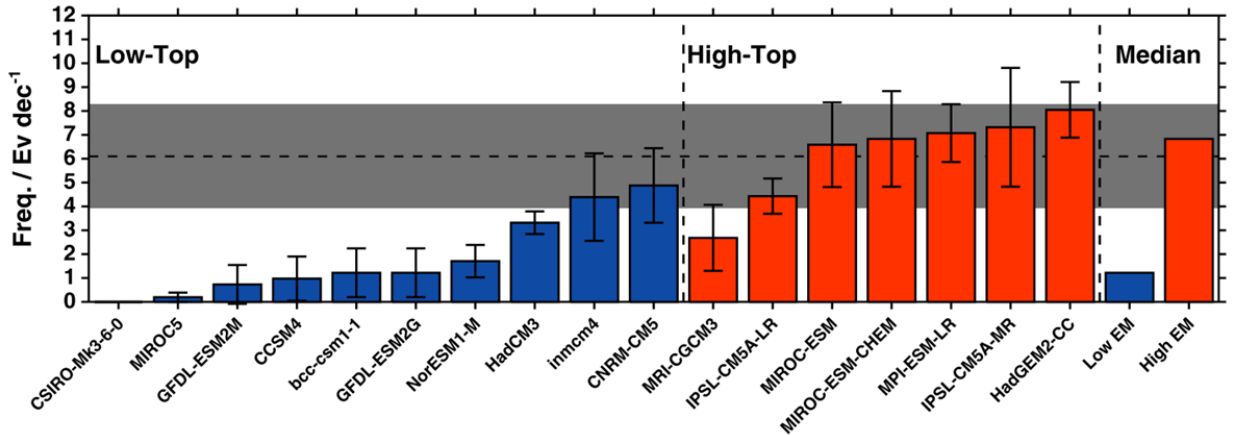
Figure 8: Climatological mean decadal frequency of SSWs for 1960–2000 in 19 historical simulations of CMIP5 models. Colored bars show the number of SSW events per decade, along with 95% confidence intervals for each estimate. Models shown in red are classified as high-top models, those shown in blue as low-top models. The climatological mean decadal frequency in the [2]ERA-40 reanalysis data set is shown by the horizontal dashed black line and the 95% confidence interval for this estimate in gray. On the right of the plot, median estimates for the low-top and high-top ensembles are shown. From Charlton-Pérez et al. (2013).

---

[2]ERA-40 European Centre for Medium-Range Weather forecasts Reanalysis (Uppala et al. 2005):

In addition to the model lid height, the spatial resolution and sub-grid parameterizations are also essential factors to obtain realistic results in stratospheric variability, stratosphere-troposphere coupling and SSW frequencies (e.g., Butler et al. 2015). Charlton-Pérez et al. (2013) showed an improved SSW frequency with the same high-top model by only increasing its horizontal resolution. This is in agreement with previous results reporting a strong sensitivity of the stratospheric variability to the spatial resolution (Scott et al. 2004, Coy et al. 2009, Roff et al. 2011). This is because high-resolution is important to resolve wave propagation and dissipation throughout the atmosphere. For example, SSWs involve the interaction of upward planetary waves with the background flow of the stratosphere during episodes of enhanced planetary wave activity in the troposphere (e.g., Matsuno 1971, Polvani and Waugh 2004). In particular, they are often preceded by tropospheric blocking (e.g., Barriopedro and Calvo, 2014), whose representation in climate models depends on the spatial resolution (e.g., Davini and D'Andrea 2016).

Another important factor to obtain realistic stratospheric variability is the appropriate representation of GWs (Palmer et al. 1986, McFarlane 1987). The wave drag of small-scale GWs must be parametrized in climate models given the computational resources required to simulate them explicitly. Unfortunately, there are other issues to represent GWs realistically, and several simplifications and assumptions are often adopted by most global models (e.g., Richter et al. 2010). In climate models where GWs are not internally simulated but parameterized, they are considered as propagating disturbances only in the vertical, that break when they reach their amplitude threshold, depositing momentum flux and generating GW drag (McLandress 1998). As introduced in Section 1.3, GWs can be originated by different sources (orography, convection, fronts...). Orographic GWs are generated from a static source and so, are better understood than non-orographic ones. For non-orographic or non-stationary GWs, models usually include arbitrary sources that are not necessarily realistic (Garcia and Solomon 1985). In this sense, the Whole Atmosphere Community Climate Model (WACCM), in its version 3.5 implemented an improved GW parameterization that does not include any arbitrary wave source. It consists in the

---

https://www.ecmwf.int/en/research/climate-reanalysis/

individual parameterization of the sources, being possible to distinguish between frontal and convective wave sources (Richter et al. 2010).

A well represented Orographic Gravity Wave Drag (OGWD) is also essential in climate models to reproduce the winter circulation in the stratosphere (e.g., Palmer et al. 1986). Most of this drag occurs in the lowest levels of the stratosphere, at mid-latitudes, and acts to decelerate the background flow. As a result, the subtropical jet separates from the polar jet, modifying the refractive conditions of the background flow and the propagation patterns for PWs (Sigmond and Scinocca 2010). Apart from the model-resolved orographic sources that can generate GWs, WACCM3.5 also included the parameterization of surface stress due to non-resolved orography (Richter et al. 2010). This is denoted as Turbulent Mountain Stress (TMS) and follows the approach used in numerical prediction models as, for instance, the Met Office unified model (Webster et al. 2003).

The TMS parameterization was found to be crucial to reproduce a realistic SSW frequency in WACCM. Richter et al. (2010) found differences in the OGWD due to the implementation of the TMS. Similar to the explanations in Sigmond and Scinocca (2010), they related the improved SSW frequency to changes in PW refraction. However, this mechanism is not able to explain the seasonally varying ability of WACCM to reproduce SSWs. Chapter 4 (Palmeiro et al., 2017b) revisits this issue in an attempt to describe in detail the mechanisms associated with the TMS implementation that lead to an improved frequency of SSWs in WACCM. This study assesses the TMS-induced changes in OGWD through the extended winter season and its role in triggering SSWs.

1.5 The Brewer-Dobson circulation

As stated in the previous sections, the interactions between different types of waves and the mean flow are essential to understand the stratospheric circulation and its variability. The interactions between the mean flow and the eddies can be characterized by using a set of primitive equations and quasi-geostrophic assumptions, as stated in Equations 3.3.2a-e in Andrews et al. (1987). However, the Eulerian approach described therein does not explicitly reproduce key processes occurring in the real atmosphere. In fact, with this formulation and in the case of stationary and conservative waves, the mean meridional eddy heat flux is canceled by the adiabatic heating/cooling associated with the mean vertical motion. Hence, the net eddy transport in the meridional plane is neglected (Andrews and McIntyre 1978). Therefore, to describe a more meaningful connection between the eddies and the mean flow, Andrews and McIntyre (1976) introduced the Transformed Eulerian Mean (TEM), which results in the residual circulation ($\overline{v}^*$,$\overline{w}^*$), whose components in spherical coordinates are:

$$\overline{v}^* = \overline{v} - \frac{1}{\rho_0}\frac{\partial}{\partial z}\left(\rho_0 \frac{\overline{v'\theta'}}{\overline{\theta_z}}\right) \tag{1.4}$$

$$\overline{w}^* = \overline{w} - \frac{1}{a \cdot cos\varphi}\frac{\partial}{\partial \varphi}\left(cos\varphi \frac{\overline{v'\theta'}}{\overline{\theta_z}}\right) \tag{1.5}$$

Under this formulation, the zonal momentum equation can be expressed as:

$$\frac{\partial \overline{u}}{\partial t} + \overline{v}^*\left(\frac{1}{acos\phi}\frac{\partial}{\partial \phi}\left(\overline{u}cos\phi\right) - f\right) + \overline{w}^*\frac{\partial \overline{u}}{\partial z} = \frac{\boldsymbol{\nabla} \cdot \mathbf{F}}{\rho_0 \cdot acos\phi} + \overline{X} \tag{1.6}$$

where $\overline{X}$ represents the force due to small-scale eddies, and $\mathbf{F}$ is the Eliassen-Palm (EP) flux vector, which represents the flux wave activity (Andrews et al. 1987). The divergence of the EP flux, $\boldsymbol{\nabla} \cdot \mathbf{F}$, is often used as a diagnostic of the wave-mean flow interaction. Thus, when $\boldsymbol{\nabla} \cdot \mathbf{F}$ is negative, there is wave convergence that can be interpreted as regions of potential wave breaking and hence wave drag on the mean flow. The meridional and vertical components of the EP flux are defined as:

$$F^\phi = \rho_0 a cos\phi \left(\frac{\partial \overline{u}}{\partial z} \frac{\overline{v'\theta'}}{\partial \overline{\theta}/\partial z} - \overline{v'u'} \right) \qquad (1.7)$$

$$F^z = \rho_0 a cos\phi \left(\left[f - \frac{1}{a cos\phi} \frac{\partial}{\partial \phi} \left(\overline{u} cos\phi \right) \right] \frac{\overline{v'\theta'}}{\partial \overline{\theta}/\partial z} - \overline{w'u'} \right) \qquad (1.8)$$

Following Equation 1.6, for a steady zonal-mean flow, a wave-driven residual circulation $(\overline{v}^*, \overline{w}^*)$ is induced when there is wave dissipation $(\boldsymbol{\nabla} \cdot \mathbf{F} \neq 0)$. The downward control principle introduced by Haynes et al. (1991) states that the vertical component of the residual circulation at a certain altitude, z, can be estimated between latitudes ϕ_1 and ϕ_2 by the wave drag from above, as:

$$\langle \overline{w}^*(z) \rangle = \frac{\frac{1}{\rho(z)} \left| \int_z^\infty \left\{ \rho a cos^2\phi \left[(\rho a cos\phi)^{-1} \boldsymbol{\nabla} \cdot \mathbf{F}(\phi, z') + X(\phi, z') \right] / \overline{m}_\phi \right\} dz' \right|_{\phi_1}^{\phi_2}}{|sin\phi|_{\phi_1}^{\phi_2}} \qquad (1.9)$$

where $m = a cos(\phi)(\overline{u} + \Omega a cos(\phi))$, is the angular momentum. Thus, wave forcing produces a response that is predominantly downwards, and hence, the circulation at a given altitude can be influenced by the forcing from above (Thompson et al. 2006). This principle provides a practical way to estimate the contribution of different waves to the residual circulation defined in Eq. 1.4 and 1.5. When averaged over time, this circulation appears as a meridional overturning in the stratosphere, also known as the Brewer-Dobson Circulation (BDC), responsible for the mass transport between the tropics and extratropics. In fact, the BDC reproduces the meridional and vertical transports described by observations of water vapor in Brewer (1949) and ozone in Dobson (1956). The residual circulation can thus be interpreted as the wave-driven part of this meridional circulation and hence is considered a good proxy to diagnose the BDC (e.g., Holton 1990). Note that in a strict way the BDC refers to the chemical transport of tracers, which also involves two-way mixing without net transport of mass (e.g., Shepherd 2002).
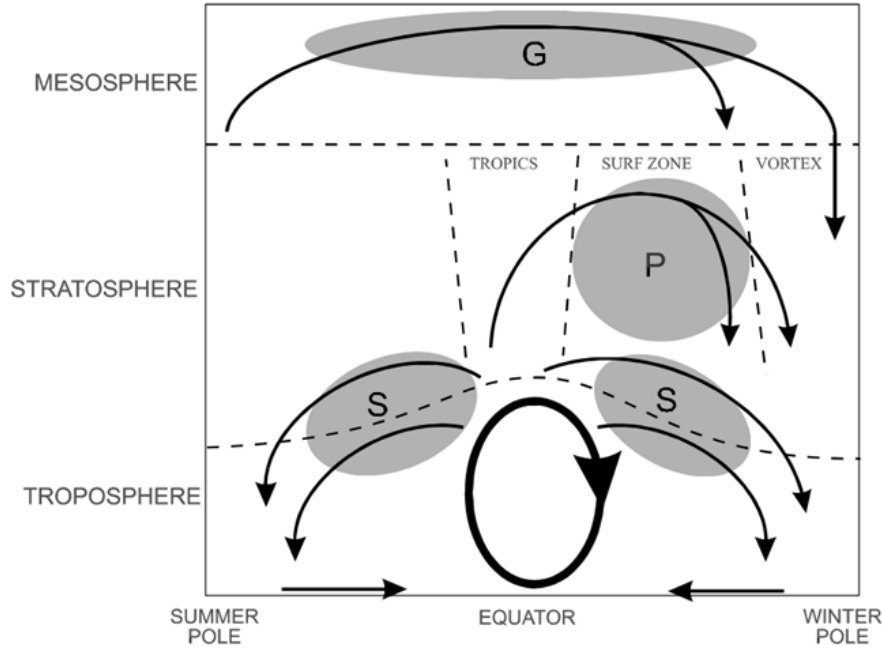
Figure 9: Schematic of the BDC in the atmosphere. The heavy ellipse denotes the thermally-driven Hadley circulation of the troposphere. The shaded regions (labelled "S", "P", and "G") denote regions of wave breaking (synoptic, PWs and GWs, respectively), responsible for driving branches of the stratospheric and mesospheric circulation. From Plumb (2002).

Following the schematic representation in Figure 9, the BDC consists in several cells of upwelling and downwelling (Plumb 2002). In the stratosphere, two different branches of the circulation can be distinguished, operating at different time-scales (Birner and Bönisch 2011). One is referred as the shallow branch, with maximum upwelling in the tropical lower stratosphere and downwelling in the subtropics, and it is mostly driven by synoptic-scale waves. The upper branch, referred to as the deep branch, is mostly driven by PWs, and it is characterized by upwelling in the upper tropical stratosphere and downwelling in the polar stratosphere of the winter hemisphere. This seasonality is associated with the limitations of the background flow to wave propagation in the stratosphere described in Section 1.3. In the mesosphere, there is a global pole-to-pole circulation from the summer to the winter hemisphere, and it is mostly driven by GWs (Plumb 2002).

1.5.1 SSWs and the BDC

As discussed above, SSWs are associated with anomalous PW dissipation in the strato-
sphere. They are usually preceded by a cold and strong polar vortex that acts as a waveg-
uide enhancing PW propagation into high latitudes (McIntyre 1982). Dunn-Sigouin and
Shaw (2015) came to the same finding, showing enhanced planetary-scale stratospheric
heat fluxes before SSWs. The opposite occurs after SSWs, as shown by Shaw and Perwitz
(2013). This is consistent with the analysis in Limpasuvan et al. (2004), which illustrates
inhibition of wave propagation following the occurrence of SSWs and hence reduced PW
dissipation. Therefore, these wave drag variations observed before and after SSWs must
have an imprint on the BDC strength (Matsuno 1971). In this sense, Gerber (2012) argued
that increased PW drag must lead to a deepening of the BDC and Gómez-Escolar et al.
(2014) reported an enhancement of the tropical upwelling in the middle stratosphere prior
to SSWs. Comparing winters with and without SSWs in the Canadian Middle Atmosphere
Model, McLandress and Shepherd (2009a) showed an ~10% increase in the BDC strength
due to SSWs. Abalos et al. (2015) identified peaks of strong tropical upwelling at 70 hPa
during winters with SSWs in several reanalyses (Figure 10).

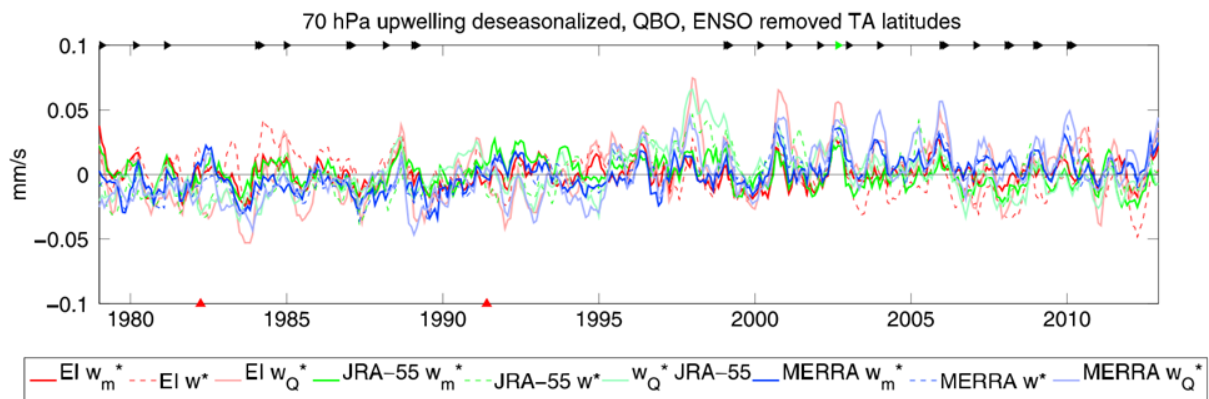Figure 10: Time series of deseasonalized tropical upwelling near 70 hPa after removing the
variability associated with QBO and ENSO. A five-point running mean has been applied to
the monthly time series. Black triangles show SSWs (in green the SH event of September
2002), and red triangles at the bottom correspond to the El Chichón (approximately April
1982) and Pinatubo eruptions (June 1991). From Abalos et al. (2015)

Apart from the previous studies, the relationship between the BDC and SSWs has not been assessed in detail. In particular, the interactions between SSWs and the downwelling of the deep branch of the BDC, which occurs at the location of the polar vortex, remains unexplored. Chapter 5 examines the variations in the BDC during the SSW lifecycle (i.e., the onset and recovery phases of the polar vortex) by using 150-year data from WACCM simulations. Moreover, the modulating effect of SSWs in the BDC transition from the winter to the summer circulation is also investigated. These issues are also explored in a future warming scenario to assess changes in the BDC-SSW relationship under increasing anthropogenic forcing conditions.

1.5.2   Future changes in the BDC

The impact of human activities on the climate system has also been detected in the chemical composition of the stratosphere, which subsequently alters atmospheric dynamics (IPCC 2013). The detection of the Antarctic ozone hole associated with increased emissions of chlorofluorocarbons (CFCs) and other halogenated Ozone Depleting Substances (ODS), its recovery, and the interplay of increasing Greenhouse Gases (GHGs) constitute one of the major concerns in studies of recent and future changes in the stratosphere (WMO/UNEP 2014).

As previously introduced, the BDC is responsible for air transport between the tropics and the poles. Figure 11 illustrates the BDC transport of ozone and ODS through the stratosphere and their interactions. Studies from Schmidt and Khedim (1991) found that air masses need ∼5 years to be transported from the troposphere to the upper stratosphere. Given that only 10% of the tropospheric air mass is exchanged with the upper stratosphere within this period, the lifetime of ODS would be from 50 to 500 years depending on the particular substance (Solomon 1999). The role of the BDC in the ongoing ozone recovery is of particular importance for three reasons. One is because the main source region of

ozone is the tropical upper stratosphere, where photolysis of oxygen occurs. The second is related to the destruction of the ODS, since the circulation rates of the BDC determine the timescales at which ODS are processed and then removed from the atmosphere (e.g., Holton et al. 1995). Finally, the strength of the BDC determines how much the pole warms by adiabatic warming and the likelihood of PSCs to develop (Calvo et al. 2017). Hence, changes in the BDC speed might have important implications in the future ozone recovery.
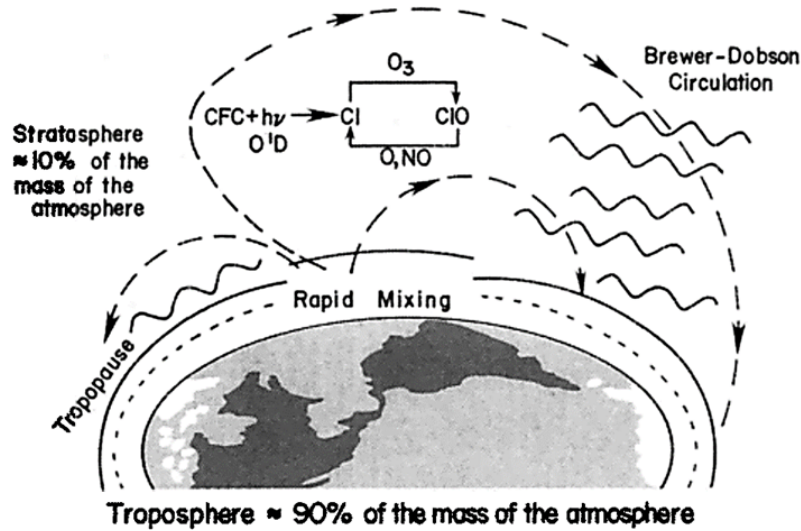
Figure 11: Schematic diagram illustrating the catalytic destruction of ozone in the middle and upper stratosphere. The simplified cartoon illustrates only the key net processes (including the BDC) that transport CFCs and other ODS in a zonally averaged sense. From Solomon (1999).

In this sense, there is general agreement across models on projecting a BDC acceleration as a direct response to increasing GHGs in future climate change scenarios (Butchart 2014). However, this has not been detected yet in reanalysis datasets or observations. Abalos et al. (2015) compared recent changes in the BDC obtained from three different reanalyses and found discrepancies in the sign of the trend between ERA-Interim and other reanalyses ([3]JRA-55 and [4]MERRA, which showed an acceleration of the BDC, consistent with model

---

[3]Japanese 55 year Reanalysis (Ebita et al. 2011):
https://jra.kishou.go.jp/index.html/

[4]Modern-Era Retrospective Analysis for Research and Applications (Rienecker et al. 2011):
https://gmao.gsfc.nasa.gov/reanalysis/MERRA/

simulations). Controversy is also large in observational studies. Fu et al. (2015) reported an accelerated BDC from 1980 to 2009, contrary to results based on age of air estimations (e.g., Engel et al. 2009, Ray et al. 2010, Stiller et al. 2012). These inconsistencies are considered the result of several factors. Since the BDC has to be inferred indirectly in observations, and any forced change must be separated from those due to natural variability, the detection of significant trends in the short observational record is difficult (e.g., Forster and Thompson et al. 2011). Detecting a statistically significant trend in reanalyses might not yet be possible, either. In this sense, Hardiman et al. (2017) argued that uncertainties associated with vertical motions are larger than the predicted trends in reanalyses, and dynamical variability can mask long-term trends.

Therefore, long model simulations are a useful tool to investigate the mechanisms behind the BDC and their possible future changes. Although positive trends in the strength of the shallow branch of the BDC are robust in model studies (e.g., Butchart et al. 2006, Garcia and Randel 2008, McLandress and Shepherd 2009b, Butchart et al. 2010), there is no consensus regarding the dynamical mechanisms behind these trends, and certain model dependence is found when attributing them to different waves. Models agree that $\sim$70% of the BDC is driven by resolved waves, but there is disagreement regarding the specific contributions of the different types of GWs, which account for the remaining 30% of the total wave drag (e.g., Butchart et al. 2011). This disagreement is particularly acute in the middle and upper stratosphere, where the role of non-orographic GWs becomes larger. In this regard, few studies have explored the driving mechanisms behind the deep branch of the BDC. In spite of this, there is general agreement between CCMs and CMIP5 models on a projected strengthening of the deep branch (Lin and Fu 2013, Hardiman et al. 2014) and changes in parameterized GWs seem to play a key role in driving this trend (Oberländer et al 2013). Thus, the specific parameterizations implemented in each particular model might be key for the interpretation of the deep branch mechanisms and its future trends (Garny et al. 2011).

Using WACCM4, which is fully coupled to an interactive ocean model and includes non-arbitrary sources in the parameterizations of GWs (Richter et al. 2010), Chapter 6 (Palmeiro et al. 2014) analyzes the mechanisms driving the BDC, and the changes due to anthropogenic forcings under three different climate change scenarios. The focus of this study is the deep branch of the BDC, which has been less investigated, and has a major role in polar ozone recovery. Given the hemispheric differences due to ozone recovery projected for the 21st century in the SH, polar downwelling in the NH and SH are analyzed separately. Different wave forcings are also considered, including their respective contributions in driving the BDC and its future trends.

Chapter 2

Objectives - Scientific questions

In an attempt to better understand the processes that drive stratospheric variability, stratosphere-troposphere coupling and their future changes, this thesis aims to answer the following scientific questions:

- To which extent is the SSW definition important? In this sense, different definitions will be used to diagnose and characterize SSW characteristics and to investigate their implications for stratosphere-troposphere coupling, including a discussion on the best method to define SSWs.

- How do new model implementations such as the TMS parameterization affect the representation of stratospheric variability and the occurrence of SSWs in WACCM4? The dynamical processes whereby the TMS modulates the stratospheric circulation will be analyzed, paying special attention to the propagation and dissipation of PWs and OGWs.

- How do SSWs interact with the polar downwelling of the deep branch of the BDC in WACCM4? The potential effects of the timing of SSWs on the winter-to-summer transition of the BDC will also be assessed. The projected changes of these interactions will be explored in a future climate change scenario.

- Which are the driving processes of the BDC and its projected changes under different

climate change scenarios in WACCM4? The shallow and the deep branches of the BDC will be evaluated separately, assessing the role of different waves to the total wave driving.

The above questions are addressed in the next chapters, which are presented as a compendium of papers. Chapter 3 compares eight SSW climatologies obtained by applying different definitions to detect SSWs in three reanalysis datasets (Palmeiro et al. 2015). By using two simulations, one with and one without the TMS parameterization, the dynamical mechanisms whereby the TMS leads to realistic SSW frequencies in WACCM4 are explored in Chapter 4 (Palmeiro et al. 2017b, submitted). In Chapter 5, the relationship between SSWs and the deep polar branch of the BDC is assessed using WACCM4 simulations under both, fixed and increasing GHGs. Finally, Chapter 6 analyzes the future trends of the deep and shallow branches of the BDC in three climate change scenarios run with WACCM4 (Palmeiro et al. 2014).

Chapter 3

Comparing sudden stratospheric warming definitions in reanalysis data

Comparing Sudden Stratospheric Warming Definitions in Reanalysis Data*

Froila M. Palmeiro

Departamento de Fisica de la Tierra II, Universidad Complutense de Madrid, Madrid, Spain

David Barriopedro and Ricardo García-Herrera

*Departamento de Fisica de la Tierra II, and Instituto de Geociencias, Centro Mixto del Consejo
Superior de Investigaciones Científicas, Universidad Complutense de Madrid, Madrid, Spain*

Natalia Calvo

Departamento de Fisica de la Tierra II, Universidad Complutense de Madrid, Madrid, Spain

(Manuscript received 23 December 2014, in final form 15 June 2015)

ABSTRACT

Sudden stratospheric warmings (SSWs) are characterized by a pronounced increase of the stratospheric polar temperature during the winter season. Different definitions have been used in the literature to diagnose the occurrence of SSWs, yielding discrepancies in the detected events. The aim of this paper is to compare the SSW climatologies obtained by different methods using reanalysis data. The occurrences of Northern Hemisphere SSWs during the extended-winter season and the 1958–2014 period have been identified for a suite of eight representative definitions and three different reanalyses. Overall, and despite the differences in the number and exact dates of occurrence of SSWs, the main climatological signatures of SSWs are not sensitive to the considered reanalysis.

The mean frequency of SSWs is 6.7 events decade^{-1}, but it ranges from 4 to 10 events, depending on the method. The seasonal cycle of events is statistically indistinguishable across definitions, with a common peak in January. However, the multidecadal variability is method dependent, with only two definitions displaying minimum frequencies in the 1990s. An analysis of the mean signatures of SSWs in the stratosphere revealed negligible differences among methods compared to the large case-to-case variability within a given definition.

The stronger and more coherent tropospheric signals before and after SSWs are associated with major events, which are detected by most methods. The tropospheric signals of minor SSWs are less robust, representing the largest source of discrepancy across definitions. Therefore, to obtain robust results, future studies on stratosphere–troposphere coupling should aim to minimize the detection of minor warmings.

1. Introduction

The winter stratospheric polar circulation is characterized by strong westerly winds referred to as the polar vortex. This circulation is disturbed by upward propagating waves from the troposphere that dissipate in the stratosphere (e.g., Andrews et al. 1987). An extreme manifestation of this wave–mean flow interaction can lead to a dramatic weakening of the polar vortex and a rapid warming of the polar stratosphere (e.g., Matsuno 1971), referred as a sudden stratospheric warming (SSW). This phenomenon was detected for the first time during the 1952 winter (Scherhag 1952). SSWs are a clear manifestation of stratosphere–troposphere coupling, and the downward propagation of the anomalies from the stratosphere to the troposphere after SSW occurrence can be used to improve Northern Hemisphere winter weather forecasts (e.g., Sigmond et al. 2013). This has launched international initiatives that aim to better understand the precursor

TABLE 1. Methodologies for SSW detection. For each method, the first six columns show the original reference, the acronym used in the text, the winter period of SSW detection, the basic criterion, and the region and pressure level employed in the definition. The last column indicates the minimum time interval demanded between two consecutive events.

Definition	Acronym	Period	Criterion	Latitude	Level	Time of recovery
WMO (McInturff 1978)	U&T[a]	Nov–Apr	$\bar{u}_{60N} < 0\,\mathrm{m\,s^{-1}}$　$\overline{T}_{90N} - \overline{T}_{60N} > 0\,\mathrm{K}$	60°–90°N	10 hPa	20 days
Baldwin and Dunkerton (2001)	EOFz[b]	Nov–Apr	NAM < −3.0	20°–90°N	10 hPa	60 days
Limpasuvan et al. (2004)	EOFu[c]	Oct–Apr	SZI < −1.0	20°–90°N	50 hPa	40 days
Taguchi and Hartmann (2005)	Tanom[d]	Oct–May	ZM Temperature anomalies > 30 K	88°N	10 hPa	60 days
Kodera (2006)	Urate[e]	Dec–Feb	$\Delta[\bar{u}_{50-70N}]_{7days} < -2.0\,\mathrm{m\,s^{-1}}$	50°–70°N	10 hPa	—
Nakagawa and Yamazaki (2006)	Trate[f]	Oct–May	$\Delta[\overline{T}_{80-90N}]_{6days} > 20\,\mathrm{K}$	80°–90°N	10, 20, 30 hPa	30 days (the weakest event is discarded)
Charlton and Polvani (2007)	U60	Nov–Mar	$\bar{u}_{60N} < 0\,\mathrm{m\,s^{-1}}$	60°N	10 hPa	20 days from $\bar{u}_{60N} > 0\,\mathrm{m\,s^{-1}}$
Seviour et al. (2013)	MOM	Dec–Mar	Centroid latitude < 66°N (displacements) Aspect ratio > 2.4 (splits)	50°–90°N	10 hPa	30 days

[a] We herein adopt the Limpasuvan et al. (2004) criterion, according to which the temperature difference has to be positive for at least 5 days within the period from 10 days before to four days after the first day of wind reversal. Note that U&T is basically the WMO definition with some added specifications.

[b] See text for details.

[c] The SZI index is calculated as the PC1 of the daily ZMZW area-weighted anomalies at 50 hPa, north of 20°N and from October to April. The resulting PC1 is then standardized for the same period and low-pass filtered with a cutoff value of 15 days. The midpoint since the 15-day low-passed SZI drops below −1 standard deviation and raises again above −1 standard deviation is the detection date in the original definition. We take instead the first day when the 15-day low-passed SZI drops below −1 standard deviation (see text for details).

[d] The onset date is defined when the temperature anomaly becomes maximum.

[e] For each day, the ZMZW tendency, U_t, is constructed from centered running means as the difference between two seven-day mean values spaced by eight days. The onset date is the day with the largest deceleration among those below $-2\,\mathrm{m\,s^{-1}\,day^{-1}}$.

[f] The area-weighted zonal mean temperature north of 80°N is first computed at 10, 20, and 30 hPa. The warming rate is computed at each level. The onset date occurs when the warming rate at 10 hPa is maximum as long as it exceeds 20 K per 6-day period in one of the three levels. If the criterion is only satisfied for one day at 10 hPa the event is discarded.

forcings, the underlying dynamics, and the potential predictive skill of these extreme events, such as the Stratospheric Network for the Assessment of Predictability (SNAP; e.g., Tripathi et al. 2015).

The World Meteorological Organization (WMO) distinguishes between two types of events: 1) major midwinter warmings, characterized by a "complete circulation reversal," and 2) minor warmings, with "limited circulation changes" (WMO/IQSY 1964). Based on this general form of the WMO definition, minor warmings have traditionally been detected as a reversal of the meridional temperature gradient over the polar cap at 10 hPa, whereas an additional reversal of the zonal-mean zonal wind (ZMZW) at 10 hPa is often required for major warmings (e.g., Labitzke 1981). On the other hand, the term "final warming" is often employed to refer to those SSWs that do not display a return to westerly winds and hence mark the transition to the easterly summer circulation (e.g., Labitzke and Naujokat 2000). In the last decade, many authors have identified SSWs modifying the former WMO definition or applying different diagnostic variables (Table 1). Here, we examine whether the climatological signatures of SSWs depend on the definition used. Thus, we review all definitions of SSWs found in the literature, including those publications that do not deal specifically with SSWs, but with polar vortex extreme events in general. Figure 1 summarizes these definitions and classifies them according to the nature of the basic field used in the diagnosis and the specific methodology applied. Some definitions only refer to major SSWs, although most methods do not discriminate between major and minor events. Several methods include final warmings, while others filter them out by imposing conditions to the timing and characteristics of the events. All these differences highlight the different perceptions of SSWs, and contribute to the discrepancies in the detected events. Furthermore, some methods allow differentiation of events in types, according to 1) the morphology of the polar vortex, which leads to displacement SSWs (in which the vortex is displaced off the pole), and splitting SSWs (when the polar vortex is divided into two pieces) (e.g., Andrews et al. 1987), and 2) the dominant wavenumber signatures in the polar stratosphere preceding the SSW, which leads to events of wavenumbers 1 to 2 (e.g., Bancalá et al. 2012; Barriopedro and Calvo 2014).
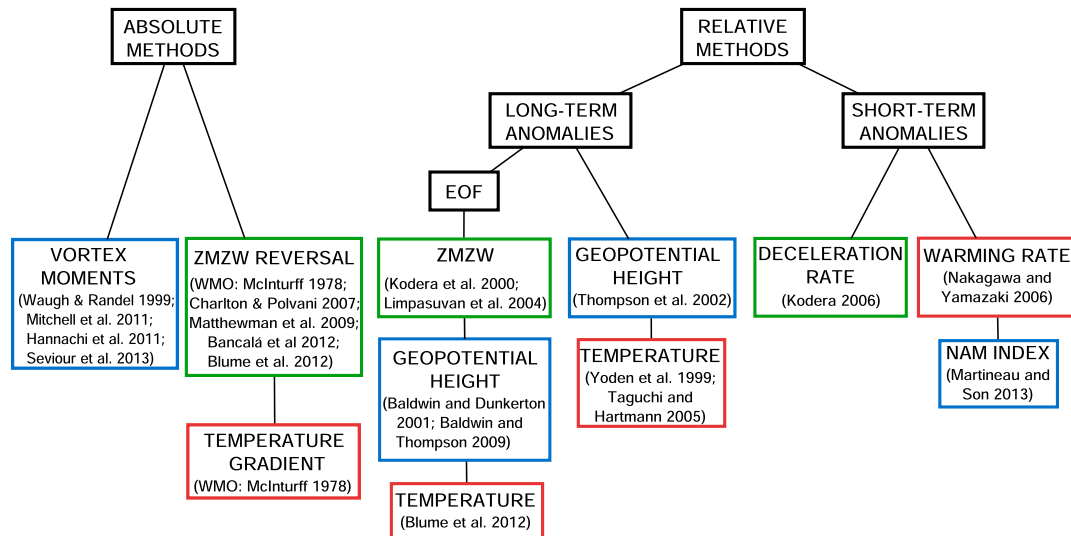
F<small>IG</small>. 1. Review of SSW detection methodologies. Methods are classified according to the nature (absolute and relative fields) and the specific diagnostic applied in the detection (colored boxes). The color indicates the field used to identify the events: geopotential height (blue), zonal-mean zonal wind (green), and temperature (red). (See text for details).

The first category of methods shown in Fig. 1 includes those based on imposed thresholds over absolute fields. Within this group, and similar to the WMO's definition of major SSWs (U&T; see acronyms for the eight methods listed in Table 1), many authors consider exclusively the 10-hPa ZMZW reversal at 60°N to diagnose the occurrence of SSWs (e.g., Charlton and Polvani 2007; Matthewman et al. 2009; U60). There are also more sophisticated methods such as those based on vortex moments (e.g., Waugh and Randel 1999; Hannachi et al. 2011). In particular, Mitchell et al. (2011) perform elliptical diagnoses of the polar vortex through potential vorticity (PV) fields to diagnose SSWs, and this methodology has been recently adapted to 10-hPa geopotential height input data, yielding similar results (Seviour et al. 2013; MOM).

Definitions based on relative fields appear in the right-hand side of Fig. 1. These methods do not distinguish between major and minor SSWs and can, in turn, be classified into two groups, depending on whether the departure fields are defined as 1) anomalies with respect to a climatological long-term mean or 2) rates of change (i.e., tendency), computed as the difference between two consecutive short-term periods, ranging from one day to one week. The first group of definitions considers methods that impose thresholds on the anomaly field (e.g., Yoden et al. 1999; Thompson et al. 2002; Taguchi and Hartmann 2005; Tanom) and those based on principal component analysis (PCA). Among those involving PCA, Baldwin and Dunkerton (2001; EOFz) use the northern annular mode (NAM) index, defined as the

projection of the geopotential height anomalies at 10 hPa onto the first empirical orthogonal function (EOF) pattern. Similar to Kodera et al. (2000), Limpasuvan et al. (2004; EOFu) employ the stratospheric zonal index (SZI), which is defined as the first principal component (PC1) of the ZMZW latitudinal distribution at 50 hPa, while Blume et al. (2012) use the PC1 of the 10-hPa polar cap temperature. Methods based on short-term tendencies include the definition of Nakagawa and Yamazaki (2006; Trate), which sets a minimum warming rate at several pressure levels, and that of Martineau and Son (2013), employing the NAM index tendency at 10 hPa to identify SSWs. Finally, Kodera (2006; Urate) demands a minimum deceleration rate of the 10-hPa ZMZW over the polar cap.

It is therefore clear that these methods differ not only in the basic field employed to detect SSWs, but also in the data treatment (zonal means, anomalies, etc.), the specific region of the polar stratosphere considered (i.e., a given latitude or the polar cap average, the vertical level chosen), and the different nature of the events (i.e., minor, major, and final warmings). Some of these issues have been noticed by Butler et al. (2015), who found differences in the total frequency of the events resulting from small changes in the demanded criteria. Most of the methodologies have been applied to reanalysis data, and some differences have also been obtained for different reanalysis products, revealing that the specific reanalysis can be an additional source of discrepancy. In fact, different reanalyses may involve time lags in the detection of the same event and different frequencies of occurrence

(e.g., Charlton and Polvani 2007) and hence potential differences in the SSW signatures.

The aim of our study is to perform a systematic comparison of the SSW definitions used in the literature in reanalysis datasets. We have applied the original methods (or slightly modified versions, for the sake of fair comparisons) to three different reanalyses over the same time period (section 2). To assess whether the SSW signatures are sensitive to the chosen definition, an intercomparison exercise is performed among all methods, focusing on the intraseasonal and decadal distributions of events (section 3a), the SSW characteristics in the middle stratosphere (section 3b), the downward propagation anomalies, and the surface signals before and after events (section 3c). Conclusions are presented in section 4.

2. Data and methods

We have used daily mean data from 1958 to 2014 from the NCEP–NCAR (Kalnay et al. 1996), the JRA-55 (Ebita et al. 2011) and the ERA (ERA-40 for 1957–2002 plus ERA-Interim for 2002–14; Uppala et al. 2005; Dee et al. 2011) reanalyses. All datasets were first interpolated to a common regular grid of $2.5° \times 2.5°$ spatial resolution. The basic fields computed in this study include zonal means of temperature, zonal wind, and geopotential height at various vertical levels, as required from the different definitions of SSWs. In addition, mean sea level pressure (MSLP) anomalies and several products were derived at daily time scales. They include the zonal mean meridional eddy heat flux $\overline{v'T'}$ at 100 hPa averaged over 45°–75°N (where the overbar indicates the zonal mean and the primes deviations from it) and the NAM index. To calculate this index we use the daily anomalies of the zonal mean geopotential height north of 20°N for the entire year. Then, we perform a PCA for each pressure level separately, and the resulting PC1 (standardized for the whole year) is taken as the NAM index. In all the results presented here, latitudinal averages are always weighted by the cosine of latitude, and anomalies are computed with respect to a daily-based climatology over the 1958–2014 period. Different ways of merging ERA data products were tested, all leading to similar results. An additional comparison of the ERA-40 and ERA-Interim reanalyses for their common period (1979–2002) revealed negligible differences in the results of this study.

We have used eight definitions of SSWs (see Table 1), which are considered representative of all of those shown in Fig. 1: U&T, EOFz, EOFu, Tanom, Urate, Trate, U60, and MOM. The detection of SSWs has been carried out by applying the original definitions given in the corresponding papers for the three reanalyses (except MOM, for which the onset dates of SSWs in ERA were directly provided by the authors). Although the WMO distinguishes between major and minor SSWs, we only used its definition for major events since the inclusion of minor warmings led to a disproportionate number of SSWs as compared with the rest of the methods. We are aware that the U60 and U&T definitions can be considered redundant as they both are based on the reversal of the ZMZW at 10 hPa. However, the U&T definition additionally requires a reversal of the temperature gradient, and, given the popular use of these definitions, we decided to include both in our analysis. Note also that all methods except Urate demand a minimum time interval between consecutive events that ranges from 20 to 60 days. The Urate definition instead picks for each winter the event with the largest wind deceleration among those satisfying its criteria, so only one event per winter can be detected.

The dates of detection of SSWs will be referred to hereafter as onset dates. In some methods, the onset corresponds to the day with the largest value of the diagnostic parameter, while in others it is defined as the first time the required conditions are satisfied. In this regard, some minor modifications were introduced in some original definitions to provide a fair comparison across methods. EOFu required a readjustment in the definition of the onset dates of SSWs since there was a systematic lag of about 20 days in the dates of the events in comparison with the other methods. This is not surprising, since in their original study, Limpasuvan et al. (2004) already denoted the beginning of the SSW as the $[-37, -23]$-day period before the detection date. This is the midpoint between the day when the SZI exceeded -1 standard deviation and the day when the SZI returned to values below that threshold. However, this methodology depends on the persistence of the event and hence it can depart considerably from the timing used in the other definitions (the beginning or the peak of the anomalous period). Thus, in our study, and for the EOFu definition only, we settled the onset of the warming as the first day the SZI becomes lower than -1 standard deviation, which yields results more comparable with the other methods. In the case of EOFz, we followed the methodology described by Baldwin and Dunkerton (2001), although we have taken unfiltered data for the entire year. In addition, zonal mean geopotential height anomalies have been used to obtain the first EOF, instead of the full 2D field that was employed in the original study, as recommended later by Baldwin and Thompson (2009).

U60 is the only method that explicitly defines final warmings as those for which the ZMZW does not return to westerlies for at least 10 consecutive days before

30 April. We have applied this criterion to all methods in order to identify and exclude these events from our analyses. Note that Tanom and Urate do not need this consideration because their period of detection ends in February. Table S1 in the supplementary material (available online at http://dx.doi.org/10.1175/JCLI-D-15-0004.s1) lists the SSWs identified by the different definitions, with events in bold indicating final warmings. Note that there are SSWs that are detected by several methods, albeit with different onset dates. These events will be hereafter referred to as common events, and appear in the same row of the table. For all definitions, events reaching the wind reversal (according to the U60 definition) are denoted as major SSWs. The remaining events will be classified as minor SSWs, even if they do not satisfy the WMO temperature gradient condition. However, similar results are obtained if the minor warming group only includes those events that are catalogued as such by the WMO. A separated analysis between major and minor SSWs will be performed when indicated. Otherwise, all events in Table S1 except final warmings will be considered.

Note that our study does not classify the events with respect to either the spatial structure of the stratospheric polar vortex (i.e., vortex splits and displacement SSWs) or the preconditioning of the polar vortex (i.e., events of wavenumber 1 and 2). This is because there is not a unique criterion to perform these classifications. For example, Charlton and Polvani (2007) and Mitchell et al. (2011) have their own criteria to classify SSWs into splitting/displacement events, and discrepancies in the classification of their common events were reported in the latter (Mitchell et al. 2011, their Table 1). Additionally, the split/displacement catalogue is sensitive to the reanalysis product (Charlton and Polvani 2007, their Table 1). Consequently, the arrangement of SSWs by their type is not consistent across reanalyses and methods, and would add unnecessary complexity to the intercomparison exercise.

In the following analyses, two types of composites will be used. The first is an SSW-based composite, which is specific for each definition according to its detected events. All SSWs are included in the composites of each method, regardless of its winter period, unless otherwise stated. Our results hold when the analysis is performed over the December–February period (common to all definitions). The second is a multimethod mean (MMM), constructed from the SSW-based composites of all methods derived from the first type. Similar results were obtained using other compositing approaches that minimize the influence of outliers (e.g., scaled composites weighted by the standard deviation). The standard deviation of a SSW-based composite (intramethod spread)

will be denoted as σ, while σ_M will indicate the inter-method spread associated to the MMM. To assess the statistical significance of the first type, we compute a Monte Carlo test of 1000 samples with the same number of cases as in the composite. In each sample, the days and months of the selected cases are fixed to those of the original SSW onset dates and only the years are chosen randomly. The signal is statistically significant when the corresponding value in the SSW-based composite is outside of the 5th to 95th percentiles of the Monte Carlo distribution. The robustness of the MMM signal is assessed by computing the percentage of methods that agree on the sign and significance. The SSW signal is considered robust across definitions when the agreement is higher than 75%.

3. Results

Our analyses have been performed on the eight selected definitions and applied to ERA, JRA-55, and NCEP–NCAR reanalysis data for the 1958–2014 period. We have chosen these three datasets because they are the only ones that include stratospheric data and extend back beyond 1979. While for several methods we have identified differences across datasets in the exact dates of SSW occurrence or even in the number of the detected SSWs, a pairwise t test comparison of the reanalysis results for the decadal frequency of SSWs revealed no significant differences at the 95% confidence level in any of the methods analyzed in this study. In addition, the results shown later are not sensitive to the reanalysis product, and hence the conclusions of this paper are not affected by the reanalysis used, which is in agreement with Martineau and Son (2010). Given that one of the methods is only available for the ERA datasets, we will only show results from this reanalysis, unless otherwise stated. Some of the corresponding results for the JRA-55 and NCEP–NCAR datasets can also be found in the supplementary material. Further comparison among reanalysis products will be included in the ongoing Stratosphere–Troposphere Processes and Their Role in Climate (SPARC) Reanalysis Intercomparison Project (S-RIP) report (http://s-rip.ees.hokudai.ac.jp/).

a. Time distribution

The MMM frequency of SSWs is 6.7 events per decade, although there is considerable variability among definitions. Trate and Urate show frequencies larger than 9 events per decade because they detect a large number of events that are catalogued as minor warmings (Table S1). On the contrary, MOM and EOFz show the lowest frequencies (~5 events per decade). This is
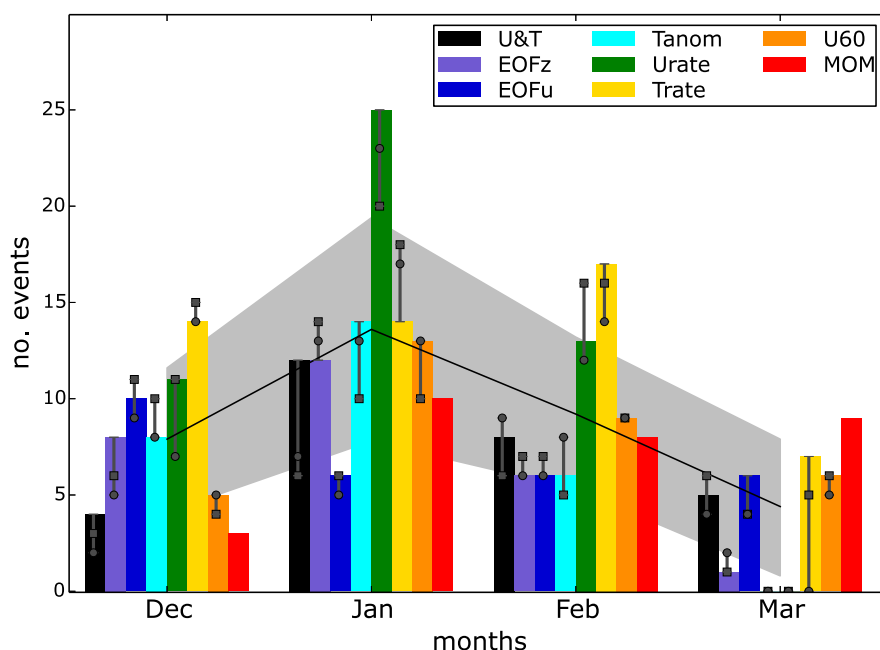
Fig. 2. Total monthly mean frequency distribution of SSWs for the 1960–2009 period. Color bars represent the number of events detected by each method (see legend). The black line represents the multimethod mean monthly frequency and the gray shadow denotes the ± 2-σ_M interval across methods. Gray squares (circles) indicate the corresponding values for the NCEP–NCAR (JRA-55) reanalysis.

related to the highly demanding threshold imposed on the NAM index in EOFz, and to the MOM tendency to capture many events in March, some of which were catalogued as final warmings (Table S1) and excluded from our analysis, as explained in section 2. To test whether the SSW frequencies are significantly different across methods, we have performed a pairwise comparison of the mean decadal frequencies. A t test revealed that 11 out of a total of 28 possible combinations were significantly different at the 95% confidence level. A binomial test was applied to assess collectively the significance of these differences, indicating that the probability of obtaining this result by chance is lower than 1%. Thus, the SSW frequency depends on the chosen definition (at 99% confidence level).

Figure 2 shows the monthly frequency distribution of SSWs for the eight different methods. The black line is the MMM, and the gray shading denotes the corresponding 2-σ_M interval. We restricted the analysis of Fig. 2 to the December–March period, which is covered by all methods except Urate and Tanom, whose analysis ends in February. Some methods also include October (EOFu and Trate), April (EOFu, U&T, and EOFz) or even May (Trate). However, no SSWs were detected later than March or earlier than November, and for the period of study only EOFu found a considerable number of SSWs in November, which partially results from our

redefinition of the onset dates (see section 2). In the remainder of the paper, all SSWs will be included, regardless of the winter period defined by each method.

Figure 2 shows similar distributions of SSWs, with the largest frequency in January in most definitions, except for Trate and EOFu. To evaluate the degree of dependence of the monthly distributions of events on the specific method, an analysis of variance (ANOVA; Wilks 2011) has been performed. This test is based on the comparison of the variance within two groups (e.g., the methods and the seasonal distribution) with the total variance. The ratio of these variances is given by the F factor, whose distribution follows a Fisher's F. Then, assuming the null hypothesis of similar population means within groups, the F factor is evaluated under an F test, thus determining whether the seasonal distribution depends or not on the method used. According to the ANOVA test, there is a significant seasonal variability in the occurrence of SSWs, which is statistically indistinguishable across methods at the 95% confidence level. This means that the seasonal cycle of SSWs is independent of the chosen method.

The decadal distribution of SSWs from 1960 to 2009 is shown in Fig. 3. In this case, the ANOVA test reveals that there is a significant amount of decadal variability associated with the occurrence of SSWs, but its decadal distribution does depend on the definition employed (at
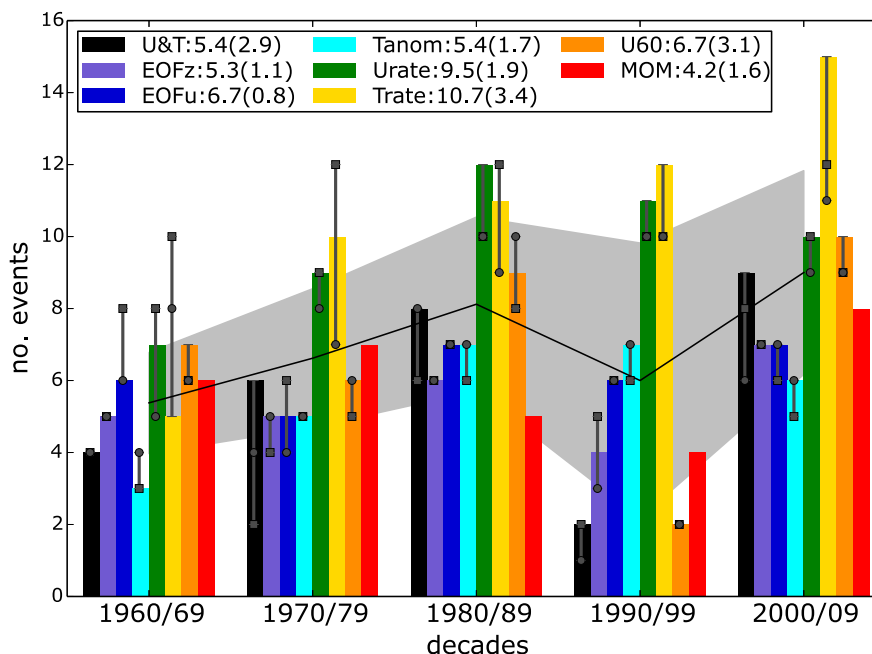
FIG. 3. As in Fig. 2, but for the total decadal distribution of events from the 1960s to the 2000s (only complete decades are shown). Numbers next to the legend show the average decadal frequency of SSWs for each method with its interdecadal standard deviation in parentheses. Gray squares (circles) indicate the corresponding values for the NCEP–NCAR (JRA-55) reanalysis.

the 95% confidence level). EOFz and EOFu have the lowest decadal variability in their distributions, while U&T and U60 show the largest variances, with a pronounced minimum in the 1990s. The latter is in agreement with relatively cold stratospheric conditions (Naujokat and Pawson 1996) and fewer occurrences of wind reversals at 60°N during the 1990s (Butler et al. 2015). Interestingly, methods based on other diagnostic variables (e.g., Tanom) or methodological approaches (e.g., Urate and Trate) do not display anomalously low frequencies of SSWs in the 1990s. Thus, the widely reported drop in the occurrence of SSWs during the 1990s is not significantly different from the behavior in other decades when definitions other than U&T or U60 (i.e., major warmings) are used, and hence it must be considered method dependent. As methods including minor SSWs do not show lower frequencies in the 1990s, this result also implies a near-normal occurrence of minor warmings in this decade. Similar results are obtained for the seasonal and decadal distribution of SSWs in NCEP–NCAR and JRA-55 reanalyses (Figs. 2 and 3).

b. Characteristics of SSWs

1) LIFE CYCLE

To assess the performance of the methods in capturing the main signatures of SSWs in the polar stratosphere

and their temporal evolution, we have computed composites of different diagnostic variables for each day of the [−40, 40]-day period around the SSW onset (Fig. 4). Figure 4a shows the daily evolution of the 10-hPa ZMZW at 60°N for each definition. While U&T, EOFz, and U60 cross the $0\,\mathrm{m\,s^{-1}}$ threshold near the onset, Tanom, Trate, Urate, EOFu, and MOM do not reach the wind inversion, although the latter two remain close to it. However, when the 10-hPa ZMZW is analyzed at higher latitudes (e.g., 65°N), EOFu and MOM do cross the zero wind line, indicating certain latitudinal dependence of the ZMZW reversal (not shown).

Several methods display the minimum ZMZW some days later than the others (Fig. 4a). This time lag among definitions is also clearly seen in the composites of wind tendency (Fig. 4b) and the intensity of the warming (Fig. 4c), particularly for those methods based on short-term tendencies (Urate, Trate). The maximum wind deceleration (Fig. 4b) occurs some days before the SSW onset except in Urate and Trate, for which it peaks at the time of the SSW, as expected from their tendency-based approach to establish the onset dates. In addition to the different diagnostics used in the detection, the time lags are also influenced by the specific criterion adopted to set the onset day. While some definitions consider the onset date as the crossing-threshold day, others use the day when the polar vortex is more perturbed. All this
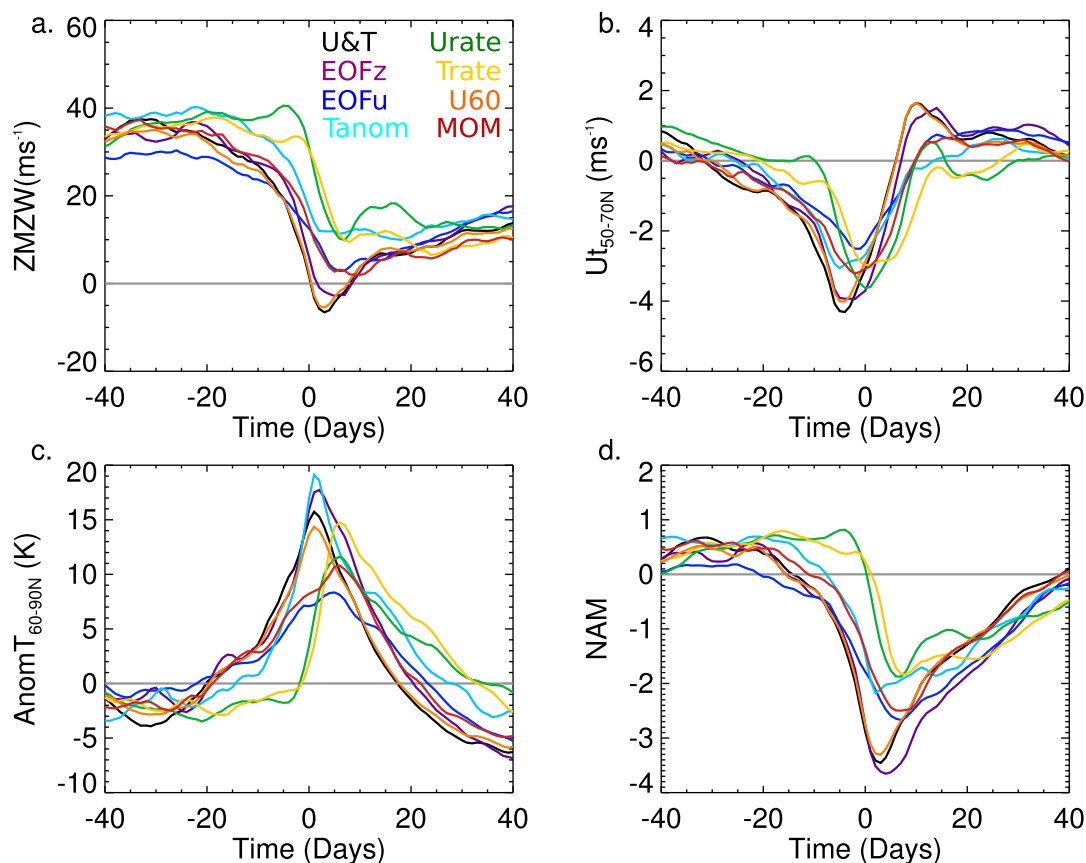
FIG. 4. Composites of different diagnostics at 10 hPa for the SSWs' life cycle: (a) zonal mean zonal wind (m s^{-1}), (b) time tendency of the zonal mean zonal wind area-weighted over 50°–70°N (m s^{-2}), (c) zonal mean temperature anomalies area-weighted over 60°–90°N (K), and (d) the NAM index (in standard deviation units). Each color line denotes a different method (see legend in the top left panel). The abscissa denotes time (in days) since the SSW onset.

explains why common events can be detected at different times of their life cycle in different methods (see Table S1). Note also that, for all definitions, the minimum in wind tendency occurs before the minimum ZMZW (Fig. 4a) and the largest warming (Fig. 4c). This is in agreement with theoretical expectations, as the minimum in the wind tendency is related to the strong wave dissipation in the polar stratosphere preceding the breakdown of the polar vortex (e.g., Andrews et al. 1987; Kodera 2006). Similarly, for all methods, the amplitude of the maximum warming is in good agreement with the magnitude of the wind deceleration (cf. Figs. 4b and 4c), as expected from the thermal wind balance.

The NAM index presents a minimum around the onset date in all methods (Fig. 4d). Overall, the evolution of the NAM index is very similar to that of the ZMZW. Thus, some methods place the minimum NAM value some days later than the detection of the event, and those that show the strongest easterly winds (Fig. 4a) also show the largest (negative) NAM values. In particular, the definitions that impose a wind reversal

(U&T and U60) reach NAM index values around −3 and show a similar behavior to EOFz, which identifies SSWs from a NAM index crossing threshold.

The overall comparison of all metrics shown in Fig. 4 reveals that the life cycle of the SSWs detected by EOFu displays weaker signatures than those reported by the other methods. As this is the only method based on data at 50 hPa (Table 1), we recomputed the life cycle composites by applying the EOFu definition at 10 hPa. In that case (not shown), the results displayed much better agreement with the other methods. This implies that the level chosen to detect SSWs can influence the life cycle of SSWs.

2) DYNAMICAL BENCHMARKS

Charlton and Polvani (2007) defined some benchmarks for SSWs based on time-averaged parameters around the SSW onset dates and they have been used in other studies (e.g., de la Torre et al. 2012) to validate the models' performance to reproduce SSW characteristics. However, the temporal windows for the calculations

were subjectively chosen according to the onset dates of the U60 definition and are not necessarily compatible with other methods included herein. To compare the different benchmarks across definitions, in our study, the time intervals have been modified to avoid biasing the results toward certain methods. Thus, we constructed the following benchmarks: 1) the amplitude of the SSWs in the midstratosphere, defined as the maximum 10-hPa warming rate over 50°–90°N and for the $[-20, 20]$-day period relative to the onset date of the SSW; 2) the maximum 10-hPa ZMZW deceleration rate at 60°N for the $[-20, 20]$-day period of the SSW; 3) the amplitude of the SSWs in the lower stratosphere, defined as in 1) but at 100 hPa; and 4) the troposphere–stratosphere coupling, as measured by the maximum anomaly of the zonal mean meridional eddy heat flux averaged over $(45–75)$°N at 100 hPa during the $[-30, 0]$-day period (i.e., an indicator of the upward propagation of tropospheric Rossby waves preceding SSWs). To avoid assigning short-lasting (i.e., daily) values to the benchmarks, the rating changes defined in benchmarks 1–3 are calculated as centered differences of 7-day mean periods separated by 8 days. As the time lags among the onsets of common events are usually lower than 30 days, this procedure also ensures that the same value of the benchmark is taken for common events, regardless of the definition employed in the detection.

To investigate the downward propagation of the SSW signatures through the lower stratosphere, a new benchmark has also been constructed. It accounts for the relative number of SSWs (with respect to the total number of SSWs) that display a sizable NAM signal response through the middle to the lower stratosphere and will be referred to as the ratio of propagating SSWs. These events have been identified by tracking negative NAM values in a time–height cross section from 10 hPa to the lower stratosphere. Our criterion of propagation is that the NAM value stays equal to or lower than -0.5 standard deviations as we descend in the stratosphere. We start by searching for the latest day (after the SSW onset) when the NAM value criterion is satisfied at 10 hPa. Then, for the so-detected day we move down to the following pressure level. From this point, we step forward (or backward) in time searching for the latest day with NAM values reaching that threshold. This procedure is repeated until 200 hPa; if at this level the criterion is satisfied at least 10 days after the onset, the event is considered as a propagating SSW. The -0.5 standard deviation value was chosen as a threshold because it provides an upper limit to the significant signal of the NAM composites (shown later in Fig. 6). Qualitatively, the results do not vary substantially if similar thresholds are used instead.

Note that a propagating event is not required to reach the troposphere.

Figures 5a–d show the SSW-based composites of each benchmark computed for each of the eight methods (colored squares) with their ± 2-σ levels, together with the MMM (black circle) and the associated ± 2-σ_M interval. The most outstanding result is the large dispersion of values within methods, which highlights a strong case-to-case variability for all definitions. These within-method changes are much larger than the intermethod spread, making the differences in the dynamical benchmarks among methods not statistically significant. The overall good agreement of benchmarks across methods confirms that the method discrepancies observed in Fig. 4 can be largely alleviated by accounting for the lags in the times of detection (as done in Fig. 5).

Even though the differences in the benchmarks are not significant, EOFu shows the smallest SSWs amplitudes (Fig. 5a) and wind deceleration rates (Fig. 5b) in the midstratosphere and the largest warming in the lower stratosphere (Fig. 5c). Again, this is related to the choice of 50-hPa data for the detection of SSWs (not shown). Interestingly, the signal-to-noise ratio (MMM/σ_M) for the SSW amplitude at 10 hPa is around 5 times larger than at 100 hPa (Figs. 5a,c). This indicates an increasing intermethod spread of the benchmarks toward the lower stratosphere, and suggests that discrepancies among methods in the SSWs signatures increase as we move down from the level of detection.

Figure 5e shows the relative number of propagating SSWs detected by each method. On average, nearly 70% of the SSWs are propagating events. There is agreement between the two definitions that explicitly demand ZMZW reversal (i.e., U&T and U60) but although they only include major warmings, they show lower ratios of propagating SSWs than EOFz and EOFu. This agrees with Baldwin and Thompson (2009), who showed that NAM-like indices can lead to stronger stratosphere–troposphere coupling than SSWs based on ZMZW reversal at 60°N. On the other hand, there is large variability in the number of propagating events among the methods with the largest percentage of minor warmings (i.e., Tanom, Trate, and Urate). This may indicate discrepancies in the propagating behavior of minor SSWs. Note, however, that benchmarks are affected by a large dispersion in all methods, which makes it difficult to establish robust conclusions based solely on the mean values of these diagnostics. Thus, in the next section, we will analyze in more detail how major and minor SSWs contribute to the discrepancies in the resulting tropospheric signal and surface impacts of SSWs.
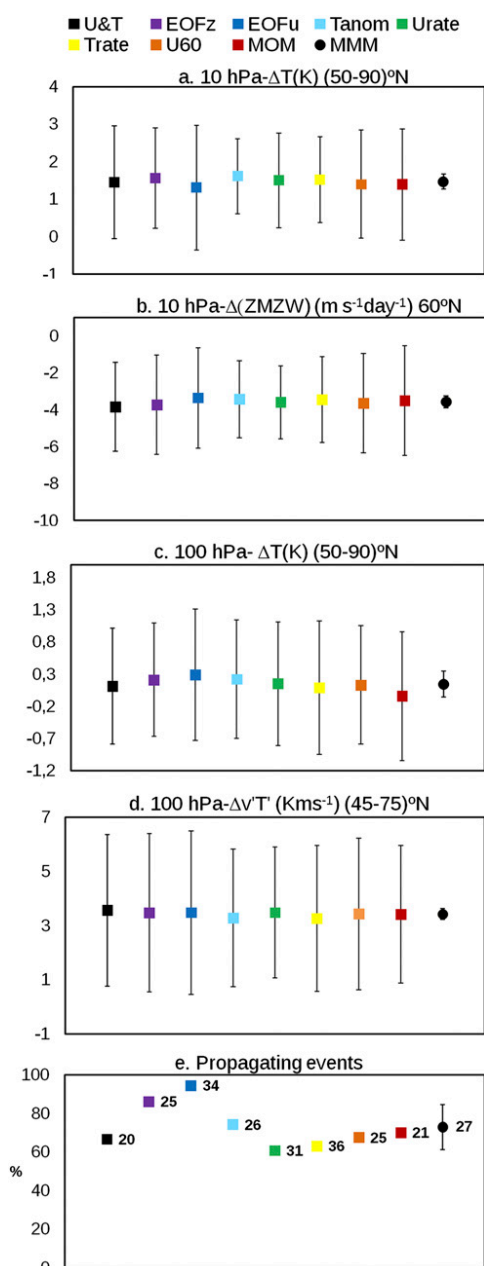
FIG. 5. SSW-based composites of dynamical benchmarks for the different methods (colored squares; see legend) and the corresponding ± 2-σ interval (whiskers): (a) maximum 10-hPa warming rate area-weighted over 50°–90°N (in K), (b) maximum 10-hPa zonal mean zonal wind deceleration rate at 60°N (in m s^{-1} day^{-1}), and (c) maximum 100-hPa warming rate area-weighted over 50°–90°N (in K). For (a)–(c), daily rates are computed as centered differences of 7-day mean periods and the maximum value is chosen over the [−20, 20]-day interval around the onset date. Also shown are (d) maximum 100-hPa $\overline{v'T'}$ anomaly area-weighted over 45°–75°N in the [−30, 0]-day period before the onset date (in K m s^{-1}) and (e) percentage of propagating events into the lower stratosphere (relative to the total number of SSWs), with numbers showing the absolute number of propagating events (see text for details). Black circles and the associated whiskers are the multimethod mean (MMM) of each benchmark and the ± 2-σ_M interval among methods, respectively.

c. Downward propagation signal and surface effects of SSWs

1) DOWNWARD PROPAGATION

The downward propagating signal of the SSWs can be better illustrated by computing the cross-section SSW-based composite of the NAM index for the [−90, 90]-day period around the onset dates of the SSWs, as shown in Fig. 6 for each of the eight methods. All definitions show the typical "dripping paint" pattern of the NAM illustrated by Baldwin and Dunkerton (2001), with persistent negative NAM values propagating downward after the occurrence of SSWs. However, not all the methods show this stratosphere–troposphere coupling with equal intensity. The strongest tropospheric NAM response is found for EOFz and EOFu. As mentioned above, this is very likely related to the NAM-based definition of EOFz, and a similar reasoning could be sustained for EOFu, as both definitions account for the first mode of variability in the winter stratosphere. However, the level used in EOFu to detect SSWs (50 vs 10 hPa) also plays an important role in modulating the tropospheric response. In fact, when the EOFu procedure is applied at 10 hPa, the downward signal weakens (not shown). In addition, these two methods are those showing the largest ratios of propagating events into the lower stratosphere (Fig. 5e). This could indicate a relationship between the ratio of propagating events and the amplitude of the tropospheric response. However, this behavior is not observed in methods with a large fraction of minor warmings (see Fig. 6). For example, Tanom shows a high ratio of propagating events into the lower stratosphere (70%) but the tropospheric response is one of the weakest (together with Urate and Trate; cf. Figs. 6d–f). One possible explanation could be that the largest relative frequency of minor SSWs in these methods is weakening the NAM signal observed for the other definitions. This possible influence of minor SSWs will be analyzed later.

To evaluate the level of agreement among methods, Figs. 7a and 7b show the MMM composite of the NAM signal (computed from panels of Fig. 6) and the intermethod spread, respectively. Despite the considerable dispersion of NAM values around the onset date of SSWs, the MMM displays a robust downward propagating NAM pattern in the stratosphere across methods. On the contrary, there are substantial differences among methods in the significance and even the sign of the NAM response in the troposphere, as reflected by the reduced multimethod agreement therein (cross-hatched areas in Fig. 7a). The intermethod spread in the NAM
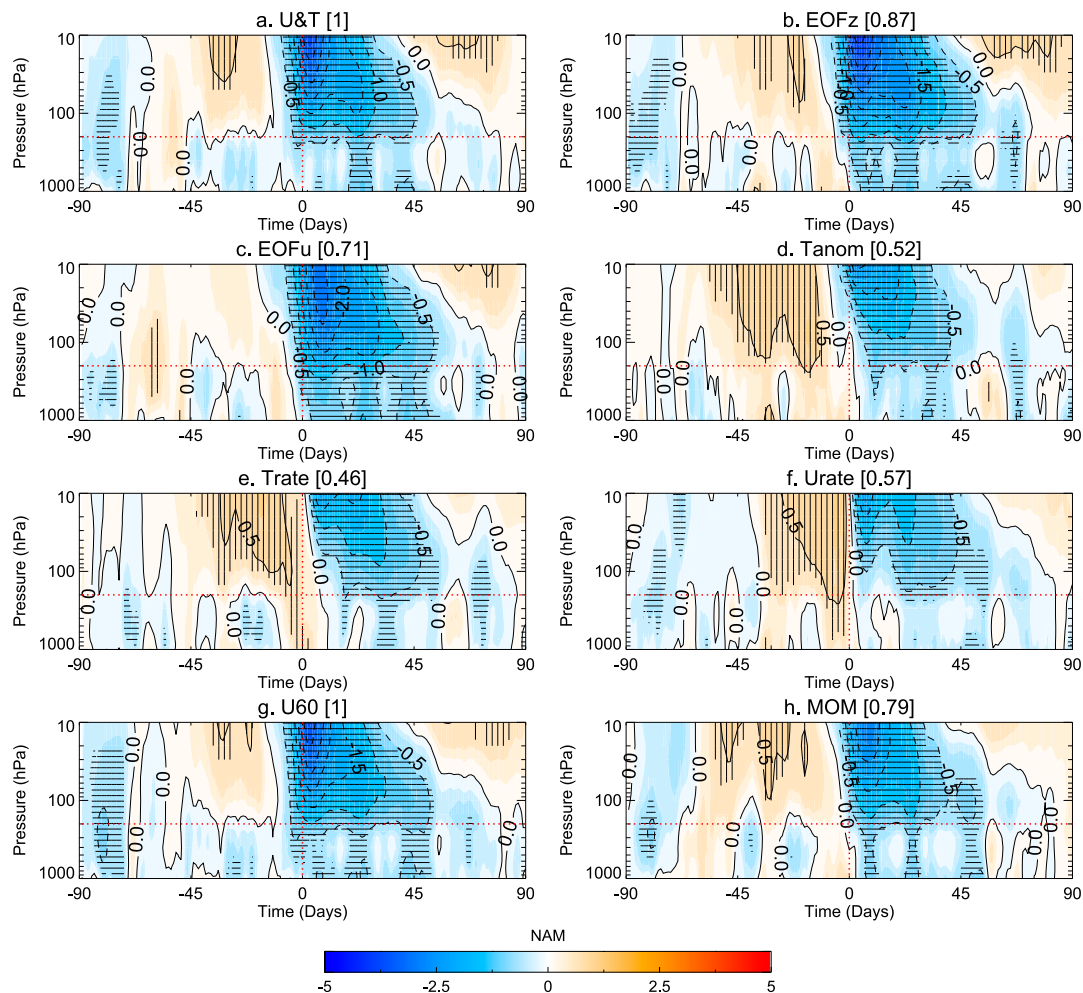
FIG. 6. Time–height composites of the northern annular mode (NAM) index (in standard deviation units) for SSWs events detected by (a) U&T, (b) EOFz, (c) EOFu, (d) Tanom, (e) Trate, (f) Urate, (g) U60, and (h) MOM. Numbers next to the titles indicate the relative frequency of major SSWs (with respect to the total number of events) detected by each method. Solid (dashed) lines denote positive (negative) NAM values. The abscissa denotes days relative to the SSW onset date. The red horizontal line highlights the 200-hPa pressure level (approximately the extratropical tropopause). Horizontal (vertical) hatched areas indicate negative (positive) anomalies that are statistically significant at the 95% confidence level according to a 1000-trial Monte Carlo test.

values around the day of detection in the stratosphere (Fig. 7b) is largely due to discrepancies in dating the SSWs. To illustrate this, we have readjusted all the SSW onsets to the date of minimum NAM index at 10 hPa. Thus, for every event, the onset is reassigned by searching the day with the minimum NAM value in a temporal window from 10 days before the earliest detection to 10 days after the latest detection among methods. This condition is applied to all SSWs, not only to common events. The MMM composite with the readjusted dates (Fig. 7c) shows stronger signals and better agreement across methods, as shown by the intermethod spread σ_M (Fig. 7d), which is now largely reduced. To test the robustness of these results to the

reanalysis product, we have repeated the MMM analysis using the NCEP–NCAR and JRA-55 data products (Fig. S1). Despite the weaker signal in the NCEP–NCAR MMM, the three reanalyses show a robust downward NAM propagation across methods. From this point, all the analyses will be performed using the readjusted onset dates. Next, we evaluate to what extent major and minor events contribute to the discrepancies among methods, as previously suggested. To do so, we have computed the MMM and intermethod spread for major and minor events separately. The downward propagation of major SSWs (Fig. 7e) shows a similar picture to the MMM of all events, but the NAM signals around the onset and the tropospheric response are
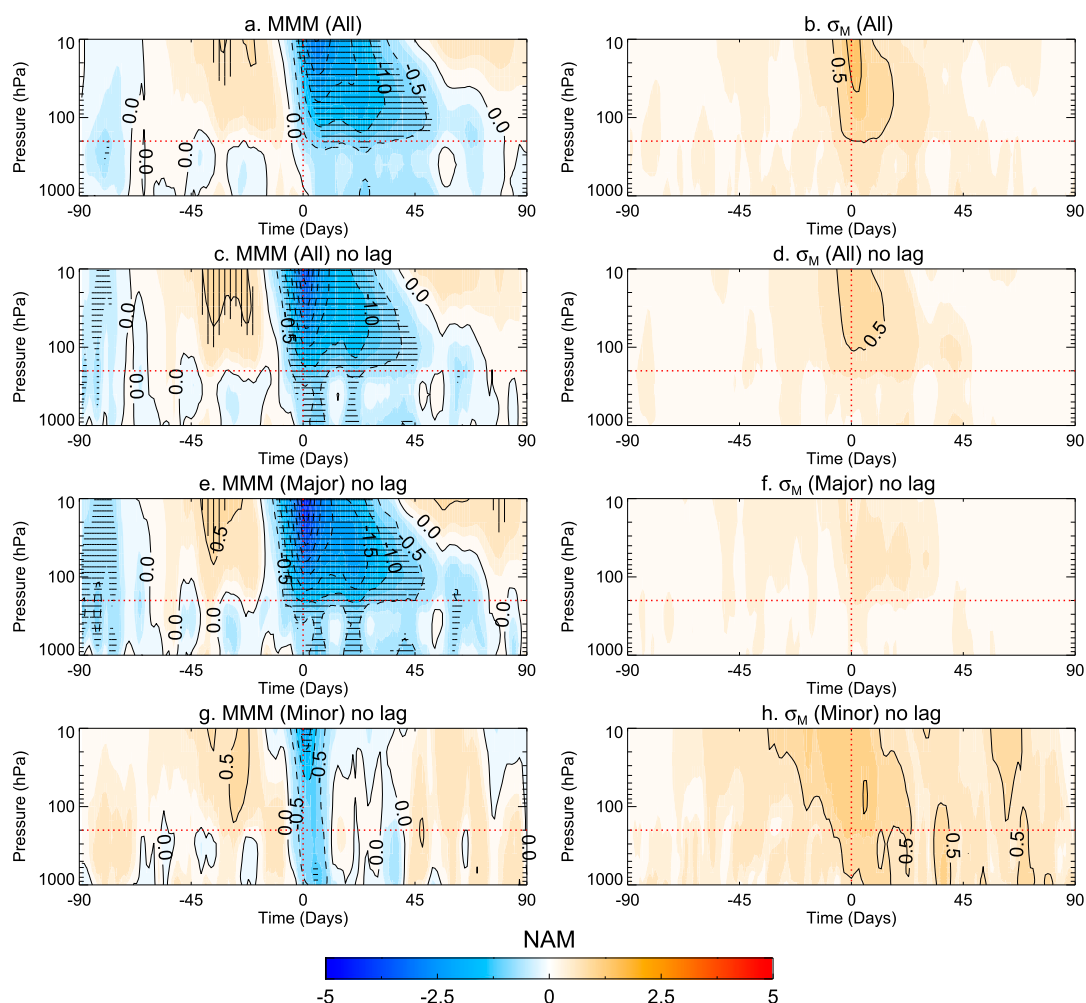
FIG. 7. (left) Multimethod means (MMMs) of the time–height NAM index composites (in standard deviation units) for (a) all SSWs, and (c),(e),(g) all, major, and minor SSWs with the readjusted onset dates (see text for details). Note that U&T and U60 are not included in the minor SSW MMM. (right) Intermethod standard deviation (σ_M) of the time–height NAM composites for (b) all SSWs, and (d),(f),(h) all, major, and minor SSWs with the readjusted onset dates. Solid (dashed) lines denote positive (negative) NAM values. The abscissa denotes days relative to the SSW onset date. The red horizontal line indicates the 200-hPa pressure level (i.e., approximately the extratropical tropopause). Hatched areas indicate regions where more of 75% of the methods agree in the sign and significance of the NAM signal.

stronger and more robust. Moreover, the intermethod spread σ_M (Fig. 7f) is noticeably reduced as compared to that of all SSWs (Fig. 7c). For minor warmings, the MMM (Fig. 7g) displays a weak and short-lasting downward propagation after the SSW onset, and large discrepancies among methods, as indicated by σ_M (Fig. 7h). In fact, the composites of minor SSWs for individual definitions show very different results (Fig. S2). In particular, EOFz and EOFu display significant propagation signals, albeit less persistent than that for major SSWs, while the others show weak negative NAM values around the onset, without clear downward propagation. Therefore, the large rates of minor SSWs

in Tanom, Urate, and Trate can explain the weaker NAM propagation signals found in their all-SSWs composites.

Finally, the very small discrepancies (σ_M) among the composites of major SSWs suggest that these events may be detected by several methods and thus may be common events. Table 2 corroborates this hypothesis. It reveals that the conditional probability of an event for being major SSW grows with the number of methods that capture it. Thus, if one event is detected by half or more of the methods (i.e., 4 out of 8), the probability of being a major SSW is ~88%. On the contrary, minor SSWs are less prone to be common events. Therefore,

TABLE 2. Probability of an event being a major/minor SSW given the number of methods that detect it. Each cell shows the conditional probability (i.e., the number of major/minor events detected in *n* or more methods divided by the total number of events detected in *n* or more methods). Note that for each *n*, the conditional probability for minor warmings is complementary to that of major warmings.

	≥2 methods (9 events)	≥3 methods (15 events)	≥4 methods (7 events)	≥5 methods (3 events)	≥6 methods (24 events)
Major	0.66	0.69	0.88	0.96	1.0
Minor	0.34	0.31	0.12	0.04	0.0

given the inherent case-to-case variability of SSWs (see section 3b), the inclusion of minor SSWs contributes notably to the intermethod discrepancies in the zonal mean tropospheric signals of SSWs, as minor events are more likely to be exclusive of each method.

2) SURFACE IMPACT AND TROPOSPHERIC PRECURSORS

Figures 8 and 9 show the MMMs of the MSLP anomalies [5, 35] days after and [−40, −10] days before the events, respectively. These time intervals were selected according to the NAM composites of Fig. 7 and the onset dates were readjusted as previously described. However, and similar to the previous section, the conclusions here remain if the original SSW onsets are used, although the signal is not so strong (not shown). The MMMs of major and minor SSWs are also shown in Figs. 8 and 9 (middle and right panels, respectively), together with their σ_M values (bottom panels). Individual composites for each method are shown in Figs. S3 and S4.

Overall, the MMM of MSLP after all SSWs (Fig. 8a) shows positive anomalies over the polar cap and negative anomalies over Europe, in agreement with Fig. 7 and previous studies (e.g., Limpasuvan et al. 2004; Charlton and Polvani 2007). However, high agreement among methods is mainly restricted to the polar cap only. This negative NAM pattern is more robust across methods when including only major warmings (Fig. 8b), and becomes weaker and not robust in the MMM of minor SSWs (Fig. 8c). Similar to the downward propagation of the SSW signals, the intermethod spread reveals better agreement across definitions in the major warming signatures (Fig. 8e), since most of them are common events, while the largest differences among methods are associated with minor SSWs (Fig. 8f). In fact, Fig. S3 indicates that there is not a unique response pattern across definitions after minor SSWs. EOFz and EOFu show similar NAM patterns after major and minor SSWs, albeit much weaker for the latter, consistent with the results shown for the downward propagation of the NAM signal. However, the other definitions display different patterns after minor warmings, which vary from method to method and show significant responses over small regions only, thus revealing a strong method dependence on the surface impact of these events.

Finally, we compare the MSLP precursor signal of SSWs, computed for the [−40, −10]-day period before the onset dates (Fig. 9). The MMM shows negative anomalies over northern North America and North Pacific and positive anomalies in Eurasia and is qualitatively similar to that obtained in previous studies for certain individual definitions (e.g., Limpasuvan et al. 2004; Cohen and Jones 2011). The MMM precursor pattern of SSWs shows higher agreement across methods than the MMM response to SSWs (Fig. 8a) and is also robust when only major warmings are considered (Fig. 9b). However, the MMM precursor signal of minor SSWs does not show a robust pattern (Fig. 9c), in agreement with the large σ_M values (Fig. 9f). In addition, the discrepancies between major and minor SSWs precursors are larger than those found for the SSWs responses (mainly in the Atlantic). Note that this result does not imply the absence of surface precursors for minor SSWs. Instead, Fig. S4 reveals significant surface signals prior to minor SSWs, but these are largely variable among methods, leading to a weak agreement in the MMM. Again, this corroborates that minor SSWs—those warmings that do not reverse the circulation—are the main source of discrepancies among the definitions.

4. Conclusions and discussion

In this study we have compared the occurrence of SSWs and their signatures among eight different definitions of SSWs, using three reanalysis datasets. Overall, the differences among reanalyses are much smaller than those across definitions. More specifically, no significant differences were found in the decadal frequencies of SSW among ERA, NCEP–NCAR, and JRA-55 reanalysis for any of the definitions, and the conclusions shown here are fairly robust to the reanalysis. Our main findings in the intermethod comparison are the following:

1) The mean frequency of SSWs is 6.7 events per decade, but it is method dependent, with some of
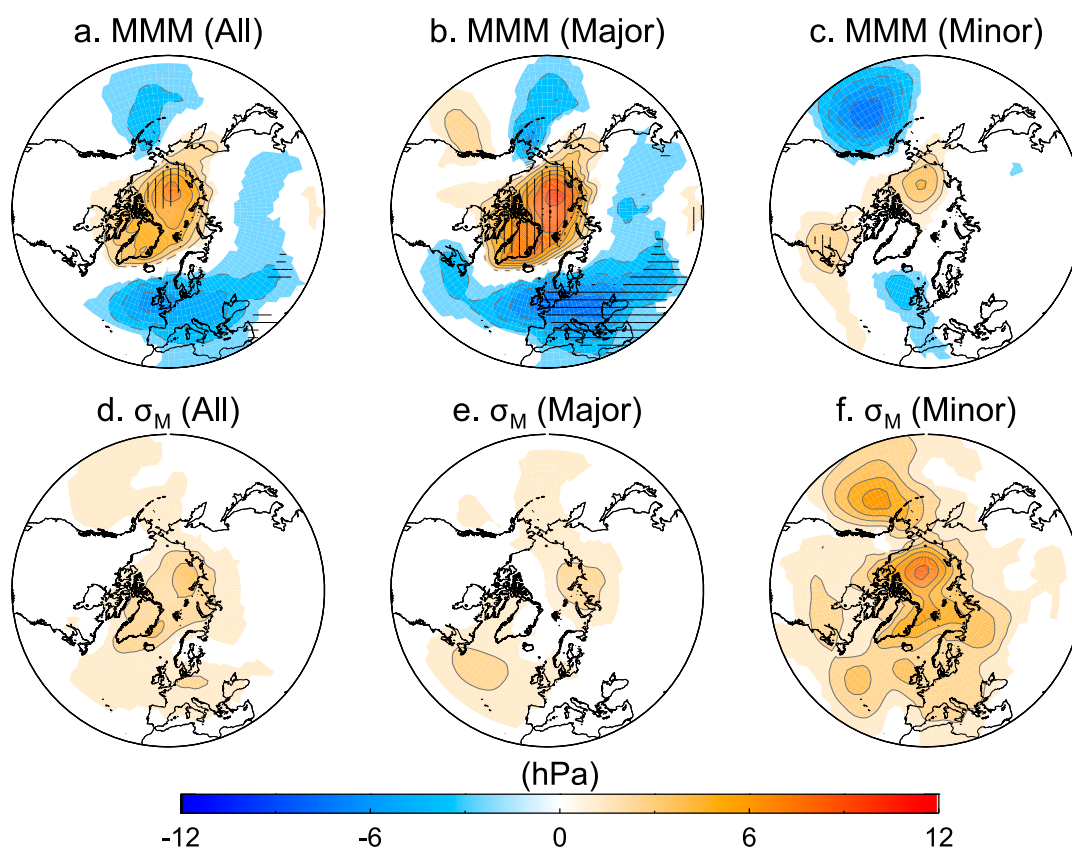
[5,35]-day period

FIG. 8. (top) Multimethod means (MMM) of the mean sea level pressure (MSLP) anomalies (in hPa) for the [5, 35]-day period after (a) all, (b) major, and (c) minor SSWs. (bottom) Intermethod standard deviation (σ_M) of the MSLP composites for (d) all, (e) major, and (f) minor SSWs. Values between -0.5 and 0.5 are unshaded. Hatched areas indicate regions where more of 75% of the methods agree in the sign and significance of the MSLP signal. Results are shown for the readjusted onset dates.

the definitions that consider minor warmings reaching frequencies larger than 10 events per decade. All methods show indistinguishable intraseasonal distributions of SSWs at the 95% confidence level, with the largest occurrence in January. In contrast, the decadal variability of SSWs depends on the method. Only definitions based on wind reversal at 60°N show significant minimum frequencies in the 1990s.

2) The temporal evolution of different variables in the stratosphere through the SSW life cycle reveals lags among some definitions. These time lags are due to the use of different variables, approaches (instantaneous or rating changes values), and criteria adopted for dating the onset (e.g., peak values or crossing thresholds). These methodological issues involve different events and detection dates across definitions. In particular, methods based on wind and temperature rates tend to detect SSWs earlier than

the others. Nevertheless, these lags are not a major issue and can be easily corrected by readjusting the onset dates (e.g., by redefining the onset as the day of minimum NAM index in a given time interval around the detection).

3) The mean values of the SSW dynamical benchmarks are not statistically different across definitions due to large case-to-case variability within methods. Although the multimethod agreement decreases for lower stratospheric benchmarks, the intramethod variability is still larger than the intermethod spread, which highlights the strong differences among events for a given definition.

4) One of the methods included herein (i.e., EOFu) is based on data at 50 hPa, instead of the traditional 10-hPa level included in the other definitions. Using this lower level leads to discrepancies with other methods in several SSW features. This suggests that the

52

[-40,-10]-day period

a. MMM (All)

b. MMM (Major)

c. MMM (Minor)

d. σ_M (All)

e. σ_M (Major)

f. σ_M (Minor)

(hPa)

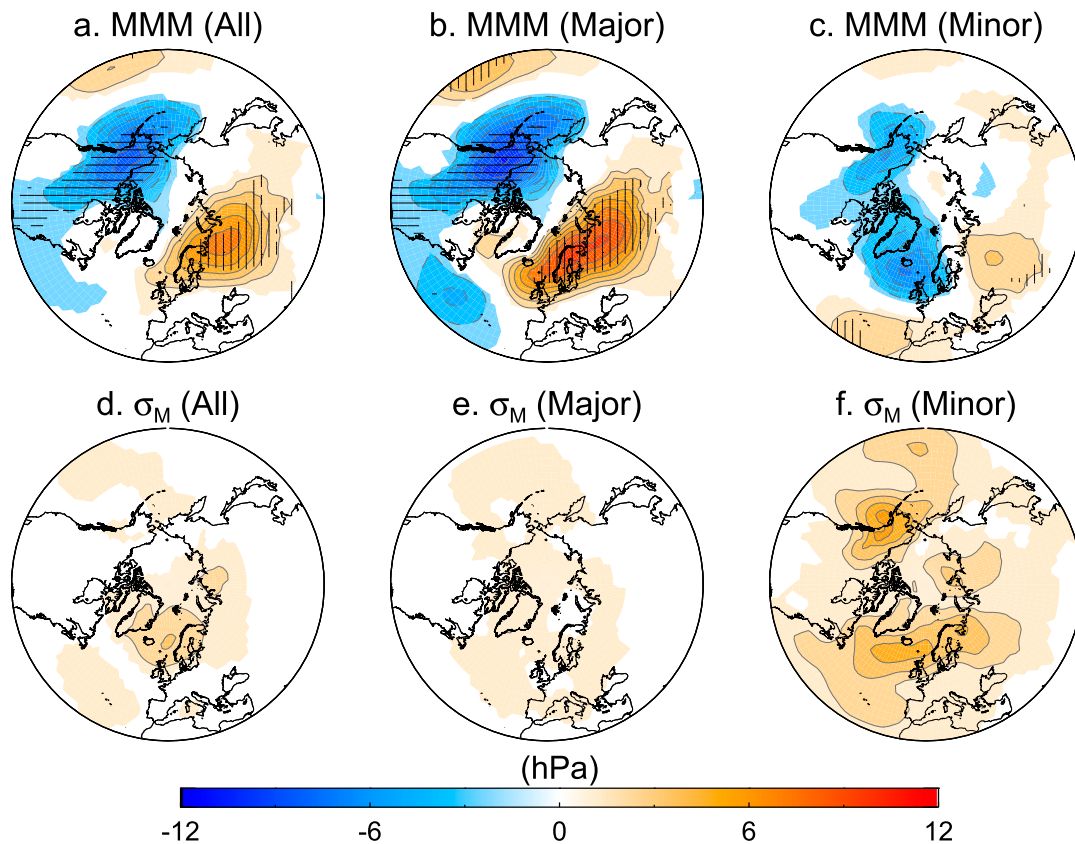-12   -6   0   6   12

FIG. 9. As in Fig. 8, but for the $[-40, -10]$-day period prior to events.

chosen level for the detection plays a role in modulating the SSW signatures.

5) All methods show a significant downward propagation of the negative NAM signal from 10 hPa to the lower stratosphere, persisting therein for more than 45 days after the SSW onset. However, not all methods show the same level of stratosphere–troposphere coupling. The strength of the coupling, as measured by the NAM index, is affected by the relative frequency of minor SSWs (with respect to the total number of events) detected in each definition. Overall, methods with larger ratios of minor SSWs involve weaker NAM propagating signals.

6) Minor SSWs are also the main source of uncertainty in the precursor and response signals of SSWs at the surface. In contrast, major SSWs show significant NAM-like patterns at the surface that are robust across definitions, since they are more likely detected by most methods.

Therefore, any of the definitions analyzed here would be equally suitable for further research on the seasonal cycle, dynamical benchmarks, and life cycle of SSWs. However, the decadal variability of SSWs is sensitive to the chosen definition, which calls for caution in studies of low-frequency variability and trends of SSWs. There are also substantial differences among methods in the tropospheric signal before and after SSWs, with the relative frequency of minor SSWs being an important source of discrepancy. This indicates that only major warmings in which wind reverses its sign should be considered to obtain robust results. This is particularly relevant when SSW occurrence is used to improve winter weather predictability or to explore tropospheric precursors of SSWs.

Since a discussion on a new SSW definition is undergoing (Butler et al. 2014), the results presented here lead us to suggest the following recommendations, which may contribute to the decision making:

• Revision of the vertical level of detection. We have found that the pressure level used to detect SSWs plays a role in modulating the downward propagation
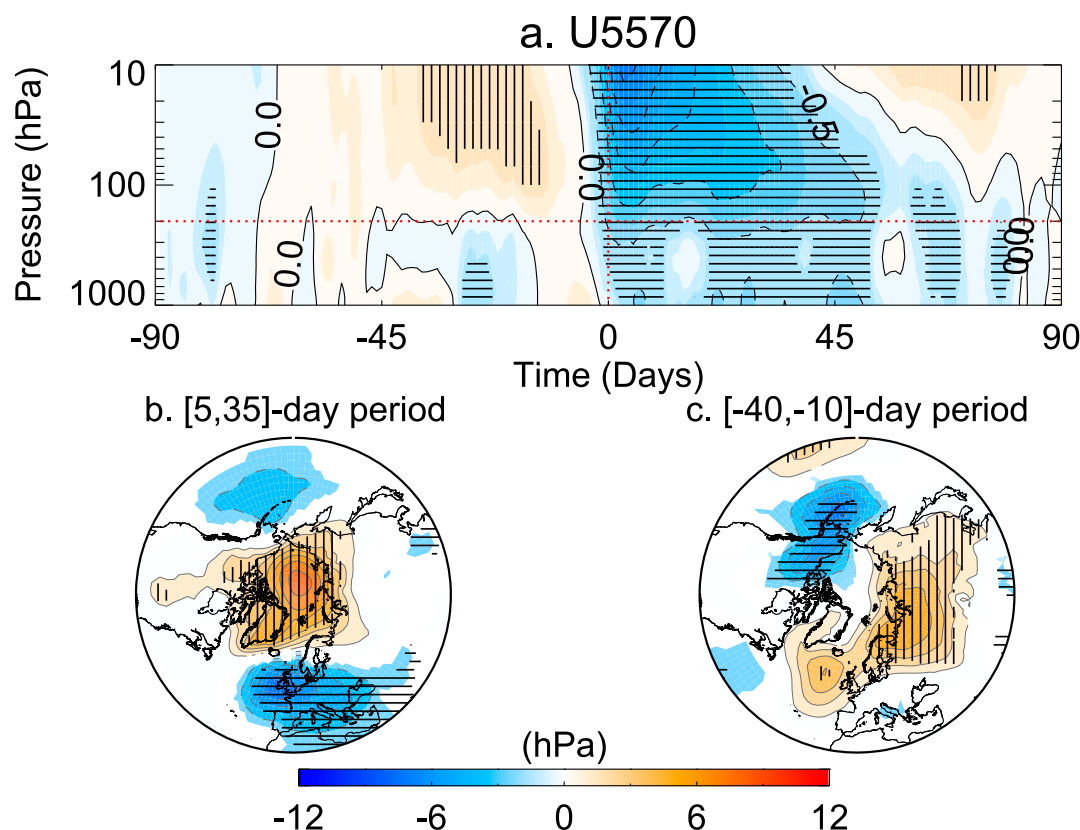
53

FIG. 10. (a) As in Fig. 6, but for the U5570 method. Also shown are MSLP anomalies composites for (b) the [5–35]-day period after and (c) the [−40, −10]-day period before SSW occurrence. Values of the MSLP anomalies between −0.5 and 0.5 are unshaded. Horizontal (vertical) hatched areas indicate negative (positive) anomalies that are statistically significant at the 95% confidence level according to a 1000-trial Monte Carlo test.

signal, with 50 hPa leading to stronger responses in the troposphere than the traditional 10-hPa level. While this may argue for choosing the lower level, our view is that the detection of the SSW should be independent of its impacts. On the other hand, previous studies have shown that 10 hPa may not be the most suitable level to define SSWs because of potential artifacts at this specific level associated with the incorporation of satellite data in reanalyses extending back beyond 1979 (Gómez-Escolar et al. 2012, and references therein) and hence it should be revised.

- Revision of the latitude of detection. Previous analyses (e.g., Butler et al. 2015) have shown that the SSW detection performed by the wind-reversal methods depends on the latitude chosen, and several alternatives (65°N or a latitudinal average) have been suggested. We rather propose evaluating the ZMZW reversal within a latitudinal range. This has the advantage of assuring that the detection includes the polar vortex edge, even in climate change scenarios and models with vortex biases.

To test this methodology we have identified events for which the 10-hPa ZMZW reversal occurs in at least one of the latitudes between 55° and 70°N (U5570 hereafter). The results obtained with this definition are consistent with the MMM values found in this paper and do not show outliers (see Fig. 10 and Fig. S5). Similar to most of the methods explored here, the minimum occurrence of major SSWs in the 1990s (as found in U&T and U60) diminishes, and although the frequency of occurrence in U5570 is comparable to methods including minor warmings (e.g., Trate), the new captured events show a major warming–like behavior in the downward propagation signal, which is similar to that shown by the definitions with the strongest stratosphere–troposphere coupling (cf. Figs. 6 and 10a). Additionally, the surface responses and precursors captured by U5570 show significant and coherent patterns, similar to those depicted by the major MMM composites (Figs. 10b,c).

- Minimizing minor SSWs detection. As shown in this study, the specific variables and criteria adopted in the

new definition might not be as relevant as long as it keeps the detection of minor SSWs to a minimum. Thus, efforts to define SSWs should aim to minimize minor warming events.

REFERENCES

Andrews, D. G., J. R. Holton, and C. B. Leovy, 1987: *Middle Atmosphere Dynamics.* International Geophysics Series, Vol. 40, Academic Press, 489 pp.

Baldwin, M. P., and T. J. Dunkerton, 2001: Stratospheric harbingers of anomalous weather regimes. *Science,* **294,** 581–584, doi:10.1126/science.1063315.

——, and D. W. J. Thompson, 2009: A critical comparison of stratosphere–troposphere coupling indices. *Quart. J. Roy. Meteor. Soc.,* **135,** 1661–1672, doi:10.1002/qj.479.

Bancalá, S., K. Krüger, and M. Giorgetta, 2012: The preconditioning of major sudden stratospheric warmings. *J. Geophys. Res.,* **117,** D04101, doi:10.1029/2011JD016769.

Barriopedro, D., and N. Calvo, 2014: On the relationship between ENSO, stratospheric sudden warmings, and blocking. *J. Climate,* **27,** 4704–4720, doi:10.1175/JCLI-D-13-00770.1.

Blume, C., K. Matthes, and I. Horenko, 2012: Supervised learning approaches to classify sudden stratospheric warming events. *J. Atmos.,* **69,** 1824–1840, doi:10.1175/JAS-D-11-0194.1.

Butler, A. H., E. P. Gerber, D. Mitchell, and W. Seviour, 2014: New efforts in developing a standard definition for sudden stratospheric warmings. *SPARC Newsletter,* No. 43, SPARC Office, Toronto, ON, Canada, 23–24.

——, D. J. Seidel, S. C. Hardiman, N. Butchart, T. Birner, and A. Match, 2015: Defining sudden stratospheric warmings. *Bull. Amer. Meteor. Soc.,* doi:10.1175/BAMS-D-13-00173.1, in press.

Charlton, A. J., and L. M. Polvani, 2007: A new look at stratospheric sudden warmings. Part I: Climatology and modeling benchmarks. *J. Climate,* **20,** 449–469, doi:10.1175/JCLI3996.1.

Cohen, J., and J. Jones, 2011: Tropospheric precursors and stratospheric warmings. *J. Climate,* **24,** 6562–6572, doi:10.1175/2011JCLI4160.1.

Dee, D. P., and Coauthors, 2011: The ERA-Interim reanalysis: Configuration and performance of the data assimilation system. *Quart. J. Roy. Meteor. Soc.,* **137,** 553–597, doi:10.1002/qj.828.

de la Torre, L., R. R. Garcia, D. Barriopedro, and A. Chandran, 2012: Climatology and characteristics of stratospheric sudden warmings in the Whole Atmosphere Community Climate Model. *J. Geophys. Res.,* **117,** D04110, doi:10.1029/2011JD016840.

Ebita, A., and Coauthors, 2011: The Japanese 55-year Reanalysis "JRA-55": An interim report. *SOLA,* **7,** 149–152, doi:10.2151/sola.2011-038.

Gómez-Escolar, M., S. Fueglistaler, N. Calvo, and D. Barriopedro, 2012: Changes in polar stratospheric temperature climatology in relation to stratospheric sudden warming occurrence. *Geophys. Res. Lett.,* **39,** L22802, doi:10.1029/2012GL053632.

Hannachi, A., D. Mitchell, L. Gray, and A. Charlton-Perez, 2011: On the use of geometric moments to examine the continuum of sudden stratospheric warmings. *J. Atmos. Sci.,* **68,** 657–674, doi:10.1175/2010JAS3585.1.

Kalnay, E., and Coauthors, 1996: The NCEP/NCAR 40-Year Reanalysis Project. *Bull. Amer. Meteor. Soc.,* **77,** 437–471, doi:10.1175/1520-0477(1996)077<0437:TNYRP>2.0.CO;2.

Kodera, K., 2006: Influence of stratospheric sudden warming on the equatorial troposphere. *Geophys. Res. Lett.,* **33,** L06804, doi:10.1029/2005GL024510.

——, Y. Kuroda, and S. Pawson, 2000: Stratospheric sudden warmings and slowly propagating zonal-mean zonal wind anomalies. *J. Geophys. Res.,* **105,** 12 351–12 359, doi:10.1029/2000JD900095.

Labitzke, K., 1981: Stratospheric-mesospheric midwinter disturbances: A summary of observed characteristics. *J. Geophys. Res.,* **86,** 9665–9678, doi:10.1029/JC086iC10p09665.

——, and B. Naujokat, 2000: The lower Arctic stratosphere in winter since 1952. *SPARC Newsletter,* No. 15, SPARC Office, Toronto, ON, Canada, 11–14.

Limpasuvan, V., D. W. J. Thompson, and D. L. Hartmann, 2004: The life cycle of the Northern Hemisphere sudden stratospheric warmings. *J. Climate,* **17,** 2584–2596, doi:10.1175/1520-0442(2004)017<2584:TLCOTN>2.0.CO;2.

Martineau, P., and S.-W. Son, 2010: Quality of reanalysis data during stratospheric vortex weakening and intensification events. *Geophys. Res. Lett.,* **37,** L22801, doi:10.1029/2010GL045237.

——, and ——, 2013: Planetary-scale wave activity as a source of varying tropospheric response to stratospheric sudden warming events: A case study. *J. Geophys. Res. Atmos.,* **118,** 10 994–11 006, doi:10.1002/jgrd.50871.

Matsuno, T., 1971: A dynamical model of the stratospheric sudden warming. *J. Atmos. Sci.,* **28,** 1479–1494, doi:10.1175/1520-0469(1971)028<1479:ADMOTS>2.0.CO;2.

Matthewman, N. J., J. G. Esler, A. J. Charlton-Perez, and L. M. Polvani, 2009: A new look at stratospheric sudden warmings. Part III: Polar vortex evolution and vertical structure. *J. Climate,* **22,** 1566–1585, doi:10.1175/2008JCLI2365.1.

McInturff, R. M., 1978: Stratospheric warmings: Synoptic, dynamic and general-circulation aspects. NASA Ref. Publ. 1017, 19 pp.

Mitchell, D. M., A. J. Charlton-Perez, and L. J. Gray, 2011: Characterizing the variability and extremes of the stratospheric polar vortices using 2D moment analysis. *J. Atmos. Sci.,* **68,** 1194–1213, doi:10.1175/2010JAS3555.1.

Nakagawa, K. I., and K. Yamazaki, 2006: What kind of stratospheric sudden warming propagates to the troposphere? *Geophys. Res. Lett.,* **33,** L04801, doi:10.1029/2005GL024784.

Naujokat, B., and S. Pawson, 1996: The cold stratospheric winters 1994/1995 and 1995/1996. *Geophys. Res. Lett.,* **23,** 3703–3706, doi:10.1029/96GL03614.

Scherhag, R., 1952: Die explosionsartige Stratosphärenerwarmungen des Spätwinters, 1951–1952. *Ber. Dtsch. Wetterdienst,* **38,** 51–63.

Seviour, W., D. M. Mitchell, and L. J. Gray, 2013: A practical method to identify displaced and split stratospheric polar vortex events. *Geophys. Res. Lett.,* **40,** 5268–5273, doi:10.1002/grl.50927.

Sigmond, M., J. F. Scinocca, V. V. Kharin, and T. G. Shepherd, 2013: Enhanced seasonal forecast skill following stratospheric sudden warmings. *Nat. Geosci.,* **6,** 98–102, doi:10.1038/ngeo1698.

Taguchi, M., and D. L. Hartmann, 2005: Interference of extratropical surface climate anomalies induced by El Niño and stratospheric sudden warmings. *Geophys. Res. Lett.,* **32,** L04709, doi:10.1029/2004GL022004.

Thompson, D. W. J., M. P. Baldwin, and J. M. Wallace, 2002: Stratospheric connection to Northern Hemisphere wintertime weather: Implications for prediction. *J. Climate,* **15,** 1421–1428, doi:10.1175/1520-0442(2002)015<1421:SCTNHW>2.0.CO;2.

Tripathi, O. P., and Coauthors, 2015: The predictability of the extratropical stratosphere on monthly time-scales and its impact on the skill of tropospheric forecasts. *Quart. J. Roy. Meteor. Soc.,* **141,** 987–1003, doi:10.1002/qj.2432.

Uppala, S. M., and Coauthors, 2005: The ERA-40 Re-Analysis. *Quart. J. Roy. Meteor. Soc.,* **131,** 2961–3012, doi:10.1256/qj.04.176.

Waugh, D. W., and W. J. Randel, 1999: Climatology of Arctic and Antarctic polar vortices using elliptical diagnostics. *J. Atmos. Sci.,* **56,** 1594–1613, doi:10.1175/1520-0469(1999)056<1594:COAAAP>2.0.CO;2.

Wilks, D. S., 2011: *Statistical Methods in the Atmospheric Sciences.* 3rd ed. International Geophysics Series, Vol. 100, Academic Press, 676 pp.

WMO/IQSY, 1964: International Years of the Quiet Sun (IQSY) 1964–1965: Alert messages with special references to stratwarms. WMO/IQSY Rep. 6, Secretariat of the World Meteorological Organization, 258 pp.

Yoden, S., T. Yamaga, S. Pawson, and U. Langematz, 1999: A composite analysis of the stratospheric sudden warmings simulated in a perpetual January integration of the Berlin TSM GCM. *J. Meteor. Soc. Japan,* **77,** 431–445.

SUPPLEMENTARY MATERIAL

Table S1: SSW onset dates according to the different methods. Dates in bold indicate final warmings (those events where the ZMZW becomes easterly but does not return to westerly for at least 10 consecutive days before 30 April, as in Charlton and Polvani (2007)). SSWs listed in the same row indicate the same event and are denoted as common events (See the main text for details).

U&T	EOFz	EOFu	Tanom	Urate	Trate	U60	MOM
12 Feb 1958	30 Jan1958	27 Jan 1958	8 Feb 1958	27 Jan 1958	5 Feb 1958	31 Jan 1958	-
-	29 Nov 1958	26 Nov 1958	-	-	**-**	-	-
-	**22 Mar 1959**	-	-	-	**13 Mar 1959**	-	-
17 Jan 1960	5 Jan 1960	30 Dec 1959	5 Jan 1960	4 Jan 1960	1 Jan 1960	17 Jan 1960	-
-	-	-	-	-	**26 Mar 1960**	-	-
-	16 Dec 1960	-	-	-	8 Dec 1960	-	-
-	-	**20 Mar 1961**	**-**	28 Feb 1961	**4 Mar 1961**	-	**9 Mar 1961**
-	-	-	20 Feb 1962	-	-	-	30 Jan 1962
-	-	-	-	-	-	-	**7 Mar 1962**
28 Jan 1963	28 Jan 1963	6 Feb 1963	-	24 Jan 1963	21 Jan 1963	28 Jan 1963	-
-	**23 Mar 1964**	**22 Mar 1964**	-	-	28 Feb 1964	**-**	**15 Mar 1964**
-	-	-	-	5 Jan 1965	-	-	-
-	16 Dec 1965	20 Nov 1965	-	-	-	16 Dec 1965	-
23 Feb 1966	-	19 Feb 1966	-	28 Jan 1966	-	23 Feb 1966	26 Feb 1966
7 Jan 1968	31 Dec 1967	5 Jan 1968	2 Jan 1968	1 Jan 1968	27 Dec 1967	7 Jan 1968	29 Dec 1967
-	-	22 Nov 1968	-	-	-	28 Nov 1968	-
-	-	-	-	-	**10 Mar 1969**	13 Mar 1969	-
26 Jan 1970	1 Jan 1970	18 Dec 1970	-	29 Dec 1969	28 Dec 1969	2 Jan 1970	5 Jan 1970
18 Jan 1971	13 Jan 1971	15 Jan 1971	-	11 Jan 1971	7 Jan 1971	18 Jan 1971	15 Jan 1971
21 Mar 1971	-	7 Mar 1971	-	-	-	20 Mar 1971	-
-	-	-	-	21 Feb 1972	20 Feb 1972	-	4 Feb 1972
31 Jan 1973	31 Jan 1973	21 Feb 1973	29 Jan 1973	28 Jan 1973	26 Jan 1973	31 Jan 1973	-
-	-	**20 Mar 1974**	-	20 Feb 1974	23 Feb 1974	-	**12 Mar 1974**
-	-	-	10 Jan 1975	1 Jan 1975	28 Dec 1974	-	**-**
-	-	**18 Mar 1975**	-	26 Feb 1975	**-**	-	**16 Mar 1975**
-	-	-	-	-	**27 Mar 1976**	-	**31 Mar 1976**
9 Jan 1977	25 Dec 1976	19 Dec 1976	21 Dec 1976	19 Dec 1976	17 Dec 1976	9 Jan 1977	7 Jan 1977
-	-	-	-	-	7 Mar 1977	-	-
-	-	-	31 Jan 1978	-	27 Jan 1978	-	-
-	-	**28 Mar 1978**	-	-	**-**	-	**25 Mar 1978**
-	-	4 Dec 1978	-	21 Jan 1979	-	-	-
22 Feb 1979	23 Feb 1979	-	7 Feb 1979	21 Feb 1979	3 Feb 1979	22 Feb 1979	18 Feb 1979
17 Mar 1980	29 Feb 1980	-	28 Feb 1980	23 Jan 1980	25 Feb 1980	1 Mar 1980	-
-	-	-	31 Jan 1981	24 Jan 1981	1 Feb 1981	-	-
-	-	1 Mar 1981	-	-	-	4 Mar 1981	-
4 Dec 1981	-	-	-	1 Dec 1981	-	4 Dec 1981	-
-	-	-	27 Jan 1982	21 Jan 1982	21 Jan 1982	-	-
-	-	-	**-**	**-**	**31 Mar 1982**	-	-
-	-	-	28 Jan 1983	24 Jan 1983	20 Feb 1983	-	-
-	-	18 Mar 1983	-	-	-	-	-
1 Mar 1984	25 Feb 1984	10 Mar 1984	-	12 Jan 1984	17 Feb 1984	24 Feb 1984	25 Feb 1984

|							
1 Jan 1985	30 Dec 1984	26 Dec 1984	31 Dec 1984	28 Dec 1984	26 Dec 1984	1 Jan 1985	25 Dec 1984
-	-	-	-	14 Feb 1986	13 Feb 1986	-	7 Jan 1986
-	-	-	-	-	-	-	**21 Mar 1986**
24 Jan 1987	23 Jan 1987	21 Jan 1987	18 Jan 1987	20 Jan 1987	19 Jan 1987	23 Jan 1987	20 Jan 1987
8 Dec 1987	6 Dec 1987	1 Dec 1987	-	2 Dec 1987	18 Nov 1987	8 Dec 1987	10 Dec 1987
14 Mar 1988	-	-	-	20 Feb 1988	7 Mar 1988	14 Mar 1988	-
21 Feb 1989	19 Feb 1989	12 Mar 1989	12 Feb 1989	24 Jan 1989	8 Feb 1989	21 Feb 1989	-
-	-	-	9 Feb 1990	7 Feb 1990	4 Feb 1990	-	-
-	-	5 Feb 1991	28 Jan 1991	11 Dec 1990	17 Jan 1991	-	-
-	-	-	18 Jan 1992	11 Jan 1992	8 Jan 1992	-	-
-	-	-	-	-	-	-	**22 Mar 1992**
-	-	-	-	11 Feb 1993	-	-	-
-	2 Jan 1994	30 Dec 1993	30 Dec 1993	29 Dec 1993	27 Dec 1993	-	-
-	-	-	-	-	24 Mar 1994	-	-
-	-	-	29 Jan 1995	19 Jan 1995	24 Jan 1995	-	2 Feb 1995
-	-	-	-	-	**20 Mar 1995**	-	-
-	-	-	-	13 Feb 1996	14 Feb 1996	-	-
-	-	17 Nov 1996	-	12 Jan 1997	-	-	-
-	-	26 Dec 1997	26 Dec 1997	3 Dec 1997	17 Dec 1997	-	-
-	6 Jan 1998	-	-	-	30 Jan 1998	-	-
-	-	**30 Mar 1998**	-	-	-	-	-
15 Dec 1998	14 Dec 1998	12 Dec 1998	-	14 Dec 1998	11 Dec 1998	15 Dec 1998	15 Dec 1998
26 Feb 1999	27 Feb 1999	27 Feb 1999	26 Feb 1999	23 Feb 1999	19 Feb 1999	26 Feb 1999	24 Feb 1999
20 Mar 2000	-	-	-	-	10 Mar 2000	20 Mar 2000	-
-	-	18 Nov 2000	20 Dec 2000	-	7 Dec 2000	-	-
11 Feb 2001	13 Feb 2001	4 Feb 2001	-	31 Jan 2001	25 Jan 2001	11 Feb 2001	15 Mar 2001
31 Dec 2001	25 Dec 2001	29 Dec 2001	27 Dec 2001	23 Dec 2001	19 Dec 2001	31 Dec 2001	-
18 Feb 2002	-	-	-	12 Feb 2002	11 Feb 2002	18 Feb 2002	21 Mar 2002
18 Jan 2003	18 Jan 2003	-	31 Dec 2002	14 Jan 2003	26 Dec 2002	18 Jan 2003	17 Jan 2003
-	-	-	-	-	28 Mar 2003	-	-
-	3 Jan 2004	30 Dec 2003	20 Dec 2003	16 Dec 2003	15 Dec 2003	5 Jan 2004	2 Jan 2004
-	-	-	-	-	-	-	-
-	-	**15 Mar 2005**	-	26 Jan 2005	20 Feb 2005	-	**11 Mar 2005**
21 Jan 2006	21 Jan 2006	10Jan 2006	12 Jan 2006	21 Jan 2006	9 Jan 2006	21 Jan 2006	17 Jan 2006
-	-	-	-	-	31 Dec 2006	-	-
24 Feb 2007	-	-	-	21 Feb 2007	20 Feb 2007	24 Feb 2007	-
-	-	-	25 Jan 2008	22 Jan 2008	20 Jan 2008	-	-
22 Feb 2008	24 Feb 2008	-	-	-	-	22 Feb 2008	18 Feb 2008
25 Jan 2009	23 Jan 2009	25 Jan 2009	-	22 Jan 2009	17 Jan 2009	25 Jan 2009	18 Jan 2009
-	-	21 Nov 2009	-	-	-	-	-
-	-	26 Jan 2010	-	22 Jan 2010	18 Jan 2010	9 Feb 2010	-
-	-	22 Mar 2010	-	-	-	24 Mar 2010	-
-	-	-	-	-	28 Jan 2011	-	-
-	-	9 Feb 2012	18 Jan 2012	11 Jan 2012	12 Jan 2012	-	7 Mar 2012
-	-	-	-	1 Dec 2012	-	-	-
-	6 Jan 2013	23 Dec 2012	6 Jan 2013	5 Jan 2013	1 Jan 2013	6 Jan 2013	-
-	-	-	-	-	13 Mar 2014	-	-
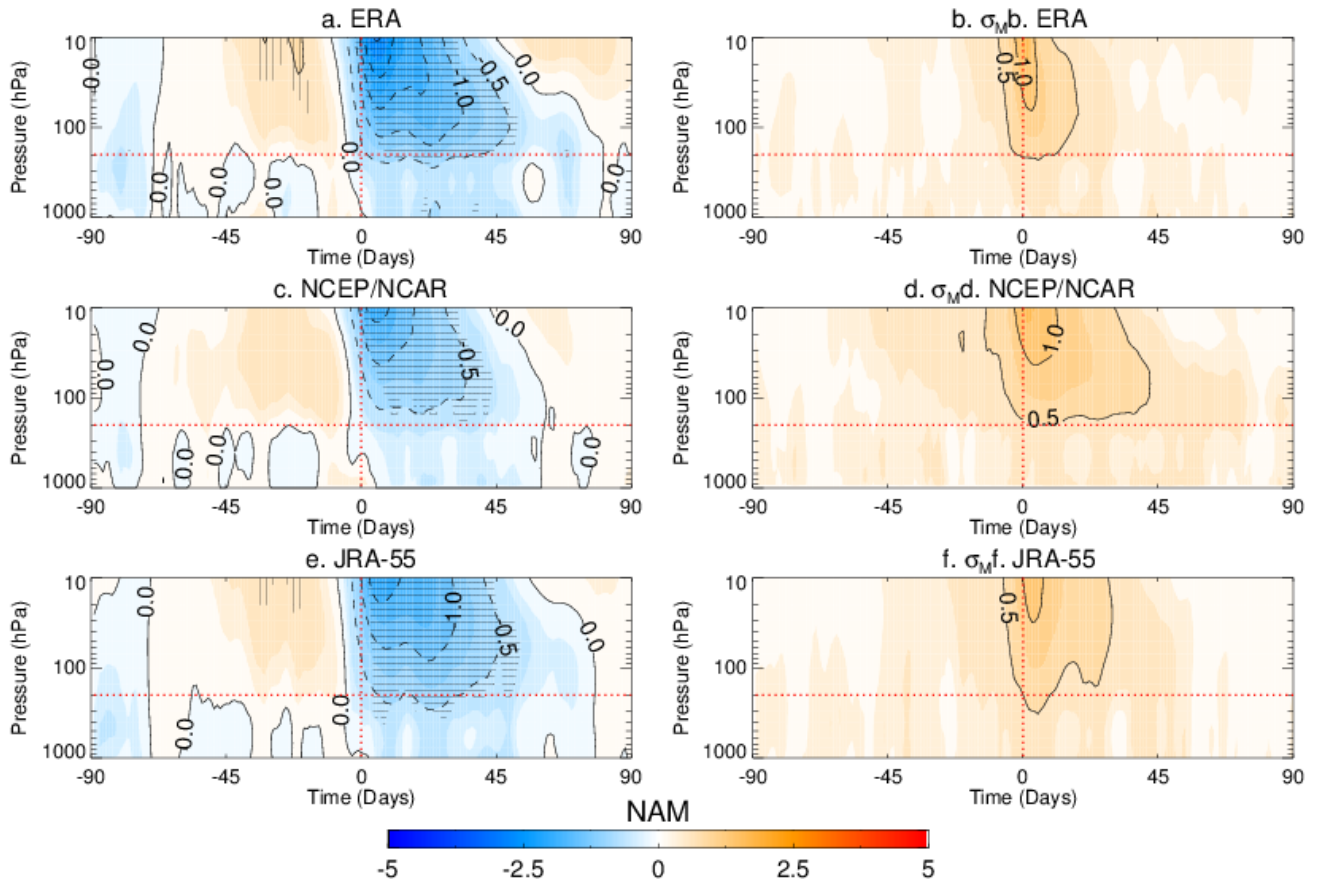
FIG. S1. Left: Multi-method means (MMM) of the time-height NAM index composites (in standard deviation units) for the: (a) ERA; (c) NCEP/NCAR; and (e) JRA-55 reanalysis from 1958 to 2014. Right: Inter-method standard deviation (σ_M) of the time-height NAM composites for the: (b) ERA; (d) NCEP/NCAR; and (f) JRA-55 reanalysis. The abscissa denotes days relative to the SSW onset date. The red horizontal line indicates the 200 hPa pressure level (i.e., approximately the extratropical tropopause). Hatched areas indicate regions where more of 75% of the methods agree in the sign and significance of the NAM signal. MOM definition is not included in the composites.
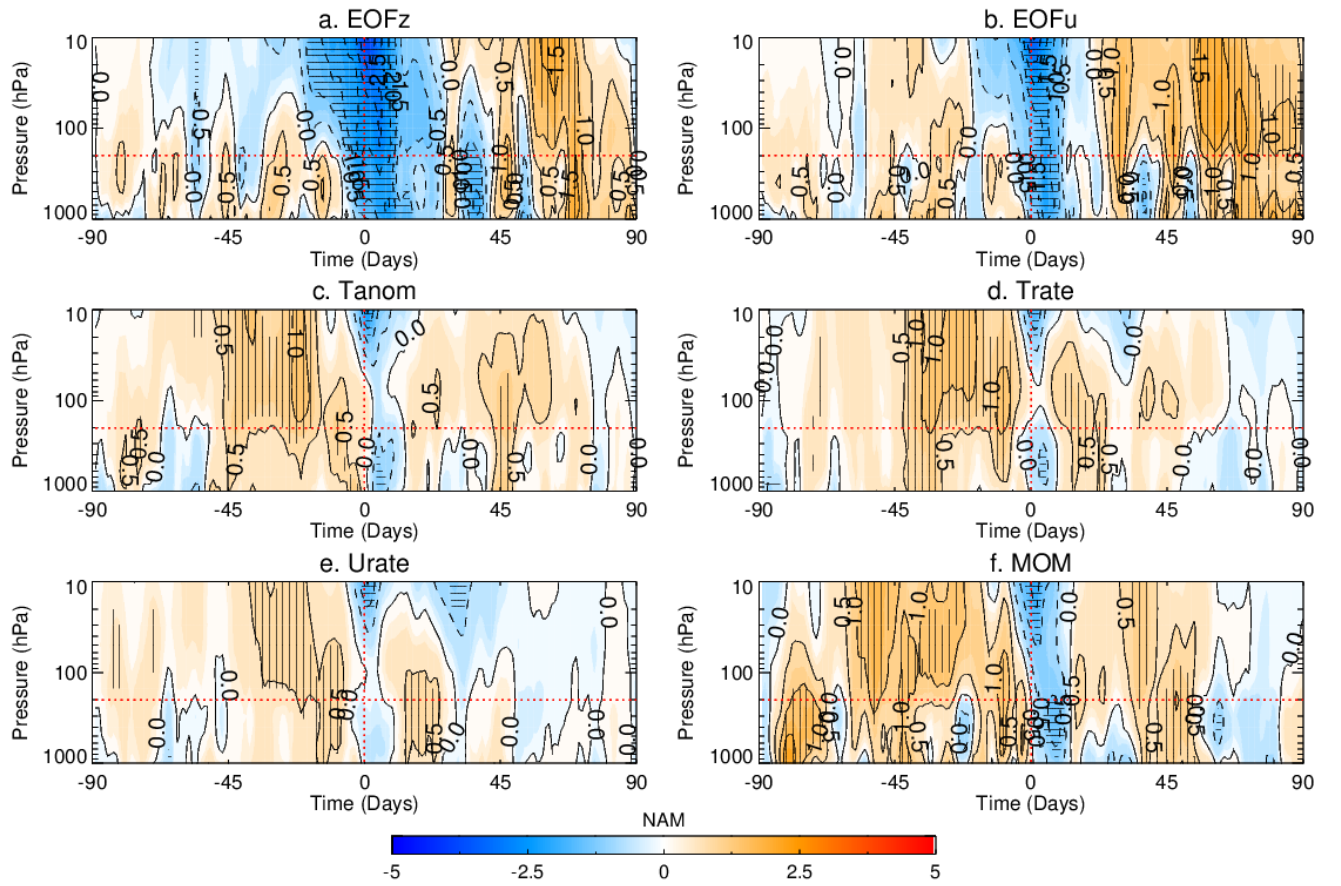
FIG. S2. Same as Fig. 6 but for minor SSWs only. Note that U&T and U60 are not included herein. Results are shown for the readjusted onset dates (See the main text for details).
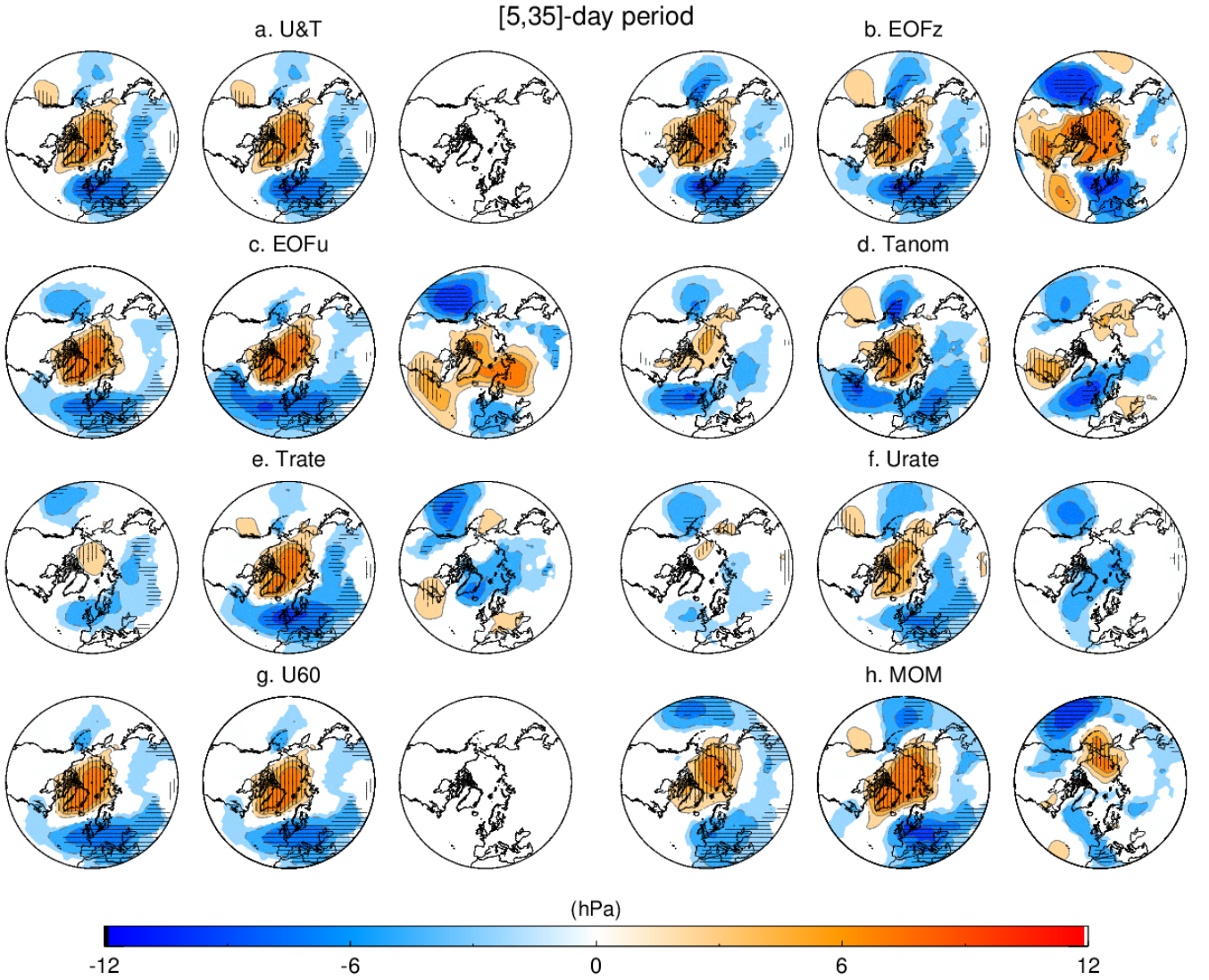
FIG. S3. SSW-based composites of the mean sea-level pressure (MSLP) anomalies (in hPa) in the [5,35]-day period after events for: (a) U&T; (b) EOFz; (c) EOFu; (d) Tanom; (e) Urate; (f) Trate; (g) U60; and (h) MOM. The three panels of each method show the corresponding composites for: (left) all; (middle) major and; (right) minor SSWs. Horizontal (vertical) hatched areas indicate negative (positive) anomalies that are statistically significant at the 95% confidence level according to a 1000-trial Monte Carlo test. Results are shown for the readjusted onset days (See the main text for details). Note that U&T and U60 do not include minor SSWs.
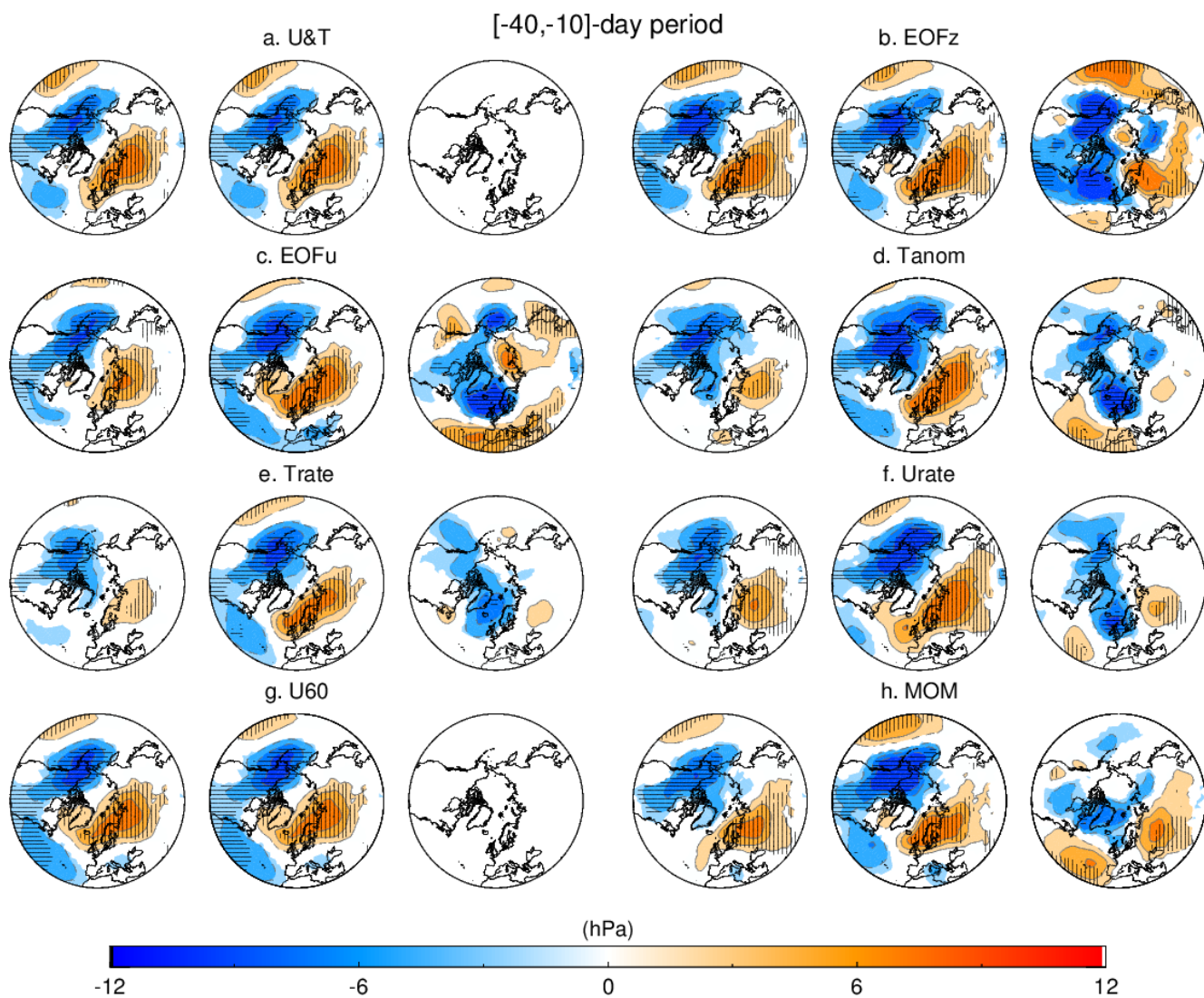
FIG. S4. Same as Fig. S3 but for the [-40,-10]-day period prior to events.
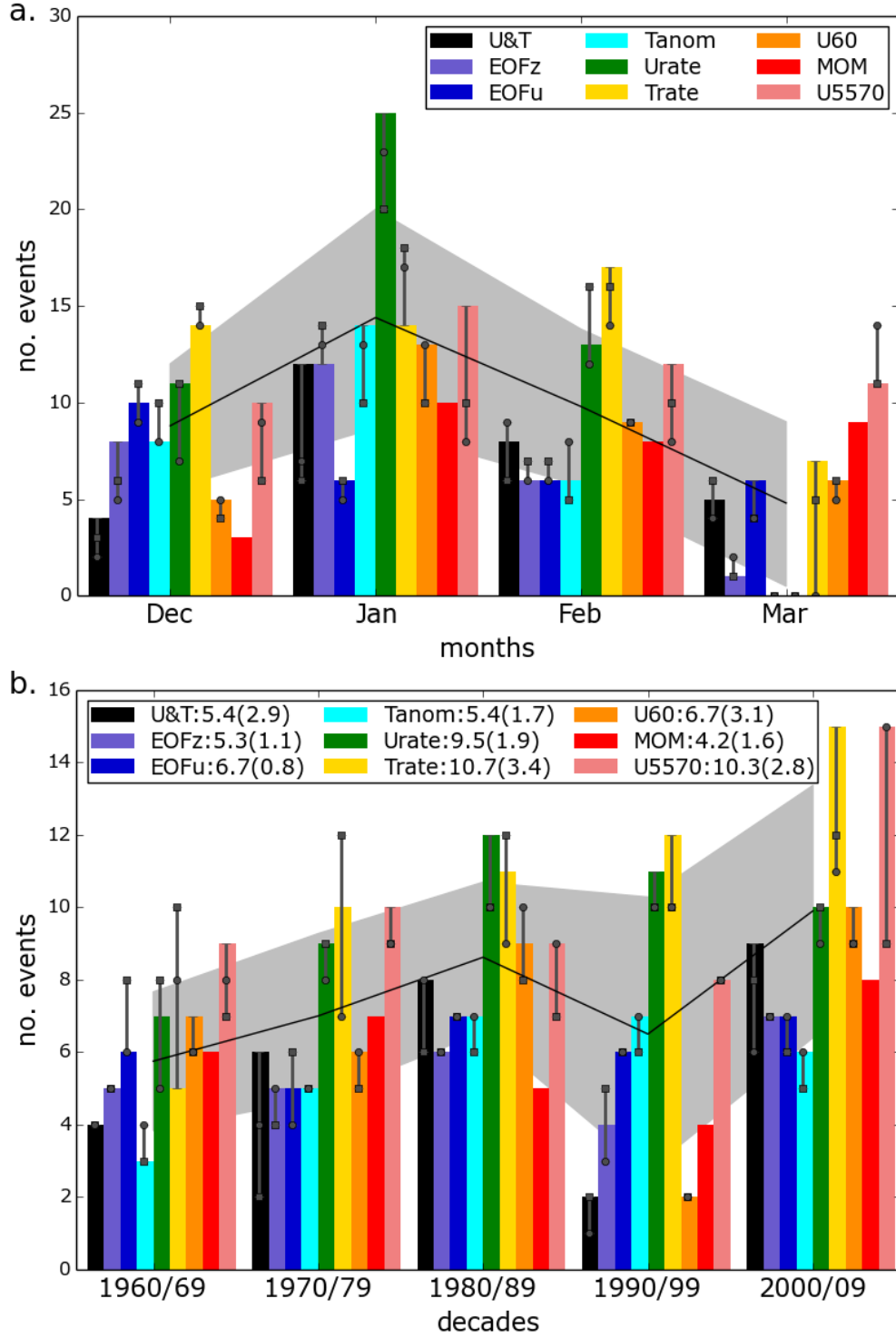
FIG. S5. (a) As Fig. 2 and (b) as in Fig. 3 but adding the U5570 method (See the main text for details).

Chapter 4

On how turbulent mountain stress influences the sudden stratospheric warming frequency in WACCM

On How Turbulent Mountain Stress Influences the Sudden Stratospheric Warming Frequency in WACCM

Froila M. Palmeiro[1], Rolando R. García[2], Natalia Calvo[1], and David Barriopedro[1]

[1]Departamento de Física de la Tierra II, Universidad Complutense de Madrid, Madrid, Spain
[2]Atmospheric Chemistry Division, NCAR, Boulder, Colorado

Abstract

The implementation of the Turbulent Mountain Stress (TMS) parametrization in the Whole Atmospheric Community Climate Model is found to be critical to obtain a realistic Sudden Stratospheric Warming (SSW) frequency in the Northern Hemisphere. The comparison of two 50-year runs, one with TMS (TMS-on) and one without (TMS-off) reveals lower than observed SSW frequency in TMS-off from December to February, while in March both simulations show SSW frequencies comparable to reanalysis. Meridional eddy heat fluxes in the lower stratosphere are stronger in TMS-on than in TMS-off, except in March. These differences are accompanied by increased orographic gravity wave drag (OGWD) in TMS-off that comes mainly from the Himalayas and the Rocky Mountains in response to stronger surface winds. Two different mechanisms of how planetary and GWs interact are identified in the simulations. In the lower stratosphere, enhanced dissipation of GWs in TMS-off modifies the subtropical jet and thus the conditions for refraction of planetary waves, which then propagate preferentially towards the equator instead of towards the pole. In the middle and upper stratosphere, compensation between resolved and parametrized GWs leads to weaker Eliassen-Palm flux divergence (EPFD) in response to stronger OGWD in TMS-off. While the former mechanism persists for the entire winter, the OGWD in TMS-off decreases in March and is compensated by enhanced EPFD, which might explain the reduced TMS-off bias in the frequency of March SSWs.

1 Introduction

Sudden Stratospheric Warmings (SSWs) are the most extreme dynamical events in the northern winter stratosphere, with an evident imprint on stratospheric variability and climatology (e.g., Limpasuvan et al. 2004, Gómez-Escolar et al. 2012). There are at least two important reasons to reproduce accurate frequencies of SSWs in General Circulation Models (GCMs). First, to obtain a realistic stratospheric winter variability, and second, because SSWs can impact the tropospheric flow during several weeks after the event, making them a potentially powerful tool for improving weather forecasts (e.g., Baldwin and Dunkerton 2001; Sigmond et al. 2013).

Within the fifth Coupled Model Intercomparison Project (CMIP5), Charlton-Pérez et al. (2013) showed discrepancies among GCMs in re-producing SSW frequencies (see their Table 1). In particular, low-top models, defined as those with an upper boundary below 1 hPa, were the largest outliers in reproducing SSW frequencies and also stratospheric variability. Later on, Shaw et al. (2014) found that a low model top is not enough to explain the under-representation of the winter stratospheric variability in GCMs since several high-top models still exhibit certain biases in reproducing extreme stratospheric events. Using idealized models, Scott et al. (2004) demonstrated that stratospheric winter variability is strongly sensitive to the horizontal resolution of GCMs, in agreement with previous studies regarding SSW predictability (e.g., Mechoso et al. 1985; Coy et al. 2009). In particular, Charlton-Pérez et al. (2013) showed that the same high-top model simulated an improved SSW frequency by simply increasing its horizontal resolution, so that orography is better represented which

is important to resolve planetary wave (PW) structures and its propagation and dissipation.

Early studies on SSW precursors considered the upward propagation of PWs and their interaction with the zonal mean flow as the main dynamical mechanism for the occurrence of SSWs (e.g., Matsuno 1971). The inter-hemispheric asymmetry in the PW forcing explains the differences in the SSW frequency between hemispheres. While SSWs are commonly observed in the Northern Hemisphere (NH), usually more than once every two years (Charlton and Polvani 2007), only one event has ever been observed in the Southern Hemisphere (Krüger et al. 2005). This has been attributed to the preponderance of topography in the NH, which favors the generation of upward-propagating PWs that can disrupt the polar vortex (e.g., Wexler 1959).

In addition to PWs, which are resolved in GCMs, the other main forcing of the lower stratospheric circulation comes from the dissipation of orographic gravity waves (OGWs). Due to the small scale of these waves, their effect has to be parametrized in the models as OGW drag (OGWD). OGWD weakens the subtropical jet in the lower stratosphere, can alter the refractive conditions for PWs (Sigmond and Scinocca 2010) and hence, modify the stratospheric climatological flow and its variability (Siskind et al. 2007). Another paradigm of how PWs interact with OGW was first considered in McLandress and McFarlane (1993). Their experiments suggested different responses in the Eliassen-Palm flux divergence (EPFD) depending on the location of the applied OGWD. This idea was further explored in Cohen et al. (2013) and refined in Cohen et al. (2014), who proposed a compensation mechanism to understand the role of different waves in driving the Brewer-Dobson circulation. This compensation occurs in the stratospheric 'surf zone' when GWs perturb the potential vorticity structure and PWs respond to counteract the GWs effects and maintain the original conditions. Consideration of this effect was found to be key for interpreting the role of different waves in the Brewer-Dobson circulation changes simulated under a changing climate (Sigmond and Shepherd 2014).

Thus, a correct representation of OGW forcing is arguably essential for GCMs to obtain realistic stratospheric winter variability. In the case of the Whole Atmospheric Community Climate Model (WACCM), Richter et al. (2010) demonstrated that adding a turbulent mountain stress (TMS) parametrization increased the winter frequency of SSWs and made it comparable to reanalysis data. They proposed that the surface roughness prescribed by the TMS parametrization leads to weaker surface winds, which, in turn, imply weaker OGWD in the lower stratosphere and a stronger subtropical jet. The associated changes in the index of refraction result in stronger PW flux towards the Pole, eventually disrupting the polar vortex and leading to more SSWs.

Here, we examine in detail the effect of the TMS parametrization in the intra-seasonal variations of the stratospheric circulation, which were not addressed by Richter et al (2010). To understand the differences between simulations, we assess the hypothesis of Richter et al. (2010) and the compensation mechanism between OGWs and PWs. Since both processes are predicated on changes in OGWD inducing changes in PWs, this approach might be useful to better understand the stratospheric biases in other GCMs.

2   Data and Methods

We compare two 50-year historical (1955-2005) simulations with the atmosphere-ocean coupled WACCM4 (Marsh et al. 2013) instead of the purely atmospheric version (WACCM3.5) used in Richter et al. (2010). We have used daily-mean and monthly-mean model output with 2.5° x 1.9° horizontal resolution. There are 66 levels distributed every 1.5 km up to 25 km, then every 2 km up to the stratopause, every 3.5 km throughout the mesosphere, and at half of the local scale height from the mesopause to the upper boundary of the model at about 140 km. The study focuses on the seasonal evolution throughout the extended winter, defined as November through March. Where appropriate, we also compare the simulation results to daily-mean and monthly-mean data from the 1955-2005 period of the NCEP-NCAR reanalysis (Kalnay et al. 1996), with 2.5° x 2.5° horizontal resolution.
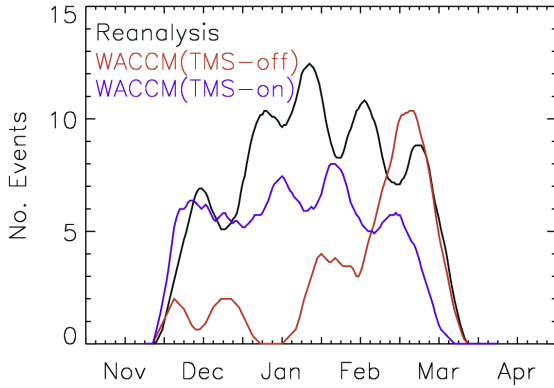
Figure 1: SSW total frequency distribution within ±10-days of the date in the x-axis for 1955 to 2005 derived from NCEP-NCAR reanalysis (black), TMS-on (red) and TMS-off (blue). The frequencies are smoothed with a 10-day running mean.

To elucidate the mechanisms whereby TMS leads to realistic SSW frequencies, we compare two different simulations, one that includes the TMS parametrization (TMS-on) and one that does not (TMS-off). In WACCM, this TMS parametrization consists in a surface stress that is proportional to the horizontal wind vector V at the surface, as follows:

$$\tau = \rho C_d \left|\mathbf{V}\right| \mathbf{V} \qquad (1)$$

where ρ is the air density and C_d is a drag coefficient, which depends on the standard deviation of the topography that is not resolved by the model horizontal grid. For a more detailed description of the drag coefficient in Eq. (1) see Richter et al. (2010). The OGWD parameterization in WACCM is based on McFarlane (1987) and the amplitude of the parametrized GWs is proportional to the surface mean flow times the height of the local topography. This means that stronger surface wind over regions of steep orography will produce more OGWD at upper levels.

SSWs are identified from November to March, as in Palmeiro et al. (2015), evaluating the zonal-mean zonal wind reversal from westerlies to easterlies at 10 hPa over a range of latitude, 55-70ºN. The methodology adopted herein ensures that the polar vortex edge is included in the evaluation of the zonal-mean wind so that possible biases in the location of the polar vortex are not affecting the counting of SSWs (Butler et

al. 2015). Consecutive SSWs can be detected if there are at least 20 days of westerlies between them, and those events for which the zonal-mean wind does not return to westerly for at least 10 days before the 30 of April are considered final warmings and are discarded.

To assess the discrepancies in SSW frequency between simulations, we have computed on a daily basis the [45-75ºN] area-weighted meridional eddy heat flux $[v'T']$ at 100 hPa, an indicator of the upward PW propagation into the stratosphere (Andrews and McIntyre, 1976). Following Nishii et al. (2009), the meridional eddy heat flux anomalies can be decomposed as follows:

$$[v'T']_a = [v'_a T'_c] + [v'_c T'_a] + [v'_a T'_a]_a \qquad (2)$$

where v is the meridional wind, T the temperature, primes denote departures from the zonal mean, represented by brackets, and the subscripts c and a indicate the climatological annual cycle and the daily deviation therefrom, respectively. The first two terms on the right-hand side of Eq. (2) represent the interaction between the climatological and the anomaly fields, and they will be referred together as the interference term. The last term of Eq. (2) may be interpreted as the high-frequency PW interactions (also referred to as the instantaneous wave anomaly term).

Additional diagnostics have been used to examine the differences between simulations on monthly-mean time-scales. To characterize the regions where PWs propagate and dissipate, the Eliassen-Palm flux and its divergence (EPFD) (Andrews and McIntyre 1976) have been computed from monthly-mean data, so that only the contribution of stationary waves is considered. The refractive index (Matsuno, 1970) is also computed to illustrate the origin of the differences in PW propagation between simulations. This index has been calculated based on monthly-mean data following Eq. (12) of Matsuno (1970). This diagnostic uses the quasi-geostrophic approximation, which has been considered appropriate to study the dynamics of PWs and SSWs (Matsuno 1971 and Palmer 1981a,b among others). Contribution to the momentum budget from OGWs is quantified by the OGWD. To evaluate the compensation mechanism between PWs and GWs proposed in Cohen et al. (2013), we examine the zonal-mean
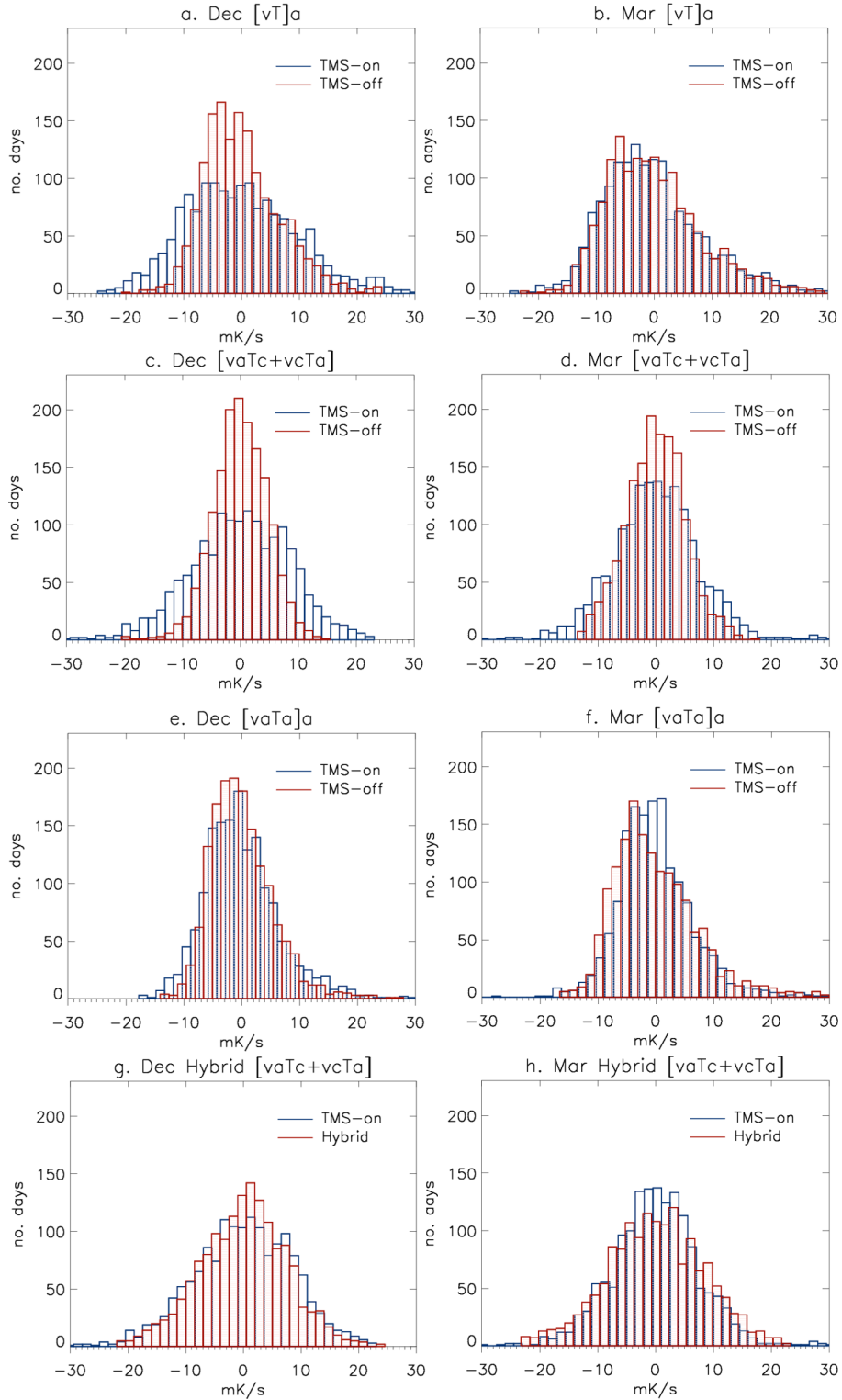
Figure 2: Climatological (1955-2005) mean PDF of the daily [45-75°N] meridional eddy heat flux anomalies at 100 hPa ($m\ K\ s^{-1}$) in (left panels) December and (right panels) March for: (a,b) total eddy heat flux anomalies; (c,d) interference term; (e,f) anomalous term; (g,h) interference term for TMS-on and the hybrid simulation (see text for details). TMS-on (TMS-off) PDF are shown in blue (red). Note that panels (a-f) correspond to each term of Eq. (2).

bounded by given latitudes and levels:

torque due to wave forcing in an atmospheric torus

$$\overline{T} = \int_{z_1}^{z_2} \int_{\theta_1}^{\theta_2} 2\pi a^2 \rho cos^2\theta \left(\frac{1}{\rho a cos\theta} \boldsymbol{\nabla} \cdot \mathbf{F} + \frac{1}{\rho} \frac{\partial}{\partial z} (\overline{\rho u'w'}) \right) a d\theta dz \tag{3}$$

where:

$$\boldsymbol{\nabla} \cdot \mathbf{F} = \frac{1}{a cos\theta} \frac{\partial}{\partial \theta} (F_y cos\theta) + \frac{\partial (F_z)}{\partial z} \tag{4}$$

is the EPFD, $F = (F_y, F_z)$ (Andrews et al., 1987); $\overline{\rho u'w'}$ is the vertical eddy momentum flux of (parameterized) GWs; a is the Earth's radius; ρ is the log-pressure density; θ is latitude and z is log-pressure altitude. The integration limits, z_1, z_2 and θ_1, θ_2, are the bottom, top, left and right boundaries of the region evaluated.

Following Cohen et al. (2014), we apply Green's theorem to Eq. (3) and obtain:

$$\overline{T} = \int_{z_1}^{z_2} 2\pi a cos\theta F_y dz|_{\theta_2} - \int_{z_1}^{z_2} 2\pi a cos\theta F_y dz|_{\theta_1} + \int_{\theta_1}^{\theta_2} 2\pi a cos\theta F_z a d\theta|_{z_2} \tag{5}$$

$$- \int_{\theta_1}^{\theta_2} 2\pi a cos\theta F_z a d\theta|_{z_1} + \int_{\theta_1}^{\theta_2} 2\pi a cos\theta F_{gw} a d\theta|_{z_2} - \int_{\theta_1}^{\theta_2} 2\pi a cos\theta F_{gw} a d\theta|_{z_1}$$

where F_{gw} is a flux of gravity wave activity, defined as:

$$F_{gw} = \rho a cos\theta \cdot \overline{u'w'} \tag{6}$$

such that is has the same units ($N\ m^{-1}$, or $kg\ s^{-2}$) as F_y and F_z.

In our analysis, we perform a systematic comparison between TMS-on and TMS-off throughout the extended winter. However, for simplicity, we will only show the results for the beginning (December) and the end (March) of the winter, since they are the months with the largest and smallest differences between simulations. Similar conclusions are obtained comparing early and late winter (e.g., November and December versus February and March). Significant differences are assessed with a two-tailed Student's t-test at the 95% confidence level.

3 Results

The frequency of occurrence of major SSWs is 5.5 events per decade in the TMS-off simulation and 8.2 events per decade in TMS-on, which is closer to the 10.3 events per decade found for the NCEP-NCAR reanalysis. If only early and mid-winter (November to February) SSWs are considered, this difference increases from 2.2 events per decade in TMS-off to 6.8 in TMS-on. The monthly distribution of events (Figure 1) is also very different between simulations. While TMS-on shows a rather homogeneous occurrence of SSWs throughout the entire winter, similar to the behavior observed in the reanalysis, most events in TMS-off occur in late winter, with the largest occurrence in March. Note that none of the events in Fig. 1 are final warmings, which are excluded by the detection criteria. The above results are robust if other methods of detecting SSW are used (e.g., WMO or Charlton and Polvani, 2007). The differences in the intra-seasonal distribution of events suggest that the mechanisms that produce SSWs operate differently in early and late winter. Consequently, from now on, we will perform the analysis on a monthly basis and compare December and March systematically.

To further understand the intra-seasonal differences between simulations in the SSW frequency, we have compared the distributions of the daily
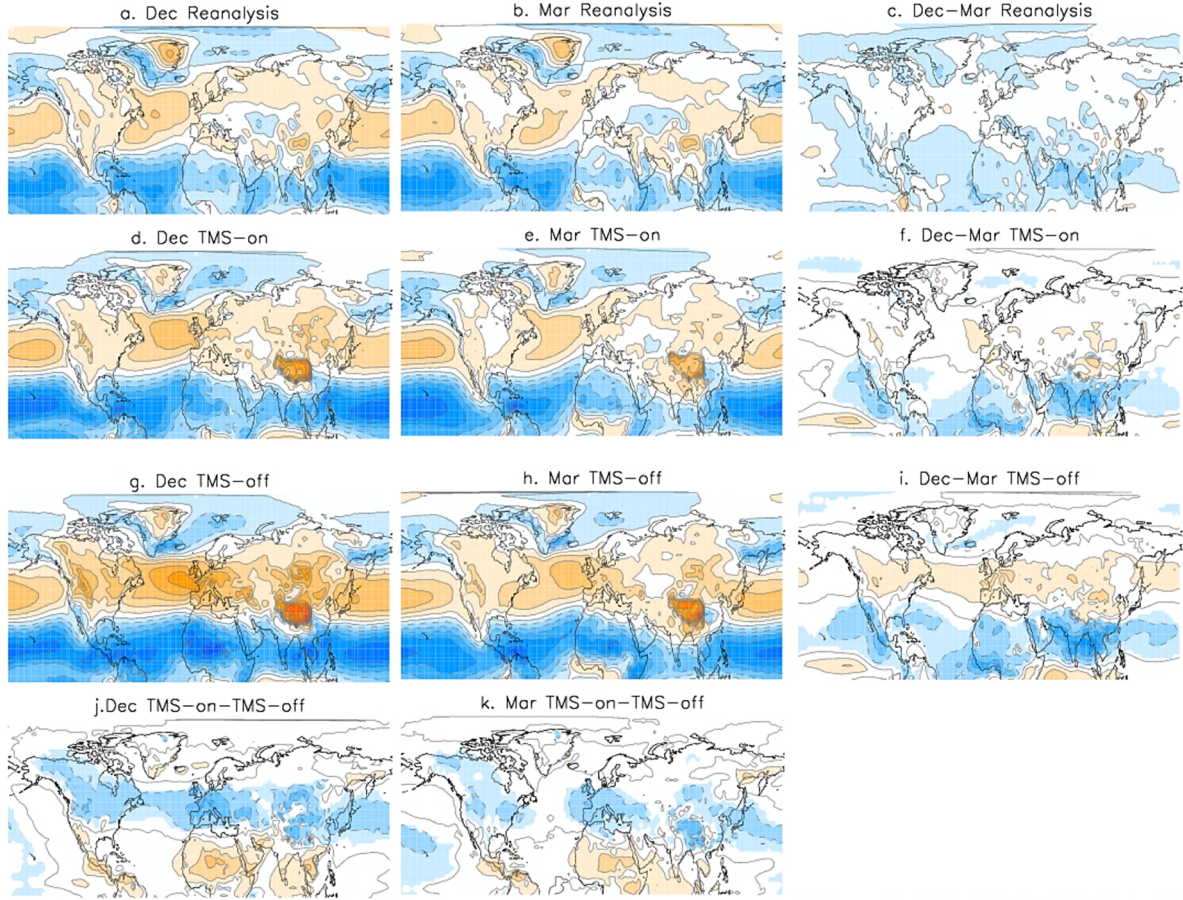
Figure 3: Climatological (1955-2005) mean surface zonal wind ($m\ s^{-1}$) in (left column) December, (middle column) March, and (right column) December minus March for: (a-c) NCEP-NCAR reanalysis; (d-f) TMS-on; (g-i) TMS-off; and (j-k) TMS-on minus TMS-off. Contour intervals are every 2 $m\ s^{-1}$. Only significant differences at the 95% confidence level are shaded.

meridional eddy heat flux anomalies at 100 hPa and their contributing terms (see Eq. (2)) for December and March (Figure 2). Interestingly, the TMS-on simulation (blue lines) has more days with large positive heat flux values (blue lines) than TMS-off (red lines) in December (Fig. 2a) but a similar distribution in March (Fig. 2b), consistent with the corresponding behavior in the SSW frequency distribution (Fig. 1). These differences arise from the interference term of Eq. (2) (Figs. 2c and 2d), which, according to Smith and Kushner (2012), is particularly important before SSW occurrence. Thus, the differences between TMS-on and TMS-off in the interference term are large in December, with stronger constructive interference in TMS-on, and vanish in March. Since the interference includes cross-terms of climatological and anomalous val-

ues, the differences between TMS-on and TMS-off could be attributed to either one or another (or both). To assess this question, we have recalculated the interference term for TMS-off using its own values for the anomalies, Va(off) and Ta(off), but imposing the TMS-on climatological values, Tc(on) and Vc(on), respectively. The resulting distributions for this hybrid interference term (Fig. 2g,h) are comparable to the original interference term distribution of the TMS-on simulation (also included in Fig. 2g,h for convenience). Moreover, we repeated this methodology, but testing the anomalies in TMS-on over the TMS-off climatology, and obtained a similar distribution to the original interference term of TMS-off (not shown). These results demonstrate that the main difference between simulations lays in the climatological amplitude of the PWs

entering the lower stratosphere and not in the amplitude of the daily anomalies. Therefore, in the remaining, we will focus on monthly-mean fields.

The question then is how the climatological configurations are set up in TMS-on and TMS-off. Differences between simulations ultimately originate at the surface, where the TMS parametrization is implemented. Figure 3 depicts the surface wind for December and March in reanalysis and both simulations. We recall that TMS surface drag is, by definition, directly proportional to the surface wind in TMS-on, whereas it is identically zero in TMS-off. Compared to reanalysis, TMS-on reproduces the surface wind more accurately than TMS-off, which tends to overestimate the wind values, particularly in December, due to the lack of surface drag. The most noticeable differences between simulations are found over North America and the North Atlantic Ocean, and in South Asia and the West Pacific Ocean, that is, downstream of the regions of high topography (the Rocky Mountains, and the Himalayas, respectively). Moreover, there are differences between the simulations in the intra-seasonal changes of the surface wind (Fig. 3, right column). While the intra-seasonal variations are small and similar to reanalysis in TMS-on (Fig. 3f), TMS-off shows a marked intra-seasonal cycle in zonal wind, specifically along the belt of westerlies (around 30°N to 55°N, Fig. 3i). As a consequence, the differences between simulations are large in December and diminish in March (cf. Fig. 3j and Fig. 3k).

The stronger surface wind in TMS-off implies stronger OGW forcing, and thus stronger OGWD on the zonal-mean flow at higher levels. To illustrate this, Figure 4 shows the refractive index squared (n^2), with EP flux vectors superimposed for TMS-on, TMS-off and their differences in December and March. As reported by Richter et al. (2010) for the atmosphere-only WACCM3.5, the main difference between simulations is the location of the minimum n^2. According to refractive index theory, waves tend to propagate towards regions of maximum n^2 and away from regions of minimum n^2 values (Matsuno, 1970). In TMS-on (Fig. 4a, b), the minimum values of n^2 are located farther poleward than in TMS-off

(Fig. 4c, d). Consequently, upward propagating PWs from the troposphere tend to be preferably refracted to the Pole in TMS-on, while equatorward propagation is more pronounced in TMS-off. Note that the differences in the refractive index between simulations persist the entire winter, that is, they are present with similar magnitude and spatial distribution in both early (December, Fig. 4e) and late (March, Fig. 4f) winter. On the other hand, the differences in the EP flux field reveal substantial intra-seasonal variability (compare vector differences in Fig. 4e,f). In December, there is stronger upward PW propagation in TMS-on compared to TMS-off, whereas upward PW propagation is similar in March. The largest intra-seasonal changes in EP flux occur for TMS-off, which displays an increased PW activity in the polar stratosphere by late winter. This is consistent with the results for the surface wind (Fig. 3), the heat fluxes (Fig. 2) and the SSW frequencies (Fig. 1). Therefore, changes in the refractive index do not appear to be sufficient to explain differences in PW propagation across the winter.

Next, we compare the wave drag from PWs and from OGWs in the northern winter stratosphere. Figure 5 shows the latitude-height cross sections of EPFD and OGWD for TMS-on and TMS-off in December and March. The zonal-mean wind is also shown in thick black contours, superimposed on the OGWD. In the lower stratosphere, the largest wave forcing is located around the subtropical jet maximum for both PWs and GWs. The reduced OGWD in TMS-on modifies the subtropical jet and this in turn, changes the refractive conditions for PWs shown previously. The differences in OGWD and EPFD between simulations remain similar from December to March in the lower stratosphere, consistent with the behavior of the refractive conditions for PWs (Figs. 4a,b). On the contrary, in the upper stratosphere, differences between simulations in both OGWD and EPFD are much larger in December (Fig. 5i,j) than in March (Fig. 5k,l).

More specifically , in December the OGWD is weaker in TMS-on compared to TMS-off (Figs. 5b,f), while the opposite occurs for the EPFD (Figs. 5a,e). In fact, for this month, the dominant forcing in TMS-on is the EPFD,
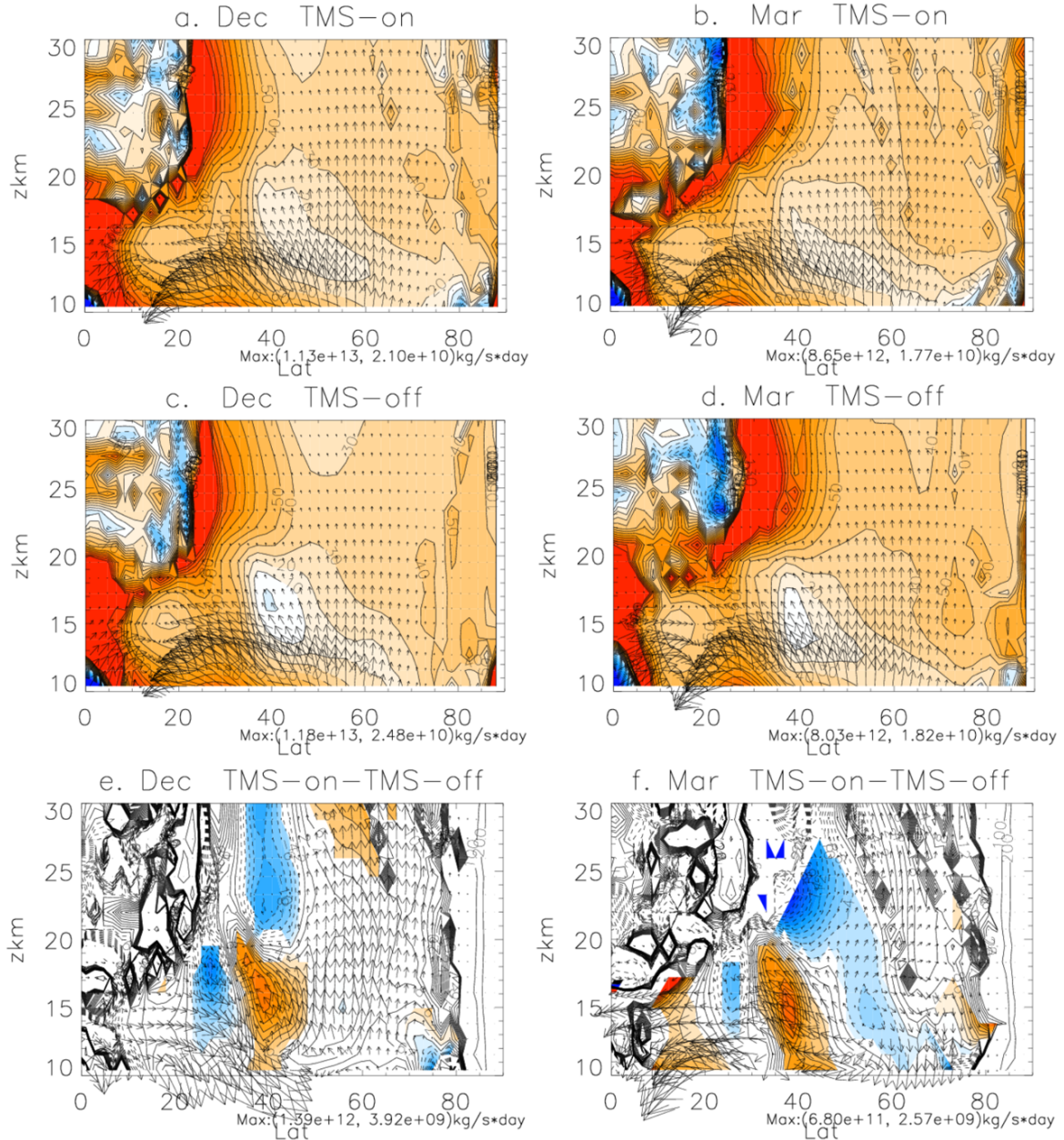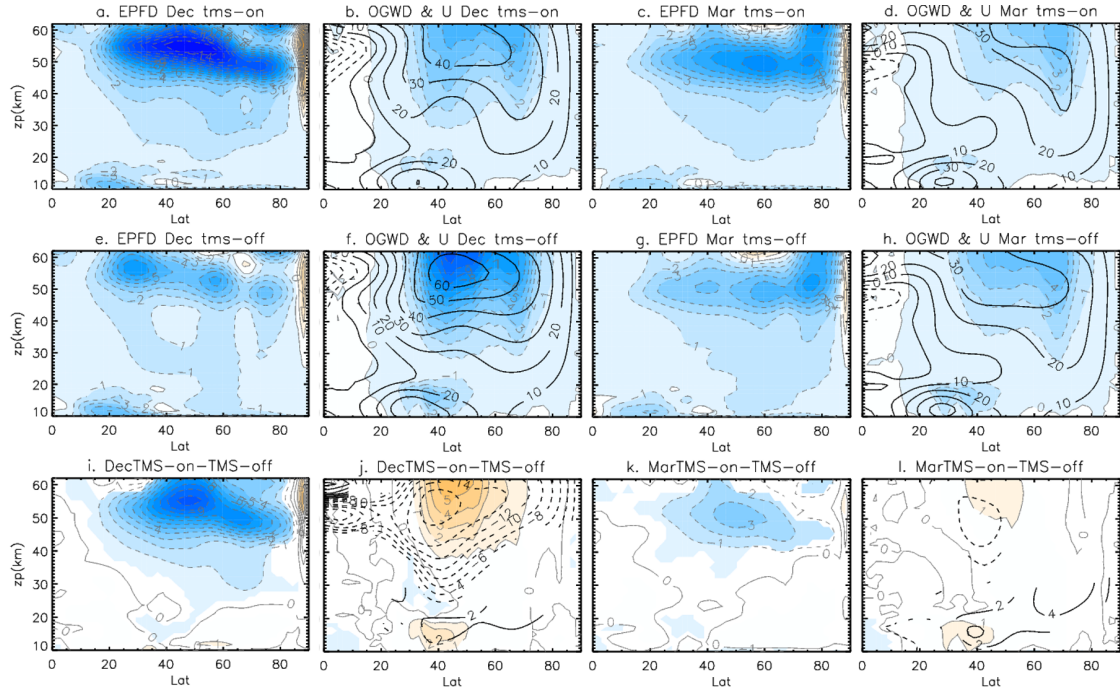
Figure 4: Climatological (1955-2005) mean wave-1 refractive index squared (shading, dimensionless) and EP flux (vectors, $kg\ s^{-1}day^{-1}$) in (left panels) November-December and (right panels) February-March for: (a,b) TMS-on; (d,e) TMS-off; and (c,f) TMS-on minus TMS-off. The refractive index squared has been multiplied by the radius of the earth squared (a^2n^2) so it is dimensionless. Contour interval is 10. Only significant differences at the 95% confidence level are shown. Maximum EP flux values are indicated below each panel.

which is consistent with more frequent SSW occurrence, whereas the leading driver in TMS-off is the OGWD. Therefore, in December, there is apparently a large degree of compensation between resolved EPFD and OGWD, such that the total forcing in the stratosphere remains relatively constant between TMS-on and TMS-off

(cf. Fig. 5i,j). In March both OGWD and EPFD in TMS-off are close to their values in TMS-on, such that the difference between the two simulations is much smaller (cf. Figs. 5k,l) than in December.

To quantify this potential compensation mech-

Figure 5: Climatological (1955-2005) mean (first and third column) EP flux divergence (shading, $m\ s^{-1}\ day^{-1}$) and (second and fourth column) zonal-mean zonal wind tendency due to OGWD (shading, $m\ s^{-1}\ day^{-1}$) in December and March for (top row) TMS-on, (middle row) TMS-off and (bottom row) TMS-on minus TMS-off. For panels showing the zonal-mean zonal wind tendency, black contours denote the zonal-mean zonal wind ($m\ s^{-1}$). Contours are every $1\ m\ s^{-1}\ day^{-1}$ for the wave forcings and every $10\ m\ s^{-1}$ ($2\ m\ s^{-1}$) for the zonal-mean zonal wind climatology (differences). Top row is for TMS-on, middle for TMS-off and bottom for TMS-on minus TMS-off. Only significant differences at the 95% confidence level are shown.

anism along the lines of Cohen et al.'s (2014) analysis, the EP fluxes, the OGW fluxes and the associated divergences were calculated in torque units following Eq. (5). Using the same units allow us to estimate the net torque in a given region simply by adding the torques across its boundaries. Figure 6 shows a schematic of the PWs and OGWs relative contributions to the net torque within the region of larger EPFD and OGWD in Fig.5. The dashed (solid) circled values indicate the contribution of PWs in TMS-on (TMS-off) in red and the same is shown in green for the OGWs. Recall that the main difference between simulations is the enhanced OGWD for TMS-off in December (Fig. 5e), which is accompanied by reduced EPFD in the upper stratosphere (Fig. 5b). The net forcing in the considered region (PWs plus GWs) relative to the incoming upward torque is similar for both TMS-on (78%) and TMS-off (74%). In TMS-off, the torque associated with OGWs implies a 34% of the total upward torque, while in TMS-on represents only the 20%. Since the torque associated

to OGWs mostly acts in this region (i.e., there is almost no upward outgoing torque from OGWs into de mesosphere), the contribution from PWs to the total torque reduces to 40% instead of the 58% in TMS-on. This means a larger forcing due to resolved PWs in the TMS-on polar stratosphere (Fig. 6a), which agrees with enhanced heat flux (Fig. 2) and the increased frequency of SSW (Fig. 1). In March (Fig. 6b), the total forcing relative to the incoming upward fluxes remains similar to that of December, and between simulations (77% in TMS-on and 76% in TMS-off in March). However, the OGWs contribution to the total upward torque from OGWs in TMS-off is reduced for March (from 34% to 20%), so the contribution from PWs in the region increases to maintain the 76%. This enhanced relative contribution from PWs in TMS-off is similar to the PW contribution in TMS-on, which explains that the TMS-off frequency of SSWs in March is higher than in December and similar to that on TMS-on. Overall, our results reveal a compensation mechanism be-

tween PW and GW forcing that takes place in the northern winter stratosphere and is able to explain the intraseasonal effects of the TMS parametrization.

4 Conclusions

This study identifies the mechanism by which turbulent mountain stress (TMS) influences stratospheric winter variability in WACCM and leads to a realistic frequency of Sudden Stratospheric Warmings (SSWs). Comparison of two runs with the only difference being the implementation of TMS parametrization in one of them (TMS-on) revealed that the difference between simulations resides on the configuration of the climatological flow, rather than in its variability (anomalous transient eddies). In TMS-off, the climatological planetary waves (PWs) in the lower stratosphere are weaker from December to February, and their interference with transient eddies do not reach the required strength to initiate SSW. In March, the background conditions become similar between simulations, as do the SSW frequencies.

The main effect of including a TMS parametrization is to reduce the surface winds and thus to decrease the upward propagation and dissipation of orographic gravity waves (OGWs) in the stratosphere. We have shown that this effect is particularly important above regions with high topography, primary the Rocky Mountains and the Himalayas, and exhibits intraseasonal variations, being stronger in early than in late winter. As a result, the surface wind configuration in TMS-on is closer to reanalysis, displaying a weak seasonal cycle, while in TMS-off the surface winds are overestimated, mainly in early winter, and so it is the OGWD in the stratosphere . The increased OGWD in TMS-off forces weaker zonal winds in the lower stratosphere, particularly in the southern flank of the subtropical jet. The associated changes in the refractive index favor enhanced (reduced) PW propagation towards subtropical (high) latitudes. However, this mechanism is observed to persist for the entire winter, and thus appears unable to explain the intraseasonal differences found in SSW frequency between simulations.
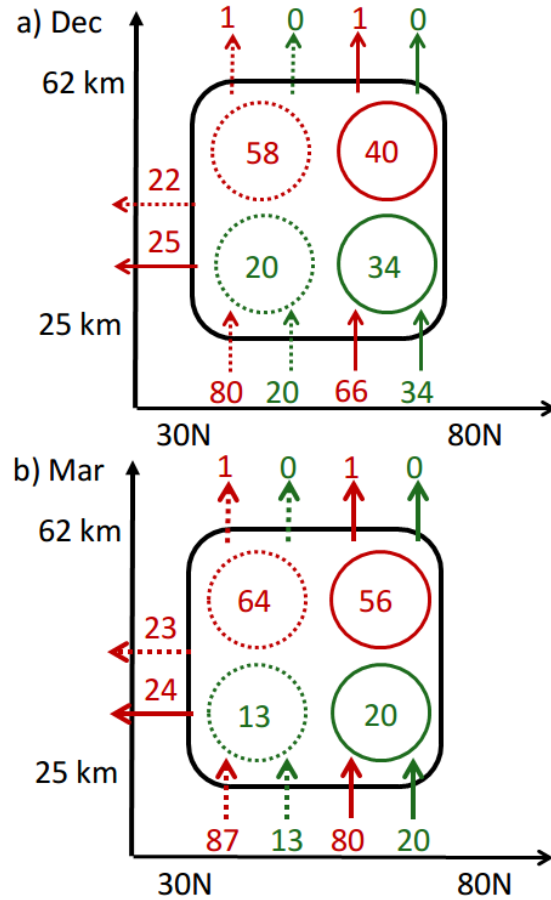
Figure 6: Climatological (1955-2005) wave momentum fluxes (arrows, denoting the direction of propagation) and their associated zonal-mean torques integrated along the boundaries of a region (denoted by the black boxes) bounded by latitudes $[30-80]°$N and from 25 to 62 km. The numbers next to the dashed (solid) arrows represent the relative contributions of the wave-induced torques in the TMS-on (TMS-off) simulation. Numbers in the dashed (solid) circles within each box are the result of evaluating the sum of the wave torques along all boundaries in TMS-on (TMS-off) and characterize the wave forcing in the region denoted by the box. Red and green colors are used for PWs and OGWs, respectively. Results are shown for (a) December and (b) March. For each simulation and month, torques are expressed as percentages of the total (PW + OGW) torque at the lower boundary.

To explain the intraseasonal effects of the TMS, we examine the compensation mechanism between resolved PWs and parametrized OGWs first proposed by Cohen et al. (2013, 2014). Although a similar process was claimed to explain the timing of the final warming in the Southern Hemisphere (Scheffler and Pulido 2015) there is,

as far as we know, no study that has appealed to this mechanism in the context of SSW occurrence. This compensation paradigm consists of a PW response to the OGWD that acts to preserve the total forcing in the middle and upper stratosphere by modification of their relative contributions. Accordingly, the Eliassen-Palm flux divergence (EPFD) increases in TMS-on due to a decreased OGWD, favoring the probability of SSWs. The opposite occurs for TMS-off, showing reduced EPFD in December due to the enhanced OGWD in the stratosphere. The intra-seasonal (December-to-March) differences in surface wind and OGWD are weaker in TMS-on than in TMS-off, which displays less OGWD in March compared to December. Hence, consistent with the compensation paradigm, the EPFD is enhanced in March in TMS-off, which explains why this simulation displays increased SSW frequency in late winter.

The failure of most GCMs to produce a realistic intra-seasonal variation of SSW frequency was noted by Charlton-Pérez et al. (2013) in the models that participated in the CMIP5 project. All GCMs showed SSW frequencies shifted to late winter, similar to our TMS-off simulation, and in particular low-top models overestimated the occurrence in March. Herein, we have found that the compensation mechanism between PWs and OGWs operates in WACCM. It would be interesting to see if it does in other models. This would help to improve GW parametrizations in order to reproduce an adequate winter background for SSW occurrence and hence, to improve stratospheric winter variability.

References

Andrews, D.G. and M.E.Mclntyre, 1976: Planetary waves in horizontal and vertical shear: The generalized Eliassen-Palm relation and the mean zonal acceleration J. Atmos. Sci., 33: 2031-2048.

Baldwin, M. P., and T. J. Dunkerton, 2001: Stratospheric harbingers of anomalous weather regimes. Science, 294, 581–584, doi:10.1126/science.1063315.

Butler, A. H., D. J. Seidel, S. C. Hardiman, N. Butchart, T. B. and A. M., 2015: Defining sudden stratospheric warmings. Bull. Am. Meteorol. Soc., 1–41.

Charlton-Perez, A. J., Baldwin, M. P., Birner, T., Black, R. X., Butler, A. H., Calvo, N.,... and Kim, J., 2013: On the lack of stratospheric dynamical variability in low-top versions of the CMIP5 models. J. Geophys. Res. Atmos., 118, 2494–2505, doi:10.1002/jgrd.50125.

Charlton, A. J., and L. M. Polvani, 2007: A New Look at Stratospheric Sudden Warmings. Part I: Climatology and Modeling Benchmarks. J. Clim., 20, 449–469, doi:10.1175/JCLI3996.1.

Cohen, N. Y., E. P. Gerber, and O. Bühler, 2013: Compensation between Resolved and Unresolved Wave Driving in the Stratosphere: Implications for Downward Control. J. Atmos. Sci., 70, 3780–3798, doi:10.1175/JAS-D-12-0346.1.

——, E. P. Gerber, and O. Bühler, 2014: What Drives the Brewer–Dobson Circulation? J. Atmos. Sci., 71, 3837–3855, doi:10.1175/JAS-D-14-0021.1.

Coy, L., S. Eckermann, and K. Hoppel, 2009: Planetary Wave Breaking and Tropospheric Forcing as Seen in the Stratospheric Sudden Warming of 2006. J. Atmos. Sci., 66, 495–507, doi:10.1175/2008JAS2784.1.

Gómez-Escolar, M., S. Fueglistaler, N. Calvo, and D. Barriopedro, 2012: Changes in Polar Stratospheric Temperature Climatology in Relation to Stratospheric Sudden Warming Occurrence. Geophys. Res. Lett.,.

Kalnay, E., and Coauthors, 1996: The NCEP/NCAR 40-Year Reanalysis Project. Bull. Am. Meteorol. Soc., 77, 437–471, doi:10.1175/1520-0477(1996)077<0437:TNYRP>2.0.CO;2.

Krüger, K., B. Naujokat, and K. Labitzke, 2005: The Unusual Midwinter Warming in the Southern Hemisphere Stratosphere 2002: A Comparison to Northern Hemisphere Phenomena. J. Atmos. Sci., 62, 603–613, doi:10.1175/JAS-3316.1.

Limpasuvan, V., D. W. J. Thompson, and D. L. Hartmann, 2004: The Life Cycle of the Northern Hemisphere Sudden Stratospheric Warmings. J. Clim., 17, 2584–2596, doi:10.1175/1520-0442(2004)017<2584:TLCOTN>2.0.CO;2.

Marsh, D. R., M. J. Mills, D. E. Kinnison, J.-F. Lamarque, N. Calvo, and L. M. Polvani, 2013: Climate Change from 1850 to 2005 Simulated in CESM1(WACCM). J. Clim., 26, 7372–7391, doi:10.1175/JCLI-D-12-00558.1. http://journals.ametsoc.org/doi/abs/10.1175/JCLI-D-12-00558.1.

Matsuno, T., 1970: Vertical Propagation of Stationary Planetary Waves in the Winter Northern Hemisphere. J. Atmos. Sci., 27, 871–883, doi:10.1175/1520-0469(1970)027<0871:VPOSPW>2.0.CO;2.

——, 1971: A dynamical model of the stratospheric sudden warming. J. Atmos. Sci., 28, 1479–1494, doi:10.1175/1520-0469(1971)028<1479:ADMOTS>2.0.CO;2.

McFarlane, N.A., 1987: The effect of orographically excited gravity wave drag on the general circulation of the lower stratosphere and troposphere. J. Atmos. Sci., 44, 1775–1800.

McLandress, C., and N. a. McFarlane, 1993: Interactions between Orographic Gravity Wave Drag and Forced Stationary Planetary Waves in the Winter Northern Hemisphere Middle Atmosphere. J. Atmos. Sci., 50, 1966–1990, doi:10.1175/1520-0469(1993)050<1966:IBOGWD>2.0.CO;2.

Mechoso, C. R., K. Yamazaki, A. Kitoh, and A. Arakawa, 1985: Numerical forecasts of stratospheric warming events during the winter of 1979. Mon. Weather Rev. 113,1015-1029.

Nishii, K., H. Nakamura, and T. Miyasaka, 2009: Modulations in the planetary wave field induced by upward-propagating Rossby wave packets prior to stratospheric sudden warming events: A case-study, Q. J. R. Meteorol. Soc., 135, 39-52.

Palmeiro, F. M., D. Barriopedro, R. García-Herrera, and N. Calvo, 2015: Comparing Sudden Stratospheric Warming Definitions in Reanalysis Data. J. Clim., 150709110342004, doi:10.1175/JCLI-D-15-0004.1. http://journals.ametsoc.org/doi/abs/10.1175/JCLI-D-15-0004.1.

Palmer, T. N., 1981a: Diagnostic study of a wavenumber- 2 stratospheric sudden warming in a transformed Eulerian-mean formalism. J. Atmos. Sci., 38, 844– 855.

——, T. N., 1981b: Aspects of stratosphere sudden warmingstudied from atransformed Eulerian-mean viewpoint. J. Geophys. Res., 86, 9679–9687.

Richter, J. H., F. Sassi, and R. R. Garcia, 2010: Toward a Physically Based Gravity Wave Source Parameterization in a General Circulation Model. J. Atmos. Sci., 67, 136–156, doi:10.1175/2009JAS3112.1.

Scheffler, G., and M. Pulido, 2015: Compensation between resolved and unresolved wave drag in the stratospheric final warmings of the Southern hemisphere. J. Atmos. Sci., 150717145012004, doi:10.1175/JAS-D-14-0270.1.

Scott, R., D. Dritschel, L. Polvani, and D. Waugh, 2004: Enhancement of Rossby wave breaking by steep potential vorticity gradients in the winter stratosphere. J. Atmos. Sci., 61, 904–918.

Shaw, T. a., J. Perlwitz, and O. Weiner, 2014: Troposphere-stratosphere coupling: Links to North Atlantic weather and climate, including their representation in CMIP5 models. J. Geophys. Res. Atmos., 2013JD021191, doi:10.1002/2013JD021191.

Sigmond, M., and J. F. Scinocca, 2010: The

influence of the basic state on the Northern Hemisphere circulation response to climate change. J. Clim., 23, 1434–1446, doi:10.1175/2009JCLI3167.1.

——, and T. G. Shepherd, 2014: Compensation between resolved wave driving and parameterized orographic gravity wave driving of the Brewer-Dobson circulation and its response to climate change. J. Clim., 27, 5601–5610, doi:10.1175/JCLI-D-13-00644.1.

——, J. F. Scinocca, V. V. Kharin, and T. G. Shepherd, 2013: Enhanced seasonal forecast skill following stratospheric sudden warmings. Nat. Geosci., 6, 98–102, doi:10.1038/ngeo1698.

Siskind, D. E., S. D. Eckermann, L. Coy, J. P. McCormack, and C. E. Randall, 2007: On recent interannual variability of the Arctic winter mesosphere: Implications for tracer descent. Geophys. Res. Lett., 34, L09806, doi:10.1029/2007GL029293. Smith, K. L., and P. J. Kushner, 2012: Linear interference and the initiation of extratropical stratosphere-troposphere interactions. J. Geophys. Res. Atmos., 117, 1–16, doi:10.1029/2012JD017587,2012.

Wexler, H. (1959). Seasonal and other temperature changes in the Antarctic atmosphere. Quarterly Journal of the Royal Meteorological Society, 85(365), 196-208.

Chapter 5

Interactions between sudden stratospheric warmings and the Brewer-Dobson circulation

Interactions between sudden stratospheric warmings and the Brewer-Dobson circulation

Abstract

The Brewer-Dobson circulation (BDC) and sudden stratospheric warmings (SSWs) represent the most illustrative phenomena of polar stratospheric variability in the winter Northern Hemisphere. While several studies have assessed the influence of SSWs on tropical upwelling, the interactions between SSWs and the deep branch of the BDC have not been addressed in detail. Here, two simulations performed with the Whole Atmospheric Community Climate Model (WACCM) were analyzed to explore the BDC response to SSW occurrence in a fixed and increasing greenhouse gases (GHGs), respectively. Results indicate that the increased wave activity at extratropical latitudes of the upper stratosphere before the SSW induces an acceleration in the downwelling branch of the BDC. After the vortex disruption by the SSW, wave activity towards the upper polar stratosphere is inhibited, resulting in the opposite effect, so that the BDC weakens for several weeks. These responses of the BDC depend on the timing of the SSW. If a SSW occurs in March, the onset of the polar upwelling of the BDC that characterizes the summer circulation starts earlier. A similar result is obtained for early (i.e., March) final warmings, indicating that these events also advance the BDC transition. The results for a future warming climate scenario project an overall delayed transition of the BDC, but without changing the transition date of all March warmings (either SSWs or SFWs) when compared to the present climate. This means that their effect on the BDC transition becomes stronger.

1 Introduction

The Brewer-Dobson Circulation (BDC) is a large-scale meridional overturning responsible for the mass transport between the tropics and the poles in the stratosphere. Attending to the location and timescale of the air movements, two main branches of the BDC can be distinguished (e.g., Beagley et al. 1997, Plumb 2002, Birner and Bönisch 2011). The faster shallow branch shows tropical upwelling up to the lower stratosphere and downwelling confined to low latitudes. The upper and slower cell is referred to as the deep branch, and connects the middle and upper tropical stratosphere of the summer hemisphere with the mid- and high-latitudes of the winter hemisphere. The BDC is wave driven, mostly by planetary waves (PWs), and hence its fluctuations can be explained by wave interactions with the background flow (Holton et al. 1995). On the other hand, sudden stratospheric warmings (SSWs), characterized by a rapid temperature increase of the polar stratosphere, are capable of altering stratospheric and tropospheric conditions for several weeks (e.g., Limpasuvan et al. 2004), thus becoming a prominent example of stratosphere-troposphere coupling (Baldwin and Dunkerton 2001).

Interactions between the BDC and SSWs are known since the early studies of Matsuno (1971). The wave dissipation in the polar stratosphere associated with SSWs induces upwelling and cooling at low latitudes (e.g., Randel et al. 2002, Kodera 2006). Distinction between the shallow and the deep branches of the BDC has been recently considered (Birner and Bönisch 2011), but the SSW signatures on the BDC have focused on the tropical upwelling of the lower stratosphere. Thus, using model simulations, McLandress and Shepherd (2009) showed an increase in the tropical upwelling at 70 hPa during SSWs, while in reanalysis data Abalos et al. (2015) found a correspondence between strong upwelling events and SSW occurrence at the same altitude. Gómez-Escolar et al. (2014)

even quantified the SSWs effects on the tropical cooling in the middle stratosphere. However, the signature of the SSW life cycle on the polar downwelling of the deep branch have not been assessed in detail. At their onset, SSWs are characterized by anomalous upward wave activity coming from the troposphere (Polvani and Waugh 2004, Limpasuvan et al. 2004) while after the vortex breakdown, upward propagation is inhibited and wave convergence in the upper stratosphere is dramatically reduced. Since the downwelling branch of the BDC is also driven by planetary wave dissipation (Plumb 2002), some imprint on the BDC might be expected.

On the other hand, the rate at which the BDC pumps tropospheric air into the stratosphere determines the time scales at which Ozone Depleting Substances (ODS) are processed and removed (Holton 1995), which is relevant in the context of anthropogenic activities. Therefore, the impact of SSWs on the BDC might involve changes regarding how ODS and other chemical processes are processed in the upper stratosphere. Since the world is undergoing an anthropogenic climate change, it is also important to investigate if the relationship between SSWs and the BDC changes in a warming climate scenario. This is an interesting question because of the current uncertainties regarding future changes in the BDC and SSWs. Many model studies have shown an acceleration of the shallow branch of the BDC in a warmer climate (Butchart 2014 and references therein), which is consistent with results from observations (Arblaster and Gillet et al. 2014). However, trends in the deep branch under climate change conditions are not clear in the observational record, and both positive and negative trends have been reported (e.g., Engel et al. 2009, Bonisch et al. 2011, Diallo 2012, Monge-Sanz et al. 2013). These contradictory results are associated with the fact that the BDC cannot be directly measured from observational data and has to be estimated by tracers. This includes too many uncertainties, making difficult to find significant trends (Arblaster and Gillet et al. 2014). Future changes in SSW frequency are also controversial. Although Charlton-Perez et al. (2008) obtained a small positive trend in SSW occurrence, McLandress and Shepherd (2009) argued that the result depended on the

method to define SSWs, and found no trends using a SSW definition insensitive to changes in the background flow. Moreover, Kim et al. (2017) reported that most CMIP5 models project an increasing trend in SSW occurrence, although it is not significant and the dynamical mechanisms remain unclear. In particular, for the Whole Atmosphere Community Climate Model (WACCM), Hansen et al. (2014) did not find a significant increase in SSW occurrence due to changes in anthropogenic forcing.

This study aims to explore the influence of SSWs on the deep branch of the BDC. We attempt to contribute to a better understanding of the BDC-SSW interactions and their future changes by analyzing two simulations from WACCM for the 1955-2099 period. One of the simulations uses fixed Greenhouse Gases (GHGs) and ODS, and the other includes time-evolving GHGs and ODS, based on the Representative Concentration Pathway 8.5 (RCP8.5).

2   Model simulation and Methods

The use of reanalysis data to characterize the BDC might be misleading due to data uncertainties in the vertical motion, which motivates the use of model integrations. We used daily data from the WACCM model in its version 4 (Marsh et al. 2013). The model consists of four coupled components: land, sea ice, ocean and atmosphere with fully interactive chemistry. The atmospheric component of WACCM extends up to 140 km along 66 vertical levels and has a longitude-latitude resolution of 2.5º x 1.9º. The model includes natural forcings, such as the solar cycle (Lean et al. 2005) and volcanic aerosols (Tilmes et al. 2009), as well as a nudged quasi-biennial oscillation (Matthes et al. 2010).

Two simulations of 145 years each (from 1955 to 2099), denoted as fixed-GHG and RCP8.5, have been analyzed. The RCP8.5 simulation includes observed CO_2 concentrations up to 2005 and a continuous CO_2 increase, which is approximately linear (80 ppmv per decade) from 2050 to 2099 (van Vuuren et al. 2007). The fixed-GHG experiment is similar to the RCP8.5 run, but keeps GHGs and ODS fixed at the
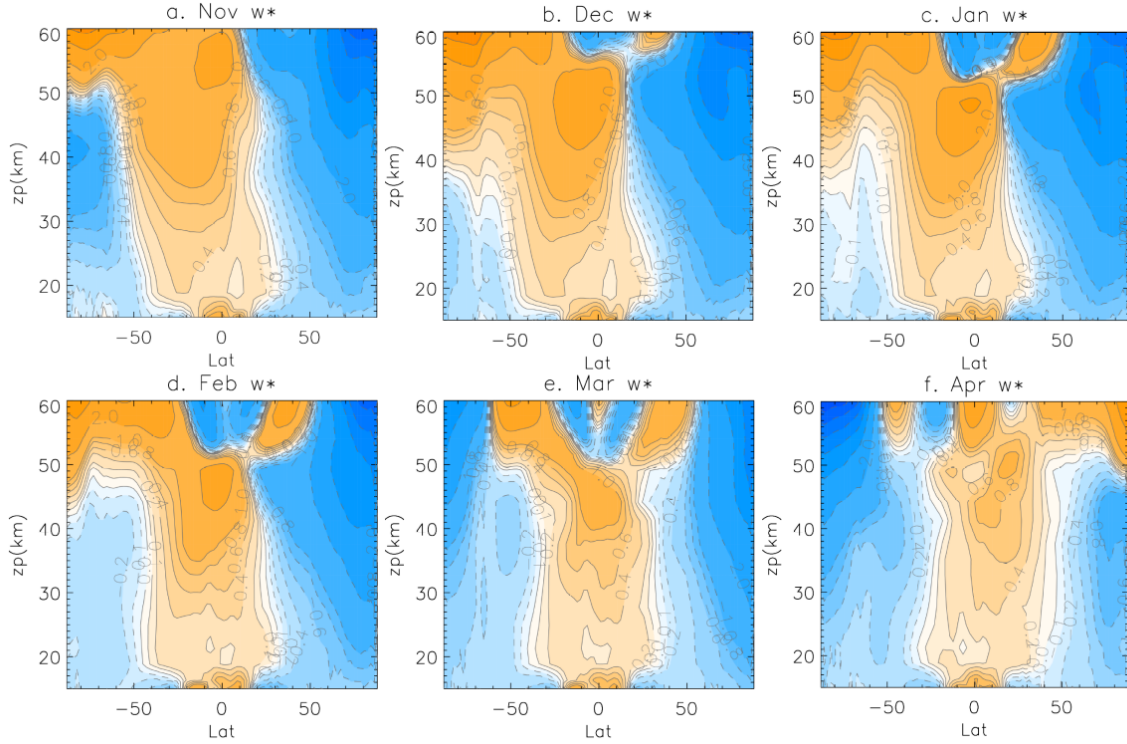
Figure 1: Monthly climatology of $\overline{w}^*$ in the fixed-GHGs simulation from November to April. Contour intervals are: $0, \pm 0.1, \pm 0.2\ mm\ s^{-1}$ and every $0.2\ mm\ s^{-1}$ up to $\pm 1\ mm\ s^{-1}$, and then every $1\ mm\ s^{-1}$. Orange (blue) shading and solid (dashed) lines represent positive (negative) values.

1960s values, which correspond to an annual CO_2 mean value of 316 ppmv. Mixing ratios of ozone depleting substances (ODS) decrease from approximately 4ppbv in 2005 to approximately 1.7ppbv in 2100 in terms of equivalent effective stratospheric chlorine (EESC). Thus, the only difference between simulations is the consideration of changes in the anthropogenic forcing.

The BDC is diagnosed by the residual vertical velocity, $\overline{w}^*$, as the mathematical approach to the residual mean meridional circulation in the transformed Eulerian-mean (TEM) framework (Eq. 1, Andrews et al. 1987):

$$\overline{w}^* \equiv \overline{w} + (a \cdot cos\phi)^{-1} \left(cos\phi \frac{\overline{v'\theta'}}{\overline{\theta}_z} \right)_\phi \qquad (1)$$

where the asterisk represents TEM notation, the overbars indicate zonal-mean and primes deviations from it; v and w are the meridional and vertical components of the wind, θ is the potential temperature, a is the Earth's radius and ϕ is the latitude.

We also defined the BDC transition from winter to summer circulation, i.e., the date when the summer polar upwelling branch of the BDC is well established in the northern upper stratosphere. This is identified as the day, between 1 March and 31 May, when $\overline{w}^*$ changes from negative (downwelling) to positive (upwelling) values at 70°N and 0.3 hPa. To avoid high frequency variations, $\overline{w}^*$ has been previously smoothed with a 15-day running mean. Our conclusions hold even though the resulting exact BDC transition dates are sensitive to variations of the previous parameters.

SSWs are defined as zonal-mean zonal wind reversals at 10 hPa from November to March in a range of latitudes from 60 to 75°N, following Palmeiro et al. (2015). Those events at which the zonal-mean zonal wind does not return to westerly for at least 10 days before the 30 of April are considered stratospheric final warmings (SFWs), as in Charlton and Polvani (2007).
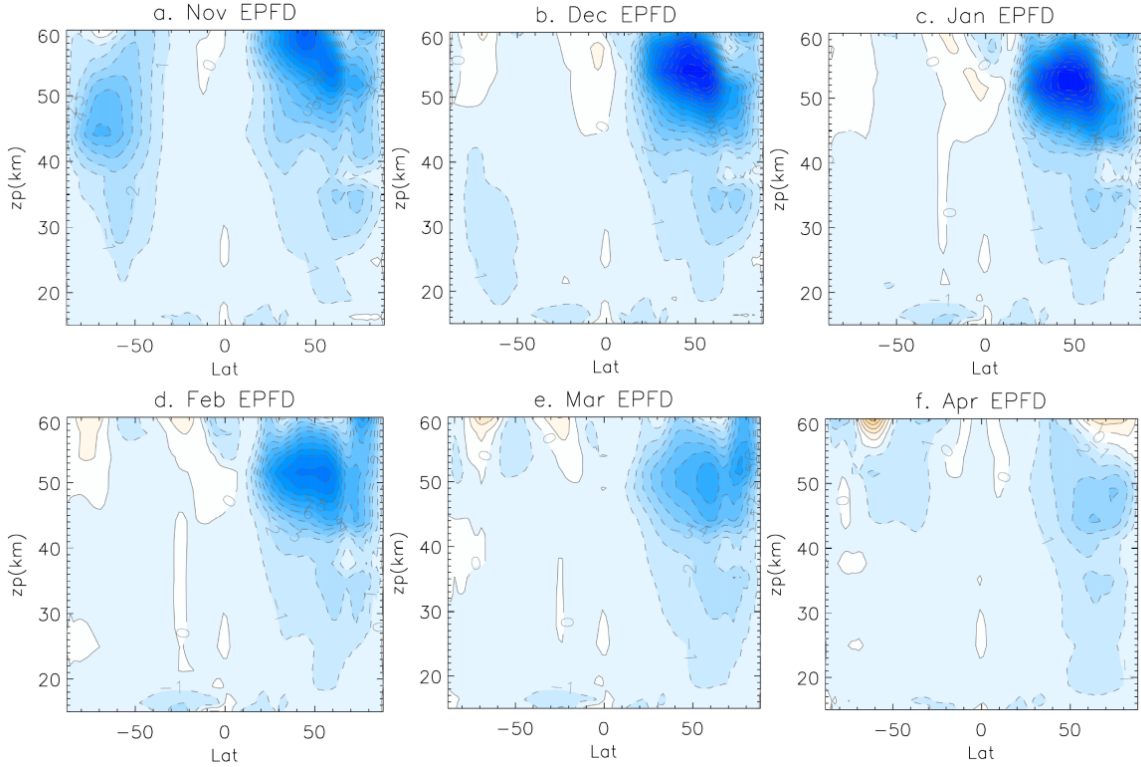
Figure 2: Monthly climatology of the EPFD in the fixed-GHG simulation from November to April. Contours are every 2.5 $m\ s^{-1}day^{-1}$. Orange (blue) shading and solid (dashed) lines represent positive (negative) values.

Anomalies in the fixed-GHG simulation are calculated with respect to the climatology of the entire period. In the RCP8.5 simulation, anomalies are computed from the climatology of the first 50 years. This allows us to take into account anthropogenic induced changes, which will be quantified by comparing the last 50 years with the first 50 years of the RCP8.5 simulation. The significance of the anomalies in the composites is assessed with a 1000-trial Monte Carlo test at the 95% confidence level. A Mann-Whitney test at the 95% confidence level is also used to assess whether two distributions are significantly different.

3   Sudden stratospheric warming influence on the strength of the Brewer-Dobson circulation

Figure 1 illustrates the monthly-mean climatological $\overline{w}^*$ from November to April in the

fixed-GHG simulation. As expected, upwelling ($\overline{w}^* > 0$) appears in the tropical middle and upper stratosphere (where it is maximum) and the midlatitudes of the Southern Hemisphere (SH) during the boreal winter. Downwelling $\overline{w}^* < 0$) occurs mostly in mid and high latitudes of the Northern Hemisphere (NH) from December to February. The transition to the summer circulation begins in March, when the upwelling in the stratosphere is centered in the tropics, and the downwelling occurs simultaneously in both hemispheres. The BDC seasonality is driven by that of the wave forcing, which is well documented in the literature (e.g., Charney and Drazin 1961). The main forcing of the deep branch is the momentum deposited by PWs (not shown), which are resolved in WACCM and thus can be characterized by the Eliassen-Palm flux divergence (EPFD) (Andrews et al. 1987). Figure 2 shows the monthly evolution of the EPFD through the extended winter. A direct comparison with Fig. 1 shows that the months with the largest wave convergence (EPFD < 0) in the NH (December and January) correspond to
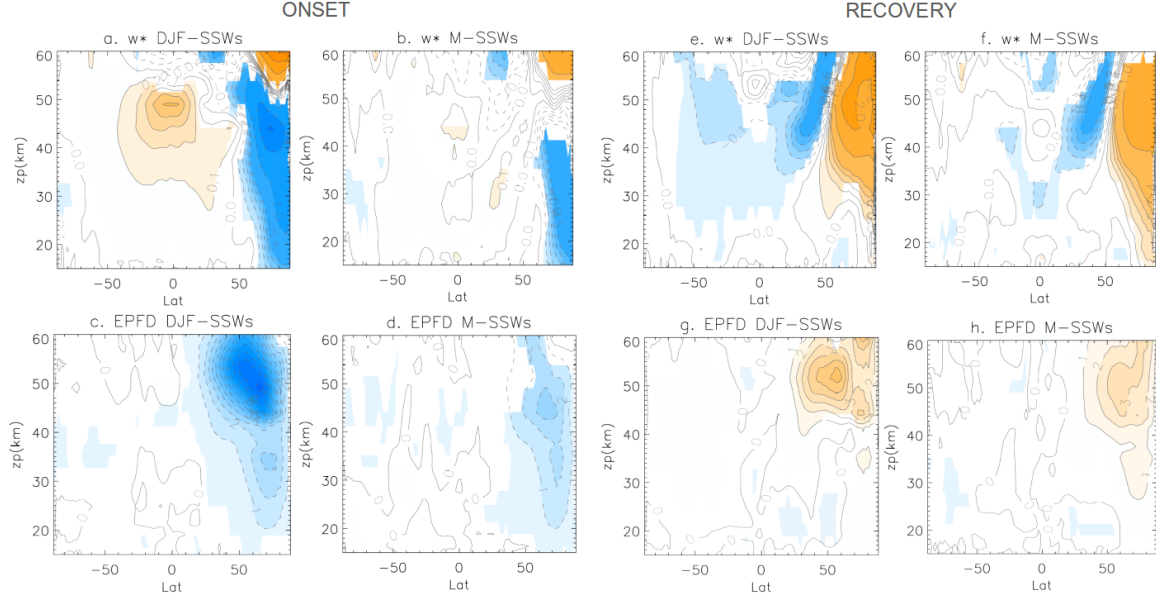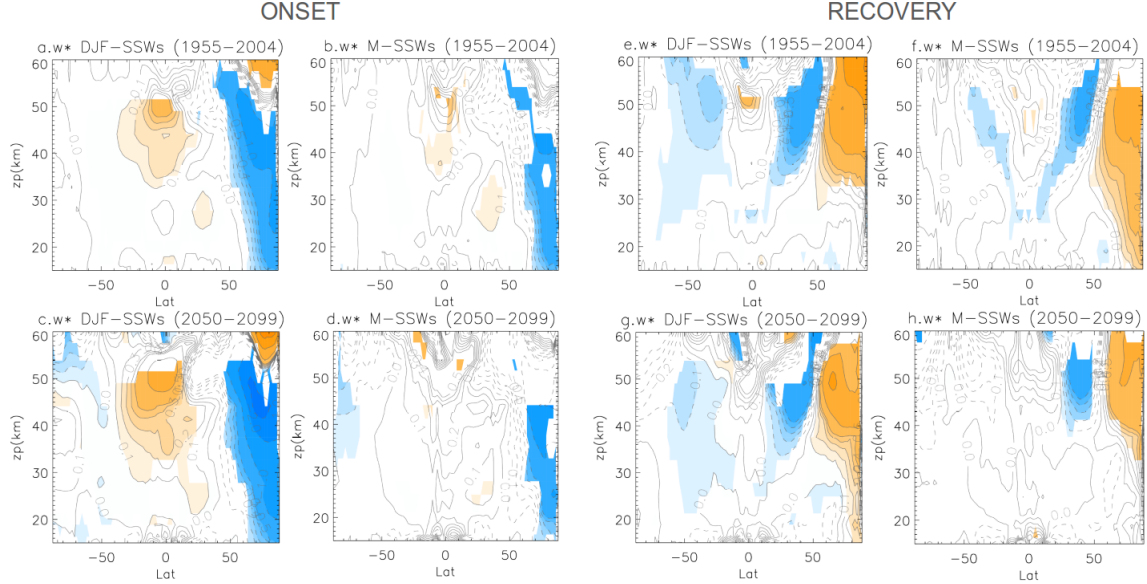
Figure 3: Composites of $\overline{w}^*$ (top) and EPFD (bottom) anomalies for the [-30,0]-day period before the SSW central date (a,b,c,d) and for the [5,35]-day period after the SSW central date (e,f,g,h). Contour intervals are every 0.1 $mm\ s^{-1}$ up to ± 0.5, $\pm 1\ mm\ s^{-1}$, and then every 1 $mm\ s^{-1}$ for $\overline{w}^*$ (top panels) and every 1 $m\ s^{-1}day^{-1}$ for EPFD (bottom panels). Orange (blue) shading and solid (dashed) lines represent positive (negative) values. Only significant values at the 95% confidence level under a 1000-trial Monte Carlo test are shaded.

those showing the strongest downwelling in the polar stratosphere. As wave convergence starts to decrease in the upper northern stratosphere, the NH polar downwelling weakens and by March – April it is well established in the SH.

To analyze the impact of SSWs on the BDC, we have composited the anomalies of $\overline{w}^*$ and the EPFD for the [-30,0]-day period before the central date of the SSWs and for the [5,35]-day period after SSWs (Figure 3). These periods are chosen following previous studies (e.g., Limpasuvan et al. 2004) and they will be referred to as the SSW "onset" and "recovery", respectively. Since there is intraseasonal variability in the background winter climatology, we have composited the SSW events of December-January-February (DJF) separately from those of March. This classification of SSWs is further justified by additional analyses at monthly time scales (not shown), which confirm a distinctive signal of March SSWs. Overall, SSW occurrence acts to strength the BDC during its onset. This is particularly true for SSWs in DJF. In this case, the largest tropical upwelling and polar downwelling in the

upper stratosphere increase by 25% compared to climatological values, while the largest polar downwelling in the middle and lower stratosphere increases up to 50%. However, the effect of the SSWs that occur in March is only significant over the downwelling branch. These results agree with composites of the EPFD, which show larger wave convergence during the onset of DJF SSWs than of March events (Fig. 3, bottom panels). These differences could be related to the weaker polar vortex at the end of the winter, which would require less wave forcing for a SSW to occur and hence a weaker imprint on the BDC. The SSW effect on the BDC reverses after the vortex disruption, in the recovery phase. Since upward wave propagation diminishes at high latitudes because of the zonal wind reversal, the recovery period is characterized by positive anomalies of the EPFD (i.e., the climatological convergence weakens, Figs. 3g and 3h), which is in agreement with the slowdown of the BDC shown in Figs. 3e and 3f. This interaction between SSWs and the BDC is consistent with the "stratospheric control" of the BDC introduced in Gerber (2012). It establishes that the strength of the stratospheric

87

Figure 4: Composites of $\overline{w}^*$ anomalies for the [-30,0]-day period before the DJF SSW (a,c) and March SSW (b,d) and for the [5,35]-day period after the DJF SSW (e,g) and March SSW (f,h) central date for the period 1955-2004 (top) and the period 2050-2099 (bottom). Contour intervals are every 0.1 $mm\ s^{-1}$ up to ± 0.5, ± 1 $mm\ s^{-1}$, and then every 1 $mm\ s^{-1}$ for $\overline{w}^*$. Orange (blue) shading and solid (dashed) lines represent positive (negative) values. Only significant values at the 95% confidence level under a 1000-trial Monte Carlo test are shaded.

polar vortex modulates the wave breaking level. Accordingly, the stronger polar vortex preceding the SSW (Limpasuvan et al. 2004) favors the increase of wave convergence that accelerates the BDC during the SSW onset (Figs. 3c and 3d). This "stratospheric control" suggests that the occurrence of SSWs affects the BDC, instead of the BDC affecting the SSW occurrence.

Next, we explore possible anthropogenic changes on the reported SSW impacts on the BDC. To do that, we compare the last 50 years (from 2050 to 2099, future) with the first 50 years (from 1955 to 2004, past) of the RCP8.5 simulation. Figure 4 shows the composites of $\overline{w}^*$ anomalies for the onset and the recovery phase of SSWs occurring in DJF and March of the first and the last 50 years of RCP8.5. The onset (Figs. 4a and 4b) and recovery (Figs. 4e and 4f) composites for the past show a similar picture as in the fixed-GHG simulation (Figs.3a and 3b and Figs. 3e and 3f, respectively), as one would expect since there are small differences between the anthropogenic forcings of fixed-GHG and the past period of the RCP8.5 experiment. On the contrary, composites for the future indicate

an enhanced response of the BDC to the SSW onset, with $\overline{w}^*$ anomalies that double those of the past in the middle and the upper stratosphere. However, this intensification of the downwelling is no longer observed when the composites of the future are computed with respect to the climatology of the last 50 years. In this case, the composites resemble those for the past (not shown). This indicates an overall acceleration of the BDC in the future, rather than a stronger impact of SSWs on the BDC. Finally, as for the recovery phase of SSWs, the positive anomalies of $\overline{w}^*$ at high latitudes in the future are weaker compared to the past (cf. Figs. 4g and 4h). Again, this is related to the stronger downwelling in the background climatology in the future.

4   Sudden stratospheric warming effect on the BDC summer transition

The transition from the winter to the summer BDC is marked by the reversal of $\overline{w}^*$ (i.e., downwelling is replaced by upwelling in the northern
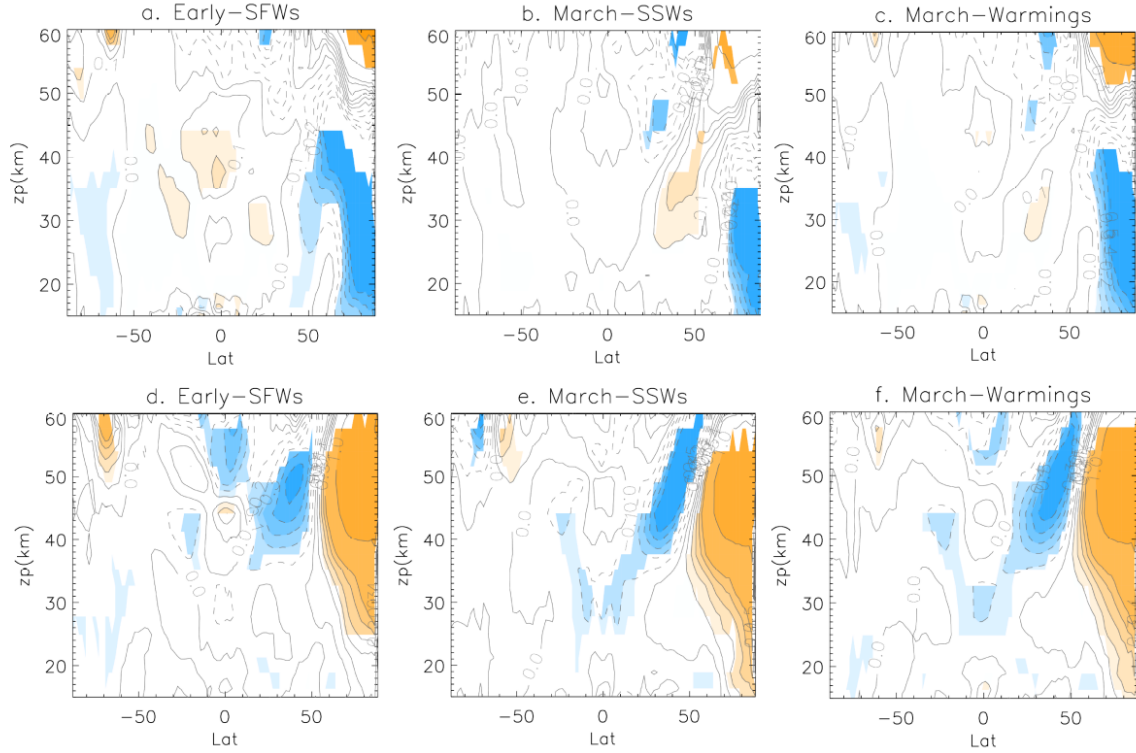
Figure 5: Composites of $\overline{w}^*$ anomalies for March SFWs (a,d), March SSWs (b,e) and all March warmings (c,d) for the [-30,0]-day period before events (top) and the [5,35]-day period after events (bottom). Contour intervals are every 0.1 $mm\ s^{-1}$ up to ± 0.5, $\pm 1\ mm\ s^{-1}$, and then every 1 $mm\ s^{-1}$ for $\overline{w}^*$. Orange (blue) shading and solid (dashed) lines represent positive (negative) values. Only significant values at the 95% confidence level under a 1000-trial Monte Carlo test are shaded.

upper stratosphere). Figure 1 shows that this occurs, on average, from March to April. Since March SSWs were found to decrease the BDC polar downwelling after their occurrence, this raises the question of whether they might have an impact on the BDC transition date to the summer circulation. On the other hand, stratospheric final warmings (SFWs), characterized by the non-return reversal of the zonal-mean zonal wind in the polar upper stratosphere, are often considered as a benchmark of the transition to the summer circulation. SFWs occasionally occur in March (early SFWs, hereafter), suggesting that these events should also be characterized by an early transition to the summer regime. Therefore, in the following analyses, we have considered early SFWs together with March SSWs and we referred to this entire set as March warmings. The joint analysis of March warmings is further supported by previous studies about early SFWs, which have reported similar effects on the polar stratosphere

to those of SSWs (Hu et al. 2014). This is because even though the vortex does not recover after SFWs, the polar jet is also disrupted, such that a similar inhibition of upward propagating waves as that after SSWs occurs. In fact, Figure 5 clearly shows that the impact of early SFWs on the BDC is indistinguishable to that of March SSWs in the fixed-GHG simulation. Similar results are obtained for the RCP8.5 experiment (not shown).

To understand the potential influence of March warmings on the BDC transition, Figure 6a shows the time-height evolution of $\overline{w}^*$ for the composite of March warmings (shaded colors) with the climatological BDC superimposed in black contours. Comparison between the $\overline{w}^*$ composite for March warmings and the entire climatology shows that the shift in the timing of the transition (zero $\overline{w}^*$ line) is larger in the middle and upper stratosphere (cf. black zero curve and green curve). Vertical lines indicate
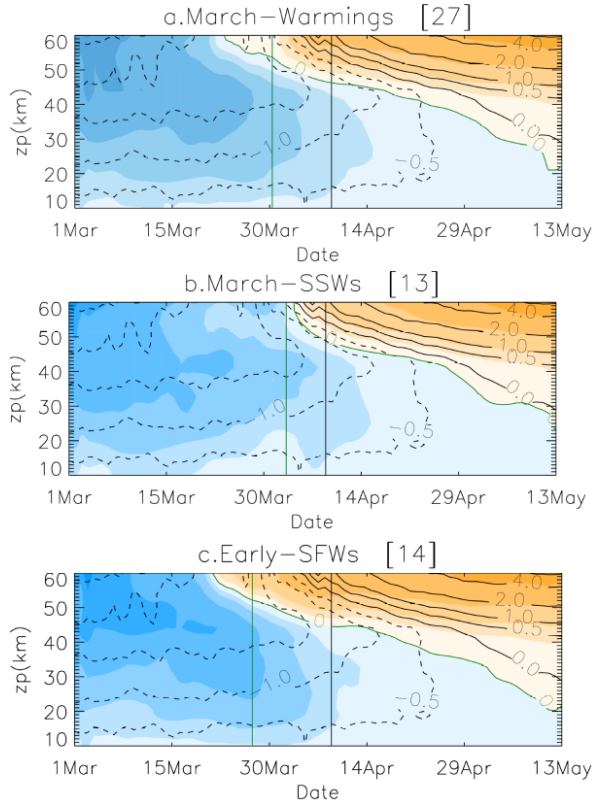
Figure 6: Composites of the time height evolution of $\overline{w}^*$ averaged between (65-90)°N in the fixed-GHG simulation for winters with: (a) March warmings, (b) March SSWs and (c) Early SFWs (shading) and all winters (black contours). Green (black) vertical line indicates the average date of the BDC transition for the composite (climatology). Contours are every 0, ±0.5, ±1, ±2, and then every 2 $mm\ s^{-1}$. Orange (blue) shading and solid (dashed) lines represent positive (negative) values.

Figure 7: Composite of March events (Top) and May final warmings (Bottom) for the Time-height evolution of $\overline{w}^*$ averaged between (65-90)°N (shading) for (a,b) March events, (c,d) May SFWs of the (a,c) first 50 years (b,d) last 50 years of the RCP8.5 simulation, with the corresponding climatology superimposed in black contours. The zero $\overline{w}^*$ line of the corresponding composite is plotted in green. Green (black) vertical line indicates the average date of the BDC transition for the composite (climatology). Contours are every 0, ±0.5, ±1, ±2, and then every 2 $mm\ s^{-1}$. Orange (blue) shading and solid (dashed) lines represent positive (negative) values.

the dates of the climatological BDC transition (black) and the mean transition date for winters with March events (green). The BDC transition date during winters with March warmings occurs 10 days earlier than the climatological transition date. This advance of the summer regime is statistically significant at the 95 % confidence level, using a t-test. It might be argued that the advance of the BDC transition for March warmings is exclusively due to early SFWs, which, by definition, mark the transition to the summer regime. However, this is not the case since, in agreement to Figs. 6b and 6c, the effect of March SSWs on the transition is comparable to that of early SFWs. In fact, the effect of March SSWs becomes stronger as they occur later towards the

end of the month. Thus, SSWs of the second half of March have a stronger impact on advancing the BDC transition than early SFWs (not shown). Then, differences between Figs. 6b and 6c are due to a tendency of early SFWs to occur, on average, later than March SSWs, and hence closer to the climatological BDC transition. Nevertheless, the fact that both March SSWs and early SFWs have qualitative similar impacts justifies the joint analysis of these events.

Under increasing anthropogenic forcing, the average BDC transition into the summer regime occurs later in the future (last 50 years of the simulation) than in the past (first 50 years) (compare black lines in Figures 7a and 7b). However, the dates of the BDC transition for March warmings (green lines) are similar in both periods, which indicates that winters with March warmings do not have an effect on the climatological delay of the BDC transition in the future. Then, the

resulting advance of the transition date due to March warmings is larger (14 days, $p < 0.05$) in a future climate (cf. distance between green and black vertical lines in Figs. 7a and 7b), as compared to the past (10 days, $p < 0.05$).

Given the advance in the BDC transition caused by March warmings, a similar but opposite effect might be expected for late SFWs, i.e. those occurring in May. Indeed, additional analyses (not shown) confirm that late SFWs are associated with a delayed BDC transition Based on this result, one may argue that the climatological delay of the BDC transition is due to an increased frequency of late SFWs (i.e., a delayed timing in the occurrence of SFWs). To illustrate that this is not the case, Figure 8a shows the distributions of the BDC transition dates in the two subperiods of the RCP8.5 experiment. Both distributions are significantly different and as expected, its comparison shows a shift towards the summer in the future, in agreement with Fig. 7. However, this shift into the summer is not reproduced in the distributions of the SFW dates (Fig. 8b), whose difference is not statistically significant between past and future periods. This means that the overall delay in the BDC transition cannot be a consequence of a corresponding delay in the occurrence of SFWs. An important conclusion of these results is that the timing of SFWs does not necessarily reflect the BDC transition (as measured by $\overline{w}^*$). Therefore, the BDC transition and the SFWs seem to occur with relative independence. This further corroborates that the advancing effect of the BDC transition by March warmings is not an artefact due to the inclusion of early SFWs.

5   Conclusions

This study shows a direct relationship between Sudden Stratospheric Warmings (SSWs) and the Brewer-Dobson Circulation (BDC). Moreover, we have found that the occurrence of March SSWs and the timing of the Stratospheric Final Warming (SFW) can modulate the BDC transition from the winter to the summer circulation. The analysis of two simulations with the WACCM model, one with only natural forcings evolving and another based on a climate change scenario lead to the following conclusions:

- There is a tight link between SSWs and the
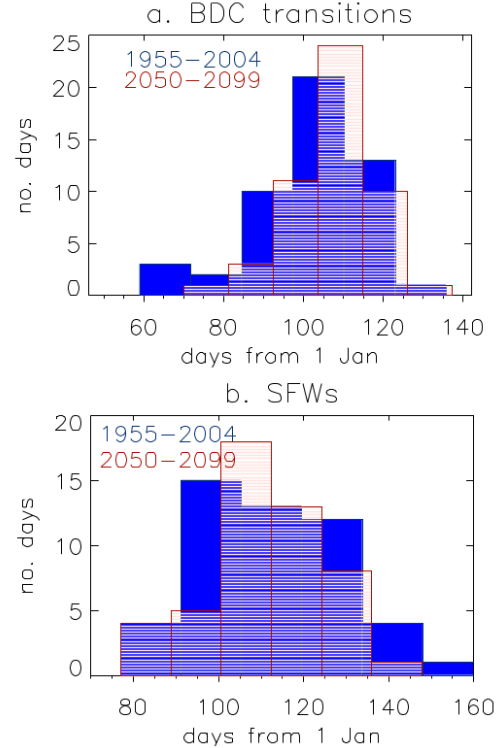
Figure 8: Histograms of the (a) BDC transition and (b) SFWs dates for the 1955-2004 period (blue) and the 2050-2099 period (red) of the RCP8.5 simulation. Abscissas indicate the number of days from the 1st of January.

deep branch of the BDC, with an increase of up to ~50% in the climatological polar downwelling during the month before the occurrence of SSWs. The maximum polar downwelling of the BDC weakens during the month following the SSW by a similar magnitude. These changes are larger when SSWs occur in December-January-February (DJF) than for those occurring in March. The latter show in turn a similar impact on the BDC to that of early (March) SFWs.

- There is an increased planetary wave convergence in the polar stratosphere prior to SSWs, which is consistent with the strengthening of the BDC circulation. After the vortex breakdown, planetary wave propagation is inhibited, in agreement with the simulated BDC deceleration.

- Under enhanced anthropogenic forcing, the influence of the SSW lifecycle on the BDC

strengthens. These changes are due to a projected acceleration of the BDC, because they are no longer observed when the polar downwelling trend is removed.

- Winters with warmings close to the summer regime (i.e., either SSWs in March or early SFWs) show an advanced winter-to-summer transition of the BDC. Thus, March warmings lead to an anticipated polar upwelling in the middle and high latitudes of the upper northern stratosphere.

- Under increasing greenhouse gases, the climatological winter-to-summer transition of the BDC is shifted into the summer. This change cannot be explained by a corresponding delay in the date of occurrence of SFWs, nor by winters with March warmings, whose transition dates remain similar in the future. As a consequence, the future effect of March warmings on advancing the BDC transition gets amplified.

References

Abalos, M., Legras, B., J., F. P. and W., Randel. (2015). Evaluating the advective Brewer-Dobson circulation in three reanalyses for the period 1979 – 2012. Journal of Geophysical Research: Atmospheres, 1–21. doi:10.1002/2015JD023182.

Andrews,D. G., J. R. Holton and C. B. Leovy (1987). Middle atmosphere dynamics. Reviews of Geophysics, 21(2), 283–290. doi:10.1029/RG021i002p00283

Arblaster, J.M., and N.P Gillett (Lead Authors), N. Calvo, P.M. Forster, L.M. Polvani, S.-W. Son, D.W. Waugh, and P.J. Young, Stratospheric ozone changes and climate, Chapter 4 in Scientific Assessment of Ozone Depletion: 2014, Global Ozone Research and Monitoring Project – Report No. 55, World Meteorological Organization, Geneva, Switzerland, 2014.

Baldwin, M. P., and Dunkerton, T. J. (2001). Stratospheric harbingers of anomalous weather regimes. Science, 294(5542), 581–4. doi:10.1126/science.1063315

Beagley, S. R., de Grandpré, J., Koshyk, J. N., McFarlane, N. and Shepherd, T. G. (1997). Radiative-dynamical climatology of the first-generation Canadian Middle Atmosphere Model. Atmosphere Ocean, 35(July), 293–331. doi:10.1080/07055900.1997.9649595

Birner, T., and Bönisch, H. (2011). Residual circulation trajectories and transit times into the extratropical lowermost stratosphere. Atmospheric Chemistry and Physics, 11(2), 817–827. doi:10.5194/acp-11-817-2011

Bönisch, H., A. Engel, Th. Birner, P. Hoor, D.W. Tarasick, and E.A. Ray (2011). On the structural changes in the Brewer-Dobson Circulation after 2000, Atmos. Chem. Phys., 11, 3937-3948, doi: 10.5194/acp-11-3937-2011

Butchart, N. (2014), The Brewer–Dobson circulation, Rev. Geophys., 52, 157–184, doi:10.1002/2013RG000448.

Charlton, A. J., and Polvani, L. M. (2007). A New Look at Stratospheric Sudden Warmings. Part I: Climatology and Modeling Benchmarks. Journal of Climate, 20(3), 449–469. doi:10.1175/JCLI3996.1

Charlton-Perez, A., J., Polvani, L. M., Austin, J., and Li, F. (2008). The frequency and dynamics of stratospheric sudden warmings in the 21st century. Journal of Geophysical Research Atmospheres, 113(16), 1–12. doi:10.1029/2007JD009571

——, A. J., Baldwin, M. P., Birner, T., Black, R. X., Butler, A. H., Calvo, N., ... Watanabe, S. (2013). On the lack of stratospheric dynamical variability in low-top versions of the CMIP5 models. Journal of Geophysical Research: Atmospheres, 118(6), 2494–2505. doi:10.1002/jgrd.50125

Charney, J. G., and Drazin, P. G. (1961). Propagation of Planetary-Scale Disturbances from the Lower into the Upper Atmosphere. Journal of Geophysical Research, 66 (1), 83–109. doi:10.1029/JZ066i001p00083

Diallo, M., B. Legras, and A. Chédin (2012). Age of stratospheric air in the ERA-Interim, Atmos. Chem. Phys., 12, 12133-12154, doi:10.5194/acp-12-12133-2012

Engel, A., et al. (2009), Age of stratospheric air unchanged within uncertainties over the past 30 years, Nat. Geosci., 2, 28–31, doi:10.1038/ngeo388

Gerber, E. P. (2012). Stratospheric versus Tropospheric Control of the Strength and Structure of the Brewer–Dobson Circulation. Journal of the Atmospheric Sciences, 69(9), 2857–2877. doi:10.1175/JAS-D-11-0341.1

Gómez-Escolar, M., N. Calvo, D. Barriopedro, and S. Fueglistaler (2014), Tropical response to strato- spheric sudden warmings and its modulation by the QBO, J. Geo- phys. Res. Atmos., 119, 7382–7395, doi:10.1002/2013JD020560.

Hansen, F., Matthes, K., Petrick, C., and Wang, W. (2014). The influence of nat- ural and anthropogenic factors on Major Stratospheric Sudden Warmings. Journal of Geophysical Research: Atmospheres, n/a–n/a. doi:10.1002/2013JD021397

Holton, J. R., Haynes, P. H., McIntyre, M. E., Douglass, A. R., Rood, R. B., and Pfister, L. (1995). Stratospheretroposphere exchange. Reviews of geophysics, 33(4), 403-439.

Hu, J. G., R. C. Ren, Y. Y. Yu, and X. HaiMing (2014), The boreal spring stratospheric final warming and its interannual and interdecadal variability, Sci. China Earth Sci., 57, 710–718, doi:10.1007/s11430-013-4699-x.

Kim, J., Son, S. W., Gerber, E. P., and Park, H. S. (2017). Defining sudden stratospheric warming in climate models: Accounting for biases in model climatologies. Journal of Climate, 30(14), 5529–5546. doi:10.1175/JCLI-D-16-0465.1

Kodera, K. (2006). Influence of stratospheric sudden warming on the equatorial troposphere. Geophysical Research Letters, 33(6), 1–4. doi:10.1029/2005GL024510

Limpasuvan, V., Thompson, D. W. J., and Hartmann, D. L. (2004). The Life Cycle of the Northern Hemisphere Sudden Stratospheric Warmings. Journal of Climate, 17(13), 2584–2596. doi:10.1175/1520-0442(2004)017<2584:TLCOTN>2.0.CO;2

Marsh, D. R., Mills, M. J., Kinnison, D. E., Lamarque, J.-F., Calvo, N., and Polvani, L. M. (2013). Climate Change from 1850 to 2005 Simulated in CESM1(WACCM). Journal of Climate, 26 (19), 7372–7391. doi:10.1175/JCLI-D-12-00558.1

Matsuno, T. (1971), A dynamical model of the stratospheric sudden warming, J. Atmos. Sci., 28, 1479–1494.

Matthes, K., Marsh, D. R., Garcia, R. R., Kinnison, D. E., Sassi, F., and Walters, S. (2010). Role of the QBO in modulating the influence of the 11 year solar cycle on the atmosphere using constant forcings. Journal

of Geophysical Research, 115(D18), D18110. doi:10.1029/2009JD013020

Mclandress, C., and Shepherd, T. G. (2009). Impact of climate change on stratospheric sudden warmings as simulated by the Canadian Middle Atmosphere model. Journal of Climate, 22(20), 5449–5463. doi:10.1175/2009JCLI3069.1

Monge-Sanz, B.M., M.P. Chipperfield, A. Untch, J.-J. Morcrette, A. Rap, and A.J. Simmons (2013). On the uses of a new linear scheme for stratospheric methane in global models: Water source, transport tracer and radiative forcing, Atmos. Chem. Phys., 13, 9641-9660, doi: 10.5194/acp-13-9641-2013

Palmeiro, F. M., Barriopedro, D., García-Herrera, R., and Calvo, N. (2015). Comparing Sudden Stratospheric Warming Definitions in Reanalysis Data. Journal of Climate, 150709110342004. doi:10.1175/JCLI-D-15-0004.1

——, F. M., Calvo, N., and Garcia, R. R. (2014). Future Changes in the Brewer–Dobson Circulation under Different Greenhouse Gas Concentrations in WACCM4. Journal of the Atmospheric Sciences, 71(8), 2962–2975. doi:10.1175/JAS-D-13-0289.1

Plumb, R. A.(2002). Stratospheric Transport . J. Meteorol. Soc. Japan, 80, 793–809.

Polvani, L. M., and Waugh, D. W. (2004). Upward Wave Activity Flux as a Precursor to Extreme Stratospheric Events and Subsequent Anomalous Surface Weather Regimes. Journal of Climate, 17 (18), 3548–3554. doi:10.1175/1520-0442(2004)017<3548:UWAFAA>2.0.CO;2

Randel, William J., Rolando R. Garcia, F. W. (2002). Time-Dependent Upwelling in the Tropical Lower Stratosphere Estimated from the Zonal-Mean Momentum Budget, 2141–2152.

Tilmes, S., Garcia, R. R., Kinnison, D. E., Gettelman, A., and Rasch, P. J. (2009). Impact of geoengineered aerosols on the troposphere and stratosphere. Journal of Geophysical Research, 114(D12), D12305. doi:10.1029/2008JD011420

Van Vuuren, D. P., Edmonds, J., Kainuma, M., Riahi, K., Thomson, A., Hibbard, K., ... and Masui, T. (2011). The representative concentration pathways: an overview. Climatic change, 109(1-2), 5.

Chapter 6

Future changes in the Brewer-Dobson circulation under different greenhouse gas concentrations in WACCM4

Future Changes in the Brewer–Dobson Circulation under Different Greenhouse Gas Concentrations in WACCM4

Froila M. Palmeiro and Natalia Calvo

Departamento de Física de la Tierra II, Universidad Complutense de Madrid, Madrid, Spain

Rolando R. Garcia

Atmospheric Chemistry Division, NCAR,* Boulder, Colorado

ABSTRACT

The climatology and future changes of the Brewer–Dobson circulation (BDC) in three climate change scenarios are studied using the latest version of the Whole Atmosphere Community Climate Model (WACCM4), which is fully coupled to an ocean model. The results show an acceleration in both the shallow and deep branches of circulation in response to increasing greenhouse gases (GHGs) together with an upward displacement of the tropical upwelling in the deep branch near the stratopause. The downward control principle reveals that different waves are involved in forcing the acceleration of the upper and lower branches. Climatological-mean tropical upwelling in both the lower and upper stratosphere is dominated by explicitly resolved, planetary-scale waves. Trends in the tropical upwelling in the lower stratosphere are mainly attributed to explicitly resolved, planetary-scale waves. However, in the upper stratosphere, despite the fact that resolved waves control the forcing of the climatological upwelling, their contribution to the long-term trend diminishes with increasing GHGs, while the role of gravity waves associated with fronts increases and becomes dominant in the model scenario with the largest GHG increases. The intensification and upward displacement of the subtropical tropospheric jets due to climate change leads to filtering of the westerly part of the frontal gravity wave spectrum, leaving the easterly components to reach the upper stratosphere and force the changes in the circulation there.

1. Introduction

The stratospheric meridional overturning circulation, also known as the Brewer–Dobson circulation (BDC), is responsible for mean mass transport of chemical tracers from the equator to the poles (Birner and Bönisch 2011). Several modeling studies have shown an acceleration of the BDC with increasing greenhouse gas (GHG) concentrations (e.g., Butchart et al. 2006), which led to growing interest in this circulation. Changes in the BDC can modify the distribution of ozone and other chemical compounds, resulting not only in a dynamical alteration

of the stratosphere and stratosphere–troposphere interactions but also to changes in the tropospheric radiative balance.

Recent studies have clearly differentiated two branches of the stratospheric mean meridional circulation: a shallow branch, located in the lowermost stratosphere, with upwelling in the tropics and downwelling in the subtropics and middle latitudes, and a deep branch with maximum upwelling in the tropical upper stratosphere and downwelling in the middle and high latitudes throughout the entire height of the stratosphere. Birner and Bönisch (2011) distinguish between shallow and deep branches on the basis of the stratospheric transit times in each branch, with the result that the shallow branch extends to about 50 hPa and the deep branch is located above that altitude. Here we follow Birner and Bönisch and adopt 50 hPa as the approximate level separating shallow and deep branches.

Recently, Lin and Fu (2013) looked at the climatology and changes in all branches of the BDC using

---

Corresponding author address: Froila Palmeiro, Universidad Complutense de Madrid, Dpto. de Física de la Tierra, Astronomía y Astrofísica II, Plaza Ciencias, s/n Madrid, Madrid 28040, Spain.
E-mail: froipalm@ucm.es

chemistry–climate models from the second Chemistry–Climate Model Validation (CCMVal2) activity. These authors define a transition layer between 100 and 70 hPa, with the shallow branch extending up to 30 hPa, and the deep branch beginning above 30 hPa. They found a larger acceleration in the shallow branch than in the deep branch. Similarly, Hardiman et al. (2014) investigated future changes in the Brewer–Dobson circulation in the entire stratosphere in high-top phase 5 of the Coupled Model Intercomparison Project (CMIP5) models (with model lids above 1 hPa). They found differences in the width of the changes in tropical upwelling above and below 20 hPa. These differences suggest that different dynamical behaviors may be related to different driving mechanisms.

The stratospheric mean meridional circulation is driven by wave dissipation (Holton et al. 1995). The downward control principle (DCP; Haynes et al. 1991) makes it possible to identify quantitatively the waves that are responsible for driving this circulation. This principle establishes that, in steady state, the mean vertical velocity at any vertical level is controlled only by the density-weighted integral of the wave forcing acting above that level. Different studies using both reanalysis and general circulation models suggest that the BDC in the lower stratosphere is mainly forced by large-scale waves [e.g., Fig. 4.10 of Eyring et al. (2010)], although there is considerable intermodel variability. In particular, in CCMVal2 models, more than 70% of the climatological tropical upwelling at 70 hPa was due to waves that are explicitly resolved by the models, 21.1% to parameterized (unresolved) orographic gravity wave drag, and 7.1% to parameterized nonorographic gravity wave drag (Butchart et al. 2011). These percentages agree well with results from the 1989–2009 Interim European Centre for Medium-Range Weather Forecasts (ECMWF) Re-Analysis (ERA-Interim), although in the latter only 4% of the tropical upwelling at 70 hPa was attributed to parameterized wave drag (nonorographic gravity waves are not included in ERA-Interim; Seviour et al. 2012).

Regarding changes in tropical upwelling associated with increasing greenhouse gases, there is a general consensus that changes in resolved wave drag are the main driver of the acceleration in the lower stratosphere [e.g., Fig. 4.11 of Eyring et al. (2010)]. The multimodel analysis of Butchart et al. (2010) revealed contributions at 70 hPa of up to 67% from these waves and 30% from orographic gravity waves. These results agree with other individual model studies, such as those by Garcia and Randel (2008; hereafter GR08), McLandress and Shepherd (2009), Garny et al. (2011), and Shepherd and McLandress (2011). GR08 pointed out that, as the subtropical tropospheric jets intensify in response to tropospheric warming driven by GHG, the contribution of gravity waves increases above 70 hPa in the middle stratosphere. This altitude dependence of the different wave contributions to the upwelling highlights the importance of analyzing the two branches of the circulation separately.

Several studies have attempted to determine whether changes in wave forcing that drive changes in the circulation are due to differences in wave transmission or in wave excitation. In particular, Calvo and Garcia (2009) found that changes in the transmission of explicitly resolved waves were the main mechanism in simulations of the last half of the twentieth century. This was in contrast with simulations of the twenty-first century, where changes in the excitation of resolved waves, related to anomalous convection, dominated over changes in wave transmission. Olsen et al. (2007) showed changes in tropospheric wave propagation due to warmer sea surface temperatures (SSTs) in the tropics. Furthermore, Deckert and Dameris (2008) demonstrated that higher tropical SSTs enhance tropical deep convection, amplifying the generation of tropical waves, as well as poleward-propagating waves that can intensify the BDC in the extratropics. Finally, Garny et al. (2011) showed that both wave propagation and wave generation are affected by increasing SSTs as a result of climate change and, thus, both mechanisms can generate changes in the BDC. In particular, Shepherd and McLandress (2011) found that changes in wave drag in their model were largely explained in terms of changes in the location of the critical layers within the subtropical lower stratosphere.

The fact that SSTs represent an important atmosphere–ocean feedback and that its explicit simulation in climate models is complex has been noted in many previous studies (e.g., Braesicke and Pyle 2004; Kosaka and Xie 2013). Up to now, most studies that investigated changes in the BDC with general circulation models that include a well-resolved middle atmosphere used prescribed SSTs from observations for past simulations or SSTs from low-top atmosphere–ocean models to understand future changes associated with GHGs. This lack of interactive atmosphere–ocean feedbacks adds uncertainty to the understanding of the mechanisms involved in the BDC changes. In the present study, we use a fully coupled atmosphere–ocean climate model with its top in the thermosphere to analyze the BDC and its forcing in the entire stratosphere. Special attention is paid to the less-investigated deep branch of the circulation and to future changes under different climate change scenarios.

This paper is organized as follows: Section 2 presents the model and simulations used here together with the methodology. Results concerning the BDC climatology are shown in section 3, while section 4 presents future trends in the circulation. Section 5 summarizes the main results.

2. Simulations and method

The latest version of the Whole Atmosphere Community Climate Model (WACCM4) is part of the Community Earth System Model, version 1 (CESM1), developed by the U.S. National Center for Atmospheric Research (NCAR). This improved version of WACCM integrates a four-component coupled system, including atmosphere, ocean, land, and sea ice models. The ocean and sea ice components are described in Holland et al. (2012) and Danabasoglu et al. (2012). The atmospheric component, which includes fully coupled chemistry, has a longitude–latitude resolution of $2.5° \times 1.9°$ and 66 vertical levels up to about 140 km. The vertical resolution is finer than 1.5 km in the first 25 km, with a gradual increase up to 2 km at the stratopause, 3.5 km in the mesosphere, and half of the local scale height beyond the mesopause. The model includes heating from volcanic aerosols (Tilmes et al. 2009), solar variability is specified from the model of Lean et al. (2005), and a quasi-biennial oscillation is imposed by relaxing the winds to observations in the tropics (Matthes et al. 2010). The parameterization of orographic gravity waves is related to surface roughness, and nonorographic gravity waves are parameterized based on the diagnosis of frontogenesis and the occurrence of deep convection in the model. These parameterizations are described in detail by Richter et al. (2010). Additional information about the model can be found in Marsh et al. (2013).

Three historical runs were performed from 1960 to 2005, each with slightly different initial conditions, and observed concentrations of GHGs at the surface. Three future simulations from 2005 to 2100 were run based on the representative concentration pathways (RCPs) adopted by the Intergovernmental Panel on Climate Change (IPCC) for its Fifth Assessment Report. RCP2.6 is the most optimistic scenario and prescribes a decrease in CO_2 starting in 2050, reaching 400 ppmv in 2100. In RCP4.5, the CO_2 concentration increases from 400 ppmv to slightly less than 550 ppmv in 2100. The RCP8.5 simulation represents a CO_2 doubling from 2005 to 2080, reaching values of 950 ppmv in 2100. Mixing ratios of ozone depleting substances (ODS) in terms of equivalent effective stratospheric chlorine (EESC) decrease from maximum values of approximately 4 ppbv in 2005 to approximately 1.7 ppbv in 2100.

To characterize the mean meridional circulation of the stratosphere, we examine the vertical component of the transformed Eulerian-mean (TEM) residual circulation $\overline{w}^*$ (Andrews et al. 1987). We will refer to upwelling when $\overline{w}^*$ is positive and to downwelling when $\overline{w}^*$ is negative. Possible changes in the future are assessed by calculating linear trends derived from deseasonalized monthly-mean time series. The significance of trends at the 95% confidence level is evaluated using a Monte Carlo test. Differences between climatological values from the first and last 20 years of the simulation are also shown, as needed. Significant differences are assessed at the 95% confidence level by a Student's t test.

3. Climatology of the BDC in WACCM4

a. Circulation

Figure 1a shows the latitude–altitude cross section of the annual-mean $\overline{w}^*$ for the ensemble mean of the three historical simulations (1960–2005). This figure clearly distinguishes the two different circulation branches discussed in the introduction. The shallow branch, in the lower stratosphere, is principally responsible for troposphere–stratosphere mass exchange and consists of two cells with rising motion in the tropics and sinking in the subtropics and middle latitudes (Holton 1990). Tropical upwelling in the shallow branch is stronger in December–February (DJF) than in June–August (JJA). In the deep branch, the largest tropical upwelling occurs in the upper stratosphere around 45–50 km. The associated downwelling extends from midlatitudes to the poles, reaching a maximum at polar latitudes in the upper stratosphere and extending down toward the polar troposphere. Similar to the shallow branch, the deep branch is equatorially centered when the annual average is computed. However, the seasonal averages show an intensification of the winter cell and a shift of the tropical upwelling toward the summer hemisphere, also stronger in DJF (Seviour et al. 2012). The deep branch cell in the summer hemisphere is very weak below 40 km, in contrast with the behavior of the shallow branch (Figs. 1b,c). Note that the summer to winter hemisphere branch of the TEM circulation starts above 65–70 km in WACCM4, beyond the upper boundary of the figures shown here.

A different look into the climatological seasonal behavior of the BDC is presented in Fig. 2. It shows the latitudinal distribution of the ensemble-mean, annual-mean $\overline{w}^*$ as a function of time and latitude at 1 hPa (Fig. 2a) and 100 hPa (Fig. 2b). These are the levels where the tropical upwelling in WACCM4 is largest in the deep and shallow branches, respectively (Fig. 1a). The seasonal behavior of $\overline{w}^*$ is similar in both the lower and the upper stratosphere, although the seasonal cycle is much more pronounced in the upper stratosphere (Fig. 2a). Thus, at 1 hPa the upwelling can comprise the entire winter hemisphere while downwelling occurs in the summer hemisphere from about 15° latitude to the pole. The magnitude of the tropical upwelling is very similar throughout the year, slightly larger in boreal
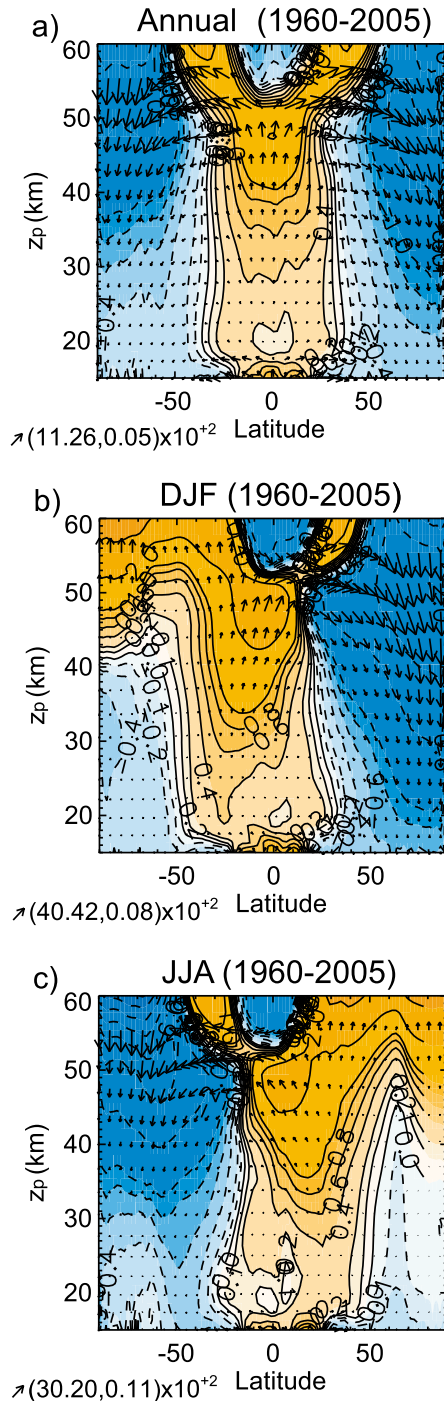
a)

Annual (1960–2005)

↗(11.26,0.05)×10^{+2} Latitude

b)

DJF (1960–2005)

↗(40.42,0.08)×10^{+2} Latitude

c)

JJA (1960–2005)

↗(30.20,0.11)×10^{+2} Latitude

FIG. 1. Climatology of the TEM ($\overline{v}^*$, $\overline{w}^*$) vector circulation (arrows) and magnitude of $\overline{w}^*$ (contours) as functions of latitude and log-pressure altitude z_p for the ensemble mean of three simulations of the historical period 1960–2005. (a) Annual-mean climatology, (b) DJF mean, and (c) JJA mean. For $\overline{w}^*$, variable contours are shown for 0, ±0.1, ±0.2 mm s^{-1}, every 0.2 mm s^{-1} up to ±1 mm s^{-1}, and every 1 mm s^{-1} thereafter. Orange shading and solid lines represent positive values; blue shading and dashed lines represent negative values. The arrows on the lower-left-hand corner of each panel indicate the scale of the vector circulation.
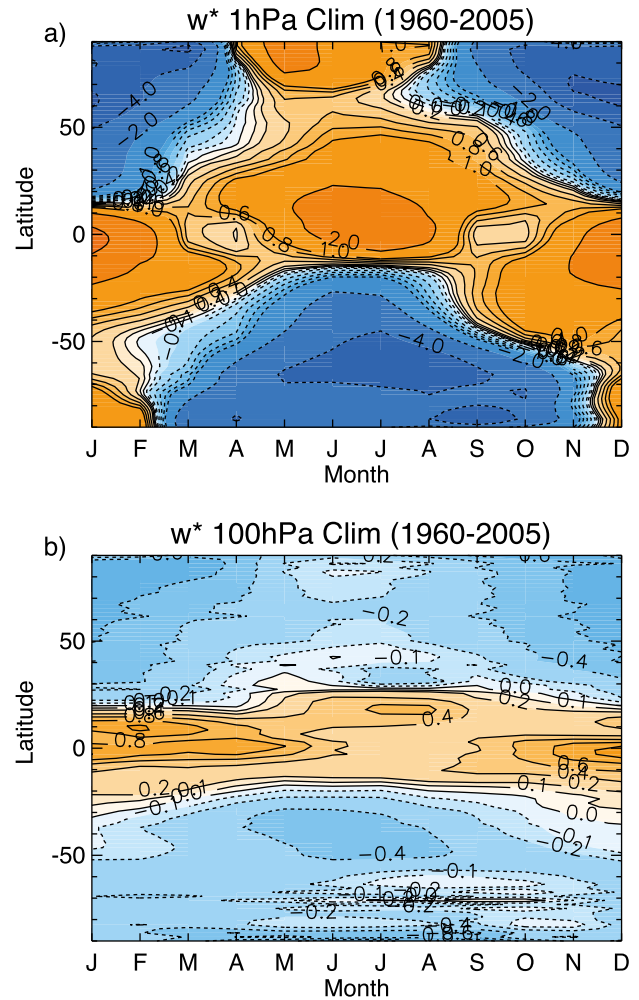
a)

w* 1hPa Clim (1960–2005)

b)

w* 100hPa Clim (1960–2005)

FIG. 2. Ensemble-mean seasonal climatology of $\overline{w}^*$ (1960–2005) at (a) 1 and (b) 100 hPa. Contour intervals are 0.2 mm s^{-1} up to 1 mm s^{-1} and every 1 mm s^{-1} thereafter. Orange shading and solid lines represent positive values; blue shading and dashed lines represent negative values.

winter months. In the Southern Hemisphere (SH), the largest downwelling occurs at middle latitudes and not in the polar region. In the lower stratosphere, upwelling is confined to lower latitudes, maximizing in the summer hemisphere in the subtropics. Downwelling is simulated from the subtropics to the polar latitudes, and it is larger in the winter half of the year. Note, however, that downwelling at polar latitudes in the lower stratosphere comes mainly from the deep branch (e.g., Birner and Bönisch 2011). The seasonal distribution of $\overline{w}^*$ at 100 hPa can be compared with results from the ERA-Interim, as shown by Seviour et al. (2012, their Fig. 4c). Although the period is not exactly the same (1989–2009 for the reanalysis versus 1960–2005 for the model) the agreement is excellent, not only regarding the spatial distribution of the regions of upwelling and downwelling, but also their

magnitude. This good agreement lends confidence to our results and supports the use of WACCM4 to investigate future changes in the BDC.

b. Wave forcing

In WACCM4, the wave drag from resolved and parameterized waves is output separately. Within the

gravity wave parameterization, orographic gravity waves and nonorographic gravity waves of frontal and convective origin are also distinguished. Thus, it is possible to use the DCP to quantify the different contribution of these waves to the tropical upwelling. The DCP estimate of $\overline{w}^*$ averaged between latitudes ϕ_1 and ϕ_2 is given by

$$\langle \overline{w}^*(z) \rangle = \frac{\dfrac{1}{\rho(z)} \left| \int_z^\infty \{\rho a \cos^2\phi [(\rho a \cos\phi)^{-1}\mathbf{\nabla} \cdot F(\phi, z') + X(\phi, z')]/\overline{m}_\phi\} \, dz' \right|_{\phi_1}^{\phi_2}}{|\sin\phi|_{\phi_1}^{\phi_2}}, \tag{1}$$

where ρ is the density, z is log-pressure altitude, $\overline{m} = a\cos\phi(\overline{u} + \Omega a\cos\phi)$ is the zonal-mean angular momentum, Ω is Earth's rate of rotation, and a is the radius of Earth. The terms in the integrand include the Eliassen–Palm flux divergence due to resolved waves, $\mathbf{\nabla} \cdot F$, and the parameterized wave drag X due to orographic gravity waves and gravity waves associated with convective and frontal sources. We average (1) over the turn-around latitudes (i.e., ϕ_1 and ϕ_2 are taken to be the latitudes where $\overline{w}^*$ changes sign on each pressure level; Rosenlof 1995). In what follows, the individual parameterized wave drag components will be denoted by OGWD, CGWD, and FGWD, which stand for orographic, convective, and frontal gravity wave drag, respectively. This methodology is similar to that used in GR08 except that, for each altitude, we evaluate the integrand in (1) between the turn-around latitudes instead of using fixed latitudes as in GR08. Note that, in order for the DCP to be applicable, the turn-around latitudes where the integrand is evaluated need to be approximately parallel to lines of constant angular momentum, and thus (1) is not valid in the deep tropics where lines of constant m form closed contours.

Figure 3 shows $\overline{w}^*$ computed from (1) for the ensemble mean of the three historical simulations. The latitude limits used in the calculation correspond to the annual-mean climatological turn-around latitudes for 1960–2005. These latitude limits are far enough from the equator that application of (1) is justified. The estimated value for $\overline{w}^*$ computed from the DCP (dashed line) and its actual value output from the model (black line) are in very good agreement everywhere except near 48 km, although the difference there is only about 15%. The tropical upwelling clearly shows the two maxima, in the lowermost and upper stratosphere, corresponding to the shallow and deep branches of the circulation. The largest values (about $1 \, \text{mm s}^{-1}$) occur at about 48 km. Throughout the entire stratosphere, resolved waves are the main

driver of the climatological tropical upwelling. In the lower stratosphere, at 70 hPa (~18.6 km), their contribution is about 70% of the total, versus 30% for orographic gravity waves. The contributions of convective gravity waves (CGWs) or frontal gravity waves (FGWs) are negligible in the lower stratosphere. These results are consistent with other modeling studies and reanalysis data (e.g., Butchart et al. 2011; Seviour et al. 2012).

In the upper stratosphere, at about 48 km (where the largest upwelling occurs), most of the upwelling is attributable to resolved waves. In fact, upwelling due to resolved waves is actually larger than the total upwelling near the stratopause because FGWs produce downwelling at this level. Both OGWD and CGWD make a small contribution to upwelling near the stratopause—about 10% of total upwelling. Note that in WACCM4 the contribution of CGWs to the mean tropical upwelling is close to zero throughout the stratosphere. The wave contribution to the climatological-mean tropical upwelling in future scenarios (not shown) is similar to the one shown in Fig. 3 for the recent past.

4. Future trends in the BDC due to increases in GHG

a. Circulation trends

Long-term trends, 2005–2100, in $\overline{w}^*$ for three future scenarios are shown in Fig. 4, with the trend in the vector TEM circulation ($\overline{v}^*$, $\overline{w}^*$) superimposed (arrows). The spatial configuration of the trends can be compared with that of the 1960–2005 climatology shown in Fig. 1a, as the climatologies for the future simulations showed very similar spatial patterns. Figure 4 shows an intensification of both branches of the circulation with increasing GHG concentrations. The intensification is very weak in RCP2.6, where only the change in the upper branch near the stratopause is significant. In RCP4.5, there is a moderate,
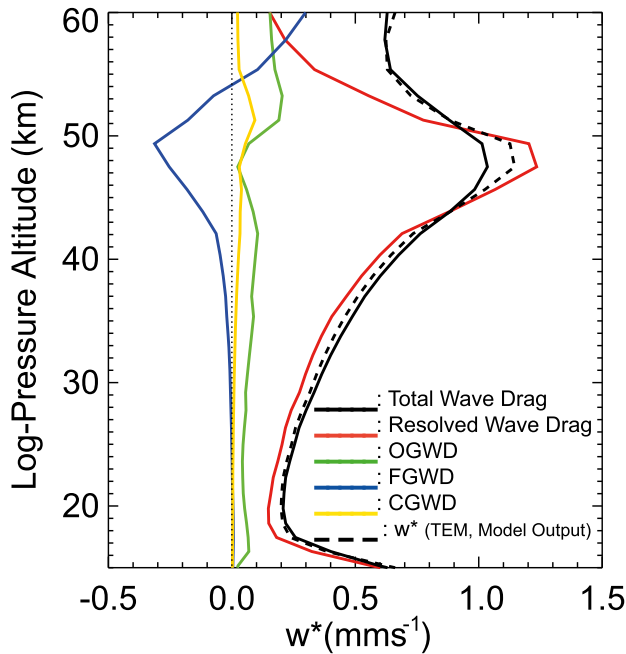
FIG. 3. Tropical average of $\overline{w}^*$ calculated from the DCP, showing the contributions due to different waves in the 1960–2005 ensemble-mean simulation. The black curve includes the total wave drag, the red curve is the resolved wave drag, the blue curve is FGWD, the green curve is OGWD, and the yellow curve is CGWD. The dashed curve is the TEM vertical velocity computed directly from the model output. Similar results hold for all other simulations discussed in this paper.

statistically significant acceleration of the circulation in the regions of maximum upwelling and downwelling in the upper stratosphere and lowermost stratosphere. RCP8.5 shows the largest trends in the TEM circulation, both in the deep and the shallow branches. The upper-stratosphere trend implies an increase in $\overline{w}^*$ over the period of analysis of approximately 50% of the climatological-mean value. Note that the regions of positive upwelling trends in the lower stratosphere and in the vicinity of the stratopause are narrower than the climatological upwelling (1960–2005) at those locations (red lines), indicating that the upwelling becomes more concentrated around the equator. This is in agreement with results (for the lower stratosphere) obtained from an ensemble of several high-top CMIP5 models (Hardiman et al. 2014). A common feature in all our simulations in the SH is the positive trend in $\overline{w}^*$ at high latitudes, implying a deceleration of the climatological downwelling over the southern polar cap (cf. Fig. 1). Comparison of the trends in the RCP4.5 scenario (Fig. 4b) with trends derived from a pair simulations (not shown), where either the mixing ratios of ODS or those of GHG were held constant at 2001 values, revealed that the deceleration of downwelling over the southern polar cap is related to ozone recovery. This has also been pointed out in
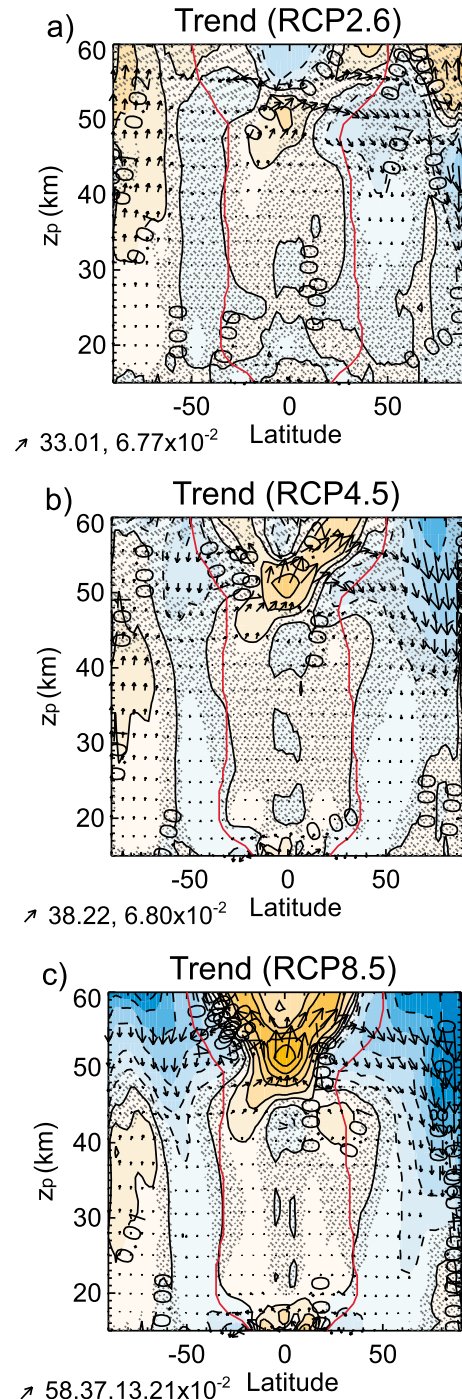
FIG. 4. Trends in the TEM ($\overline{v}^*$, $\overline{w}^*$) vector circulation (arrows) and $\overline{w}^*$ (contours) as functions of latitude and z_p over the period 2005–2100 for (a) RCP2.6, (b) RCP4.5, and (c) RCP8.5. Contours are 0, ± 0.01, ± 0.02 mm s^{-1} decade^{-1}, and every ± 0.02 mm s^{-1} decade^{-1} thereafter. Stippling indicates where trends in $\overline{w}^*$ are not significant at the 2σ level. Orange shading and solid lines represent positive values; blue shading and dashed lines represent negative values. Red lines indicate the climatological (1960–2005) turn-around latitudes. The arrow on the lower-left-hand corner of each panel indicates the scale of the vector trend.

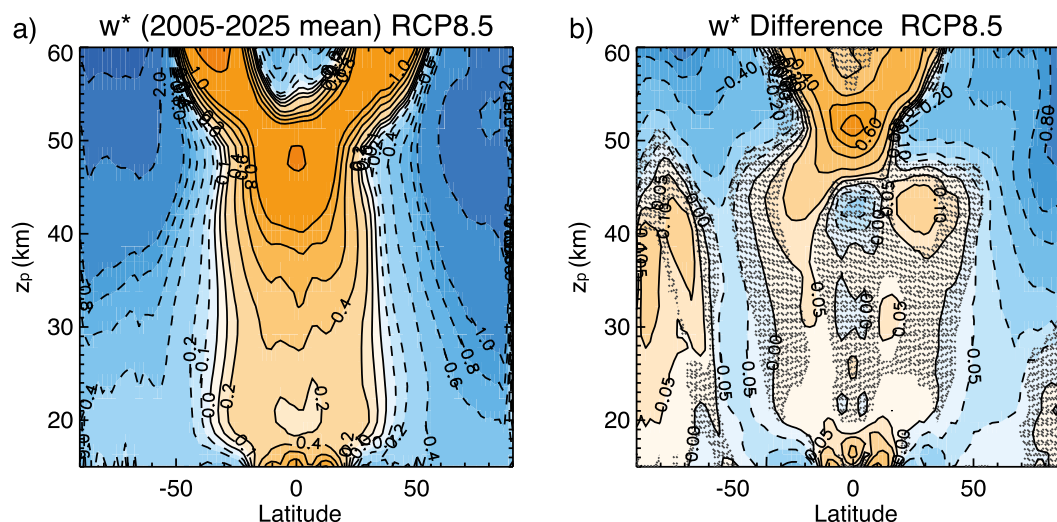FIG. 5. (a) $\overline{w}^*$ averaged over the first 20 years of the RCP8.5 simulation (2005–25); contour interval is 0.5 mm s^{-1}. (b) Difference in $\overline{w}^*$ averaged over 2080–99 minus 2005–25. Variable contours are 0, ±0.05, ±0.1, ±0.2 mm s^{-1}, and every 0.2 mm s^{-1} thereafter. Stippling indicates where trends in $\overline{w}^*$ are not significant at the 2σ level according to a Student's t test. Orange shading and solid lines represent positive values; blue shading and dashed lines represent negative values.

other, recent studies (e.g., McLandress and Shepherd 2009).

In addition to the intensification of the BDC shown in Fig. 4, the largest trends in tropical upwelling in the upper stratosphere indicate an upward displacement of the region of upwelling with increasing GHG concentrations. Thus, for simulation RCP2.6, the maximum trend in upwelling is centered near 48 km, while for RCP8.5, it occurs near 52 km. To analyze this behavior in more detail, differences between the averages of the last and the first 20 years of the simulations were computed. The results are shown in Fig. 5 for RCP8.5, which is the scenario with the largest changes. Significant differences at the 95% level were computed with a Student's t test. The difference pattern (Fig. 5b) in the upper stratosphere is centered at a higher altitude than the climatological upwelling. This upward displacement is larger in RCP8.5 than in RCP4.5, and it is not present in the RCP2.6 simulation (not shown), which indicates that certain changes only occur for the larger increases in GHGs concentrations. The behavior illustrated in Fig. 5 may be understood as an upward expansion of the deep branch tropical upwelling.

b. Trends in wave forcing

To investigate the contribution of the different waves to changes in the BDC, the latitude–altitude distribution of forcing is first examined. Figure 6 depicts the latitude–altitude cross sections of the climatologies and trends in the four types of wave forcing studied here [Eliassen–Palm (EP) flux divergence of resolved waves, OGWD,

FGWD, and CGWD]. Results are shown for the RCP8.5 climate change scenario since it produces the largest changes. In the lowermost stratosphere, significant negative trends in EP flux divergence appear in the subtropics (Fig. 6b). These represent an intensification and upward extension of the climatological wave dissipation in this region (Fig. 6a). Significant trends in orographic wave forcing also appear in the lower stratosphere between 30° and 40°N, intensifying the climatological drag between 20 and 25 km and weakening it below 20 km (Figs. 6c,d). Nonorographic gravity waves do not dissipate in the lower stratosphere, in agreement with results from the DCP, which showed no contribution from FGWs and CGWs to the climatological tropical upwelling in this region. In addition, no changes in FWGD or CGWD were found in the future simulation in this region.

Significant trends in EP flux divergence are also found in the upper stratosphere. Significant negative trends enhance the climatological wave dissipation in the high latitudes of the NH and shift upward that one in the subtropics and midlatitudes of the SH, above 50 km. At lower altitudes, between 40 and 50 km, there are positive trends in EP flux divergence that weaken the climatological wave dissipation therein. Taken together, the trend patterns above and below 50 km may be interpreted as an upward shift in the region of the largest EP flux divergence with respect to climatology. There is also a significant positive trend in the SH at high latitudes, probably related to ozone recovery, as the abundance of ozone over Antarctica impacts resolved wave propagation (Li et al. 2008). Here, this is manifested as a positive
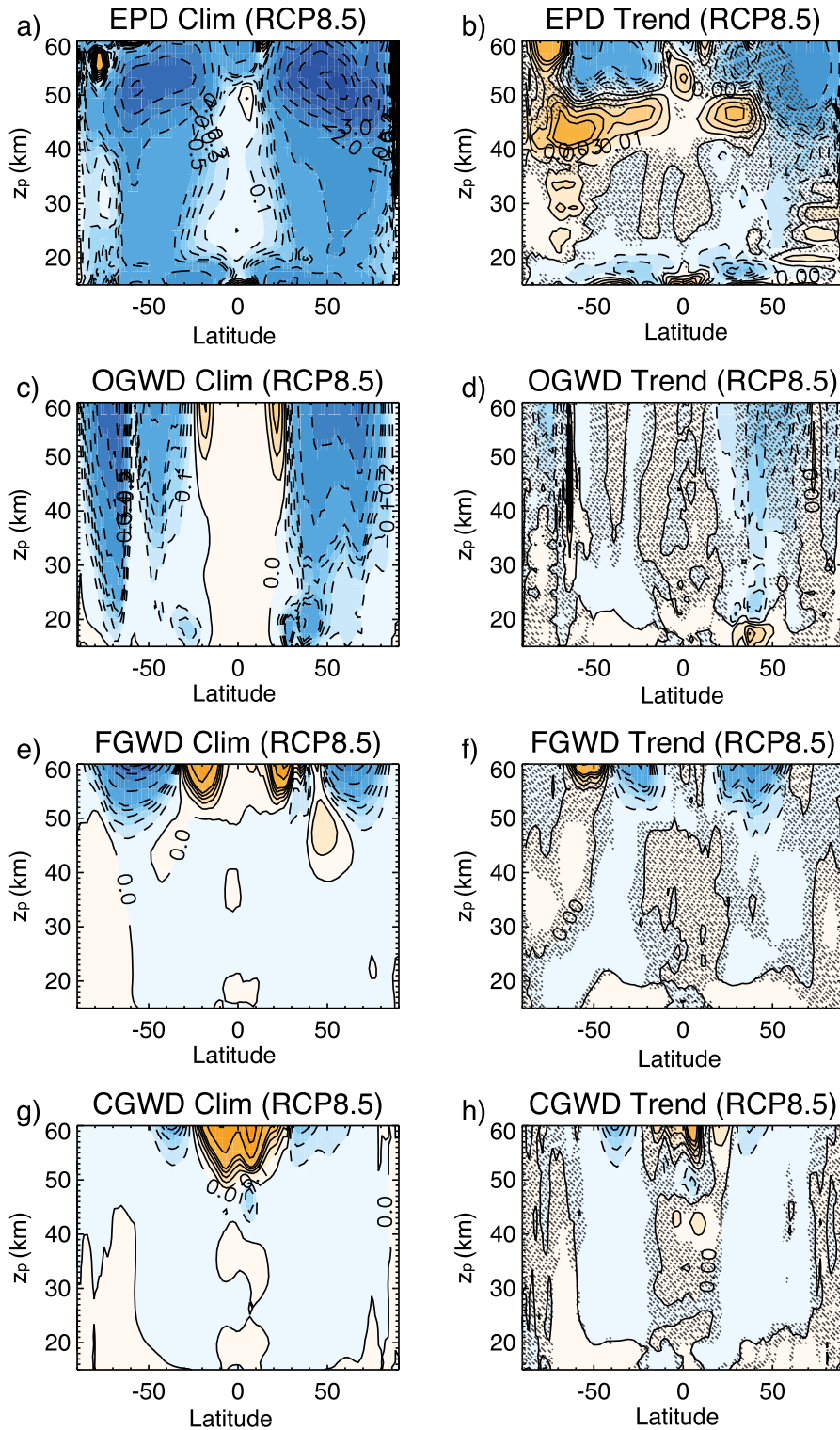
FIG. 6. (left) RCP8.5 climatological annual means and (right) trends per decade for (a),(b) EP flux divergence, (c),(d) OGWD, (e),(f) FGWD, and (g),(h) CGWD. In the left panels, contours are every $\pm 0.1\,\mathrm{m\,s}^{-1}\,\mathrm{day}^{-1}$ up to $\pm 0.5\,\mathrm{m\,s}^{-1}\,\mathrm{day}^{-1}$ and then every $\pm 1\,\mathrm{m\,s}^{-1}\,\mathrm{day}^{-1}$. In the right panels, contours are every $\pm 0.01\,\mathrm{m\,s}^{-1}\,\mathrm{day}^{-1}\,\mathrm{decade}^{-1}$ up to $\pm 0.05\,\mathrm{m\,s}^{-1}\,\mathrm{day}^{-1}\,\mathrm{decade}^{-1}$ and then every $\pm 0.1\,\mathrm{m\,s}^{-1}\,\mathrm{day}^{-1}\,\mathrm{decade}^{-1}$. Orange shading and solid lines represent positive values; blue shading and dashed lines represent negative values. Stippling indicates where trends are not significant at the 2σ level.

FIG. 7. Trends in $\overline{w}^*$ due to different waves between the turn-around latitudes of the climatological ensemble mean (1960–2005) for (a) RCP4.5 and (b) RCP8.5. Color lines are as in Fig. 3. Shadowing indicates the 2σ confidence limits.
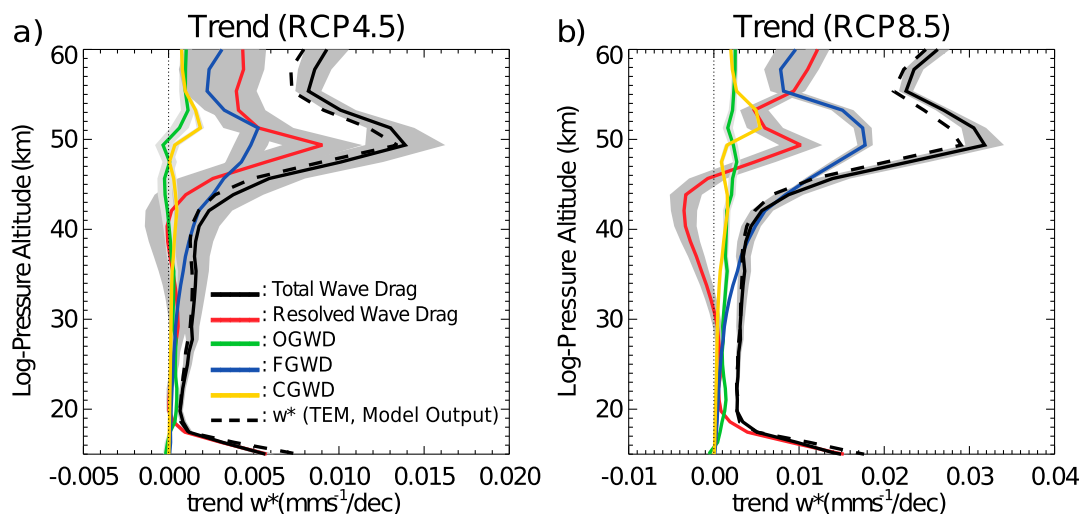
EP flux divergence trend associated with a decrease in wave dissipation in the southern polar latitudes.

Significant negative trends in OGWD are simulated in the subtropical upper stratosphere of the NH, enhancing the climatological wave-induced acceleration. Significant negative (easterly) trends in FGWD are simulated in the subtropics and NH midlatitudes (Fig. 6f). They indicate a decrease of the climatological westerly FGWD in the subtropics and an enhancement of the climatological easterly component in the NH midlatitudes (Fig. 6e). These changes occur mainly during winter in each hemisphere, as explained below. The CGWD is the result of dissipation of gravity waves excited by deep convection in the tropics. These waves dissipate at much higher altitudes (mainly above 50 km; Fig. 6g) and, accordingly, they were not found to drive the climatological tropical upwelling in the stratosphere (Fig. 3). In terms of trends, weaker trends than in the case of FGWD are observed above 50 km in the tropical and subtropical regions, although they intensify during JJA (not shown).

To quantify the contribution of each of these waves to the trends in the climatological tropical upwelling, the DCP has been applied to the RCP4.5 and RCP8.5 simulations (Fig. 7) in a similar way as it was applied to the historical climatology. That is, we have applied (1) to each RCP scenario between the climatological annual-mean turn-around latitudes of the historical ensemble (1960–2005). No results are shown for RCP2.6 since no significant trends in $\overline{w}^*$ were found in the tropical region in this case (Fig. 4a).

In the lower stratosphere, the net trends in tropical-mean upwelling in RCP4.5 and RCP8.5 seen in Fig. 7 are consistent with the results shown in Fig. 4. Trends in

resolved wave drag and in OGWD are the only important driver of the enhanced upwelling of the shallow branch up to about 18 km (~70 hPa); above this level, orographic gravity waves (OGWs) play a nonnegligible role. In the lower stratosphere, the relative contribution of the different waves to the total trend is similar in both RCP scenarios, although the magnitude of the trends is larger in RCP8.5. Our results in this region are consistent with those obtained by GR08, who applied the DCP between fixed latitudes in a previous version of WACCM. In the upper stratosphere, RCP4.5 and RCP8.5 show significant trends in $\overline{w}^*$ centered above 50 km (~1 hPa), above the location of maximum climatological $\overline{w}^*$ (Fig. 1a), in agreement with the upward extension of the circulation pointed out above. Interestingly, the contribution of FGWs to the trend in $\overline{w}^*$ increases dramatically from RCP4.5 to RCP8.5 compared to the increase driven by resolved EP flux divergence. Thus, while in RCP4.5, 36% of the total upwelling trend near 50 km is attributed to FGWs (and 64% to resolved waves), in RCP8.5 the FGW contribution increases up to 56% versus 30% for resolved waves, such that changes in FGW driving become the largest contributor to the trend in tropical upwelling in the upper stratosphere in the scenario with the largest increase in GHGs.

We have also applied the DCP in simulation RCP8.5 between the climatological turn-around latitudes and the pole in each hemisphere (Figs. 8a,b)—that is, over the latitude ranges where there is climatological downwelling. We note, however, that in these regions the trends in vertical velocity are not uniformly negative. This is particularly true of the SH, where poleward of 65°S the trend in vertical velocity is actually positive below about 45 km
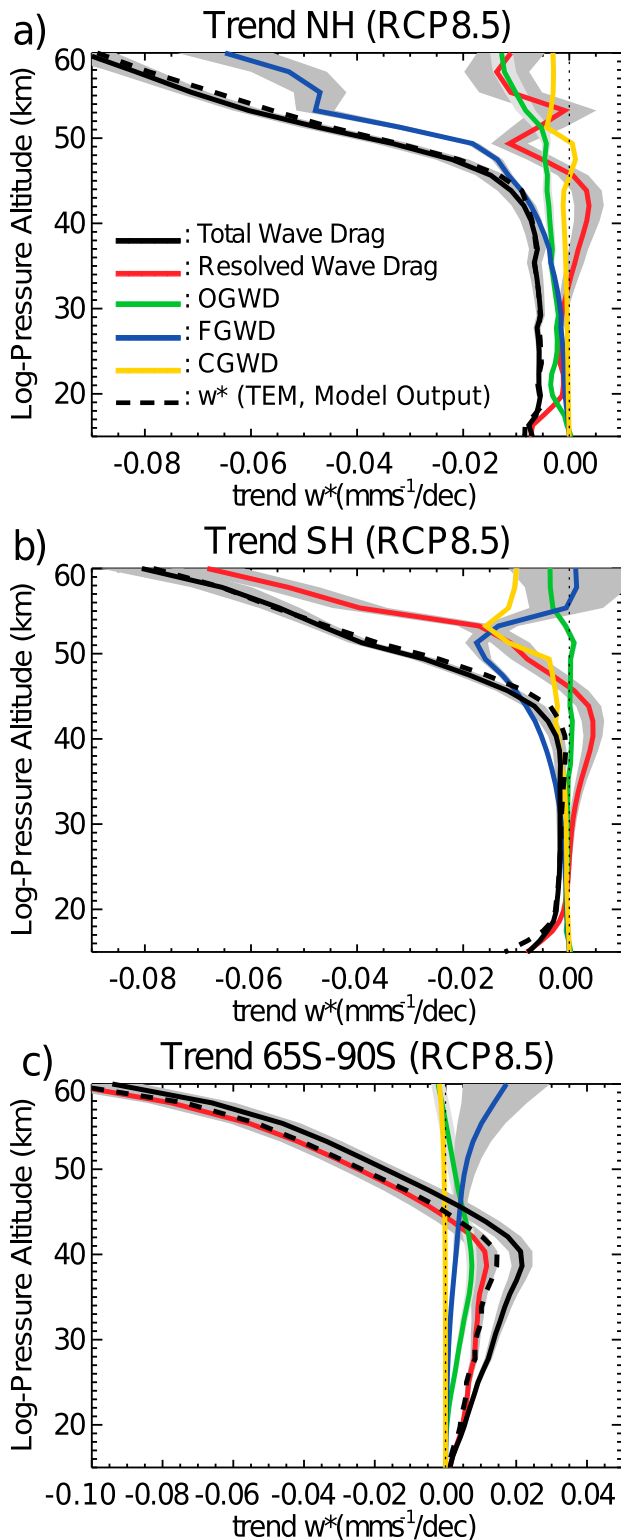
105

FIG. 8. Trends in $\overline{w}^*$ attributable to different waves for simulation RCP8.5: (a) in the Northern Hemisphere, between the northern turn-around latitude and the North Pole; (b) in the Southern Hemisphere, between the southern turn-around latitude and the South Pole; and (c) between 65°S and the South Pole. Line colors are as in Fig. 3. Shadowing indicates the 2σ confidence limits.

(cf. Fig. 4). In the NH (Fig. 8a), the mean downwelling trend between the northern turn-around latitude and the pole in the lower stratosphere is attributed to resolved waves and OGW; at 18 km, the percentages are 70% and 30%, respectively. In the upper stratosphere, 50% of the trend is attributed to FGWs while the other 50% is due to OGWs and resolved waves; above 50 km, the contribution of FGWs is dominant. CGWs contribute negligibly to the intensification of downwelling in the NH, as near zero trends were found everywhere.

In the SH, Fig. 8b shows that in the lower stratosphere, almost 100% of the downwelling trend is due to resolved waves. However, above 45 km, where the downwelling trend extends to polar latitudes, FGW, CGW, and resolved wave contributions increase reaching similar magnitudes at 53 km. Above this altitude, resolved waves become again the principal contributor. OGW were found to contribute negligibly to the SH downwelling trends. Finally, in order to determine the cause of the positive trend in vertical velocity over the southern polar cap at altitudes below 45 km (implying a weaker downwelling), we have applied the DCP between 65°S and the South Pole (Fig. 8c). The results show that resolved waves and OGW are responsible for this positive trend over the southern polar cap, with negligible contributions from other waves. This result is consistent with the pattern of trends shown for the EP flux divergence (Fig. 6b), which shows a decrease in resolved wave forcing below 50 km at high southern latitudes.

Changes in tropical upwelling are forced by changes in wave dissipation, which in turn are modulated by changes in the background winds. To understand the mechanisms that drive the changes in wave forcing with increasing GHGs, Fig. 9 shows the climatology (contours) and the trends (colors) of the zonal-mean zonal wind for the three RCP scenarios. There is a direct relationship between the intensification and upward shift of the subtropical jets and the increasing load of GHGs. The largest trends are present in the extreme scenario, RCP8.5 (Fig. 9c), consistent with the largest trends in meridional temperature gradient (not shown). In agreement with GR08 and Shepherd and McLandress (2011), the intensification of the subtropical jets enhances wave propagation and dissipation in the subtropical stratosphere (Fig. 7b). The negative trends in the SH present in all the RCP simulations reflect the impact of ozone recovery.

Changes in the zonal-mean zonal wind can affect the propagation and dissipation of gravity waves. We show here how these changes affect FGWs, which are the main contributor to the changes in tropical upwelling found in the upper stratosphere in the RCP8.5 simulation (see Fig. 6f). Figures 10a and 10b show vertical profiles of the climatological FGW eddy momentum flux associated
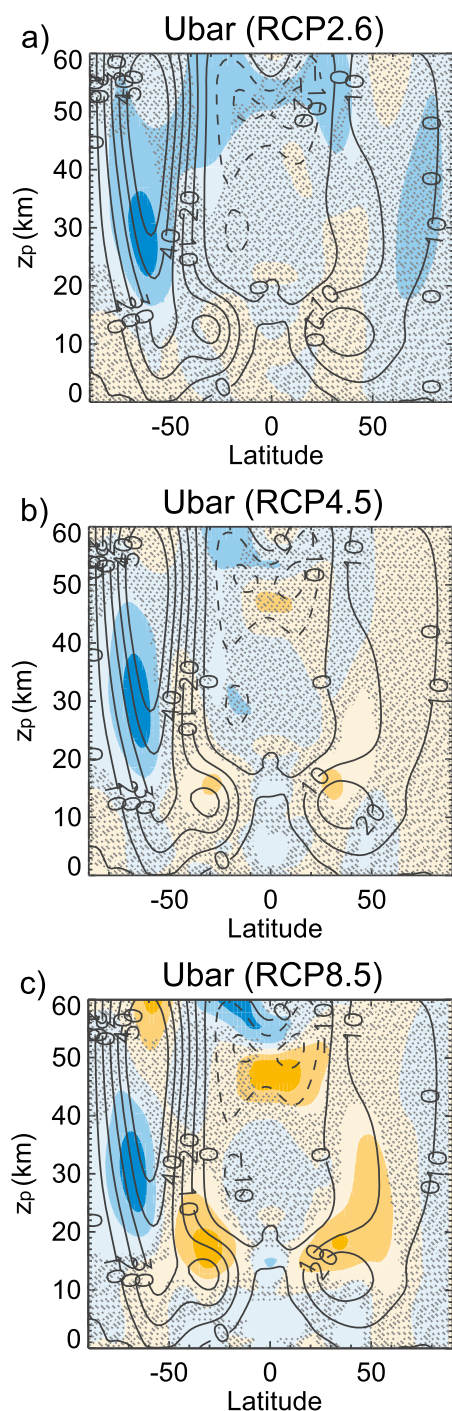
FIG. 9. Trends (shaded) and climatology (black contours) of the zonal-mean zonal wind for three RCP scenarios: (a) RCP2.6, (b) RCP4.5, and (c) RCP8.5. Contour interval for the trend is $\pm 0.2\,\mathrm{m\,s^{-1}\,decade^{-1}}$; for the climatology, the interval is $\pm 10\,\mathrm{m\,s^{-1}}$. Orange shading and solid lines represent positive values; blue shading and dashed lines represent negative values. Stippling indicates where trends are not significant at the 2σ level. Note that the altitude range starts from the surface in these plots.

with waves of easterly (red) and westerly (blue) phase velocity, together with the zonal-mean zonal wind (black) at 20°N and 20°S. These are approximately the latitude limits for the maximum trend in the deep branch upwelling, near the stratopause. The net FGW momentum flux (green curve) is zero at the source but quickly becomes positive below 20 km owing to the filtering of westerly components of the spectrum by the climatological subtropical jet (black curve). Above 20 km, where the climatological zonal-mean zonal wind turns negative, easterly components of the spectrum are attenuated sharply, and the net FGW momentum flux becomes negative. The negative net flux decreases above 50 km, giving rise to the climatological positive wave drag seen in Fig. 6e.

Trends in FGW momentum flux are shown in Figs. 10c and 10d. At the source of the waves, near 5 km, both westerly and easterly components of the spectrum become weaker with respect to climatology; that is, the tendencies have the opposite sign of the climatological values. This behavior is associated with a weakening of the zonal-mean zonal wind below 10 km. It is not altogether clear why this weakening of the tropospheric zonal-mean wind reduces the FGW momentum fluxes at their source, but a possibility is that the frequency of occurrence of fronts diminishes at this location; since the diagnosis of frontogenesis is the trigger for the FGWs in the model (Richter et al. 2010), infrequent frontogenesis will result in a weakening of the momentum flux associated with these waves. Some distance above the wave source, at 15–20 km, there is a sharp intensification of the momentum flux carried by the easterly components of the spectrum, which is most pronounced in the SH. This is related to the strengthening of the subtropical jets with increasing GHG concentrations (black curves). Above about 25 km, where the trends in the zonal-mean wind become negative, the flux carried by the easterly components is in turn attenuated, such that the momentum flux tendency of the easterly components of the FGW spectrum becomes small everywhere above 30 km. This, together with the decrease in the flux associated with westerly components of the spectrum noted above, produces a positive tendency in the net flux (green lines). Above 50 km, where the waves dissipate, this in turn gives rise to a negative tendency on FGWD, consistent with Fig. 6f.

5. Summary

WACCM4, the latest version of the Whole Atmosphere Community Climate Model, coupled to a fully interactive ocean model, has been used to investigate trends in the Brewer–Dobson circulation due to climate
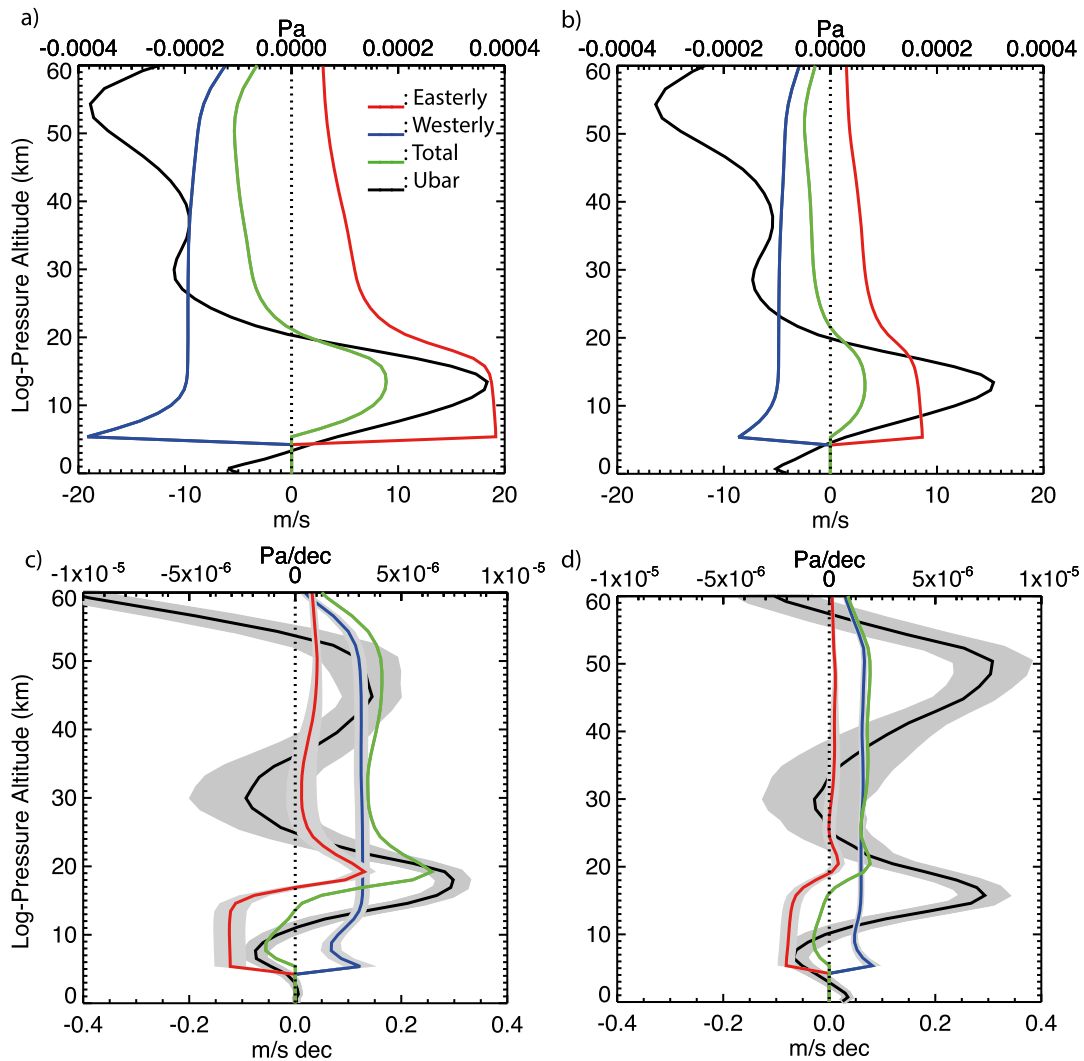
FIG. 10. Annual-mean (a),(b) climatology and (c),(d) trends of the frontal gravity wave momentum flux (red for waves of easterly phase velocity, blue for waves of westerly phase velocity, and green for the net flux) at (left) 20°S and (right) 20°N. Also shown in (c),(d) are trends in zonal-mean zonal wind (m s^{-1} decade^{-1}; black). Shadowing indicates the 2σ confidence limits.

change. The model reproduces both branches of the climatological circulation as previously documented in ERA-Interim (e.g., Seviour et al. 2012) and other modeling studies (e.g., Birner and Bönisch 2011). The shallow branch, in the lowermost stratosphere, has upwelling in the tropics and downwelling in the subtropics; the deep branch, whose maximum upwelling is located in the upper stratosphere (~48 km) is global in extent, with downwelling extending to polar latitudes and down into the polar troposphere (not shown). A seasonal analysis shows the shift of the tropical pipe into the summer hemisphere in both branches of the circulation; this shift is more noticeable in the deep branch.

The application of the DCP between the turn-around latitudes of the climatological tropical upwelling revealed

that different waves are involved in driving the climatology of the shallow and the deep branches. The climatological upwelling of the shallow branch is mainly driven by resolved waves (70%) with a nonnegligible contribution of OGWs (30%) at 70 hPa (~18.6 km), in agreement with Butchart et al.'s (2011) multimodel and reanalysis study. Resolved waves are also dominant in forcing the upwelling of the deep branch, followed by FGWs, which contribute negatively and consequently slow down the climatological circulation at these altitudes. Contributions from OGWs and CGWs are less than 10% to the deep branch upwelling.

Simulations using climate change scenarios show an acceleration of the BDC that increases with increasing loading of GHGs. Significant trends are found in both

branches of the BDC in RCP4.5 and RCP8.5 scenarios (larger in RCP8.5), but the trends are much weaker and mostly not significant in the RCP2.6 scenario. Trends in tropical upwelling are confined to lower latitudes than the climatological upwelling in the lower and upper stratosphere, where the maximum upwelling in both branches occurs, which indicates a narrowing of the tropical upwelling region in the lower stratosphere and in the stratopause region. In addition, the maximum changes in the upwelling of the upper stratosphere appear at higher altitudes than the climatology, indicating an upward extension of the circulation in these climate change scenarios. In WACCM4, the largest changes in the tropical upwelling occur at 100 hPa and at 1 hPa. In the upper stratosphere, the tropical upwelling increases up to 50% in the RCP8.5 scenario compared to climatology over the period covered by this simulation.

To identify the waves involved in the acceleration of the mean meridional circulation, we have applied the downward control principle, choosing the climatological turn-around latitudes of the historical period as the limits of integration for calculating tropical and extratropical mean $\overline{w}^*$ tendencies. The trend in the shallow branch upwelling is mainly due to waves that are explicitly resolved in the model (70%) while parameterized orographic gravity waves account for 30% in the lower stratosphere (at 70 hPa). This agrees with results from other chemistry–climate models such as the Atmospheric Model with Transport and Chemistry (AMTRAC) (Li et al. 2008), the Canadian Middle Atmosphere Model (CMAM) (McLandress and Shepherd 2009), and the previous version of WACCM, WACCM3.5 (GR08). In addition, Calvo and Garcia (2009) showed that the main driver of trends in the tropical upwelling of the lowermost stratosphere in WACCM3.5 was the EP flux divergence due to large-scale tropical Rossby waves. We note, nevertheless, that models are by no means unanimous in their attribution of trends in the shallow branch; in a minority of the models included in Fig. 4.11 of Eyring et al. (2010), the trend is due to changes in parameterized wave driving. In addition, the absolute magnitude of the trend, regardless of its source, varies considerably among models.

In the upper stratosphere, where frontal and convective gravity waves start to break, the contribution to the trend in the tropical upwelling is more heterogeneous than in the lower stratosphere. At these altitudes, frontal gravity waves play an important role in determining the upwelling trend, and their contribution becomes larger as the GHG burden increases. Trends in $\overline{w}^*$ calculated from the DCP revealed that more than 50% of the tropical upwelling trend near the stratopause in simulation RCP8.5 is due to changes in frontal gravity wave

drag while resolved wave drag accounts for 30%. The same methodology applied to the extratropics confirmed that frontal gravity waves are the main contributor to extratropical downwelling trends. The dominant role of frontal gravity waves in driving the mean meridional circulation trends in the upper stratosphere is related to changes in the background zonal-mean zonal winds. These changes in the winds modify the spectrum of frontal gravity waves such that the net momentum flux becomes more positive above the region where the subtropical jet intensifies ($\sim$15 km), such that the flux divergence in the upper stratosphere becomes more negative, which enhances tropical upwelling.

Finally, it should be borne in mind that the results presented here must be presumed to be model dependent. This is particularly the case in the upper stratosphere, where gravity waves are a major driver of the trends, since gravity waves are parameterized in general circulation models and these parameterizations differ among the models. Even in the lower stratosphere, Fig. 4.11 of Eyring et al. (2010) shows that, while all models produce positive tropical mass flux trends at 70 hPa, the magnitude of the trends and the relative contribution thereto by different waves varies from model to model. Nevertheless, insofar as the trends computed here depend on filtering of the (parameterized) upward-propagating gravity wave spectra by the evolving zonal-mean wind distribution, the sign and vertical distribution of the trends should be robust.

REFERENCES

Andrews, D. G., J. R. Holton, and C. B. Leovy, 1987: *Middle Atmosphere Dynamics.* International Geophysics Series, Vol. 40, Academic Press, 489 pp.

Birner, T., and H. Bönisch, 2011: Residual circulation trajectories and transit times into the extratropical lowermost stratosphere. *Atmos. Chem. Phys.,* **11,** 817–827, doi:10.5194/acp-11-817-2011.

Braesicke, P., and J. A. Pyle, 2004: Sensitivity of dynamics and ozone to different representations of SSTs in the Unified Model. *Quart. J. Roy. Meteor. Soc.,* **130,** 2033–2045, doi:10.1256/qj.03.183.

Butchart, N., and Coauthors, 2006: Simulations of anthropogenic change in the strength of the Brewer–Dobson circulation. *Climate Dyn.,* **27,** 727–741, doi:10.1007/s00382-006-0162-4.

——, and Coauthors, 2010: Chemistry–climate model simulations of twenty-first century stratospheric climate and circulation changes. *J. Climate,* **23,** 5349–5374, doi:10.1175/2010JCLI3404.1.

——, and Coauthors, 2011: Multimodel climate and variability of the stratosphere. *J. Geophys. Res.,* **116,** D05102, doi:10.1029/2010JD014995.

Calvo, N., and R. R. Garcia, 2009: Wave forcing of the tropical upwelling in the lower stratosphere under increasing concentrations of greenhouse gases. *J. Atmos. Sci.,* **66,** 3184–3196, doi:10.1175/2009JAS3085.1.

Danabasoglu, G., S. C. Bates, B. P. Briegleb, S. R. Jayne, M. Jochum, W. G. Large, S. Peacock, and S. G. Yeager, 2012: The CCSM4 ocean component. *J. Climate,* **25,** 1361–1389, doi:10.1175/JCLI-D-11-00091.1.

Deckert, R., and M. Dameris, 2008: Higher tropical SSTs strengthen the tropical upwelling via deep convection. *Geophys. Res. Lett.,* **35,** L10813, doi:10.1029/2008GL033719.

Eyring, V., T. G. Shepherd, and D. W. Waugh, Eds., 2010: SPARC report on the evaluation of chemistry climate models. SPARC Rep. 5, WCRP-132, WMO/TD-1526, 305 pp. [Available online at http://www.sparc-climate.org/publications/sparc-reports/sparc-report-no5/.]

Garcia, R. R., and W. J. Randel, 2008: Acceleration of the Brewer–Dobson circulation due to increases in greenhouse gases. *J. Atmos. Sci.,* **65,** 2731–2739, doi:10.1175/2008JAS2712.1.

Garny, H., M. Dameris, W. Randel, G. E. Bodeker, and R. Deckert, 2011: Dynamically forced increase of tropical upwelling in the lower stratosphere. *J. Atmos. Sci.,* **68,** 1214–1233, doi:10.1175/2011JAS3701.1.

Hardiman, S., N. Butchart, and N. Calvo, 2014: The morphology of the Brewer–Dobson circulation and its response to climate change in CMIP5 simulations. *Quart. J. Roy. Meteor. Soc.,* doi:10.1002/qj.2258, in press.

Haynes, P. H., C. J. Marks, M. E. McIntyre, T. G. Shepherd, and K. P. Shine, 1991: On the "downward control" of extratropical diabatic circulations by eddy-induced mean zonal forces. *J. Atmos. Sci.,* **48,** 651–680, doi:10.1175/1520-0469(1991)048<0651:OTCOED>2.0.CO;2.

Holland, M. M., D. A. Bailey, B. P. Briegleb, B. Light, and E. Hunke, 2012: Improved sea ice shortwave radiation physics in CCSM4: The impact of melt ponds and aerosols on Arctic sea ice. *J. Climate,* **25,** 1413–1430, doi:10.1175/JCLI-D-11-00078.1.

Holton, J. R., 1990: On the global exchange of mass between the stratosphere and troposphere. *J. Atmos. Sci.,* **47,** 392–395, doi:10.1175/1520-0469(1990)047<0392:OTGEOM>2.0.CO;2.

——, P. H. Haynes, M. E. McIntyre, A. R. Douglass, R. B. Rood, and L. Pfister, 1995: Stratosphere–troposphere exchange. *Rev. Geophys.,* **33,** 403–439, doi:10.1029/95RG02097.

Kosaka, Y., and S.-P. Xie, 2013: Recent global-warming hiatus tied to equatorial Pacific surface cooling. *Nature,* **501,** 403–407, doi:10.1038/nature12534.

Lean, J., G. Rottman, J. Harder, and G. Kopp, 2005: SORCE contributions to new understanding of global change and solar variability. *Sol. Phys.,* **230,** 27–53, doi:10.1007/s11207-005-1527-2.

Li, F., J. Austin, and J. Wilson, 2008: The strength of the Brewer–Dobson circulation in a changing climate: Coupled chemistry–climate model simulations. *J. Climate,* **21,** 40–57, doi:10.1175/2007JCLI1663.1.

Lin, P., and Q. Fu, 2013: Changes in various branches of the Brewer–Dobson circulation from an ensemble of chemistry climate models. *J. Geophys. Res. Atmos.,* **118,** 73–84, doi:10.1029/2012JD018813.

Marsh, D., M. J. Mills, D. E. Kinnison, J.-F. Lamarque, N. Calvo, and L. M. Polvani, 2013: Climate change from 1850 to 2005 simulated in CESM1(WACCM). *J. Climate,* **26,** 7372–7391, doi:10.1175/JCLI-D-12-00558.1.

Matthes, K., D. R. Marsh, R. R. Garcia, D. E. Kinnison, F. Sassi, and S. Walters, 2010: Role of the QBO in modulating the influence of the 11 year solar cycle on the atmosphere using constant forcings. *J. Geophys. Res.,* **115,** D18110, doi:10.1029/2009JD013020.

McLandress, C., and T. G. Shepherd, 2009: Simulated anthropogenic changes in the Brewer–Dobson circulation, including its extension to high latitudes. *J. Climate,* **22,** 1516–1540, doi:10.1175/2008JCLI2679.1.

Olsen, M. A., M. R. Schoeberl, and J. E. Nielsen, 2007: Response of stratospheric circulation and stratosphere–troposphere exchange to changing sea surface temperatures. *J. Geophys. Res.,* **112,** D16104, doi:10.1029/2006JD008012.

Richter, J. H., F. Sassi, and R. R. Garcia, 2010: Toward a physically based gravity wave source parameterization in a general circulation model. *J. Atmos. Sci.,* **67,** 136–156, doi:10.1175/2009JAS3112.1.

Rosenlof, K. H., 1995: Seasonal cycle of the residual mean meridional circulation in the stratosphere. *J. Geophys. Res.,* **100,** 5173–5191, doi:10.1029/94JD03122.

Seviour, W. J. M., N. Butchart, and S. C. Hardiman, 2012: The Brewer–Dobson circulation inferred from ERA-Interim. *Quart. J. Roy. Meteor. Soc.,* **138,** 878–888, doi:10.1002/qj.966.

Shepherd, T. G., and C. McLandress, 2011: A robust mechanism for strengthening of the Brewer–Dobson circulation in response to climate change: Critical-layer control of subtropical wave breaking. *J. Atmos. Sci.,* **68,** 784–797, doi:10.1175/2010JAS3608.1.

Tilmes, S., R. R. Garcia, D. E. Kinnison, A. Gettelman, and P. J. Rasch, 2009: Impact of geoengineered aerosols on the troposphere and stratosphere. *J. Geophys. Res.,* **114,** D12305, doi:10.1029/2008JD011420.

Chapter 7

Discussion

This thesis has addressed several questions regarding two major phenomena of stratospheric variability: SSWs and the BDC. Vertical motions of the BDC can be well diagnosed by the zonal-mean residual circulation in the TEM framework, as described in Chapter 1. However, the SSW definition is still under discussion (e.g., Butler et al. 2015). The first part of this thesis, Chapter 3, has dealt with the relevance of the method used to detect SSWs. Previous studies argued that the SSW definition can affect relevant results such as their surface impacts (Maycock and Hitchcock 2015) or the future trends in SSW frequency under climate change conditions (McLandress and Shepherd 2009a). The eight methods selected in this thesis are representative of all definitions found in the literature, based on different variables (temperature, zonal wind, etc.), approaches (absolute methods, Principal Component Analysis, etc.) or latitudes to detect SSWs (see Fig.1 in Palmeiro et al. 2015). We evaluate these definitions in ERA reanalysis data from 1958 to 2014 and in two other long reanalyses (JRA-55 and NCEP-NCAR). The reanalyses comparison is motivated by the rising interest of reporting differences among these datasets under the SRIP-Project initiative (http://s-rip.ees.hokudai.ac.jp/)

The average frequency of SSWs for all definitions is almost 7 events per decade regardless of the reanalysis dataset, with values that range from 4 to 11 events dec^{-1}, mostly depending on the consideration of minor SSWs. While the resulting intraseasonal distribu-

tions of SSW occurrence are similar among definitions, and display the largest frequency in January, the interdecadal distribution is method-dependent, and the minimum frequency in the 1990s reported in several studies is only captured by methods demanding the wind reversal at 60°N. This condition is indeed the most widely employed to define SSWs in the literature, and thus, previous studies addressing low-frequency variations of SSWs might not be robust. Apart from small variations in the SSW frequencies, no significant differences were obtained in the main signatures of SSWs among these three reanalyses.

Dynamical benchmarks of SSWs in the middle and lower stratosphere indicated that case-to-case variability within methods is larger than the inter-method differences, so all definitions are equally suitable to study the stratospheric signatures of SSWs. At the surface, major SSWs, which are commonly detected by most methods, show the strongest and most coherent responses. In contrast, minor SSWs are more specific of each method and do not show robust stratosphere-troposphere coupling. An important question arises about the causes of the case-to-case variability in the stratospheric signatures of SSWs and how they are related to the spread in the surface responses. In this sense it would be useful to explore if, in addition to major SSWs, there are other factors that modulate the degree of stratosphere-troposphere coupling. This would be informative to assess the potential skill of SSWs in seasonal forecasts.

The results reported here have also implications for the undergoing revision of the SSW definition (see e.g. discussion in Butler et al. 2015). As shown in Chapter 3, although the stratosphere-troposphere coupling is well captured by zonal-mean zonal wind reversals at 60°N and 10hPa this diagnostic is not robust, causing a spurious minimum of SSW occurrence in the 1990s. Instead, we propose to use a range of latitudes, from 55°N to 70°N, ensuring that the polar vortex edge is being evaluated. This is important to account for cases when the vortex is different to the observed climatological mean conditions, as it might occur in climate models, under climate change conditions, or in the 1990s. This method increases the sample size, and shows strong signals in the downward propagation

and the surface imprints before and after SSWs. Moreover, it is simple and similar to previous definitions proposed in the literature but it avoids the aforementioned methodological artefacts. Therefore, it was applied to detect SSWs in the remainder of this thesis (Chapters 4 and 5).

SSWs are the main source of intraseasonal variability in the polar winter stratosphere. Thus, it is essential for climate models to reproduce the observed frequencies and signatures of SSWs (e.g., Gerber and Polvani 2009). Many climate models, including some high-top models, tend to underestimate the SSW occurrence (e.g., Charlton-Pérez et al. 2013). This was the case of WACCM3 and previous versions of this model. In WACCM3.5, and subsequent releases, the TMS parameterization was found to be critical to reproduce the observed SSW frequencies (Richter et al. 2010). Chapter 4 addresses how the TMS modulates SSW occurrence in WACCM4 by comparing two simulations with (TMS-on) and without (TMS-off) the TMS parameterization. This version of WACCM is coupled to an interactive ocean (Marsh et al. 2013), such that sea surface temperatures and sea ice do not need to be prescribed, thus including important atmosphere-ocean feedbacks that add realism to the results. Moreover, the parameterization of GWs includes non-arbitrary GW sources and hence the representation of these waves and the associated drag is more realistic than in previous versions of the model. The results indicate that TMS-off strongly underestimates the observed SSW frequencies in early winter (from December to February), but reproduces March SSW frequencies adequately. Differently, TMS-on shows realistic SSW frequencies throughout the winter, including the observed peak of occurrence in January found in reanalysis (Chapter 3). Additional analysis show that the TMS parameterization decreases OGWD in the NH, modifying the refractive conditions in the subtropical jet region and favoring poleward PW propagation, as reported in Richter et al. (2010). However, this mechanism operates throughout the whole season and hence it is not able to explain the intraseasonal differences in the occurrence of SSWs between TMS-on and TMS-off.

A new mechanism is proposed here through compensation between OGWs and PWs in the middle and high latitudes of the stratosphere. This means that PW forcing increases or decreases depending on the OGWD existing in that region in order to preserve the total forcing. This compensation is in line with that proposed in Cohen et al. (2014) regarding the different wave contributions to the BDC. They showed that an imposed torque in a certain region of the middle stratosphere causes the PWs to respond with a similar decrease in their torque. In Chapter 4, the TMS-off simulation would be analogue to the case in which an additional torque (OGWD) is applied, so that PW forcing decreases in the stratosphere and SSWs are less likely to occur.

Although the particular causes of SSWs occurrence are not well understood, the model of Matsuno (1971) based on the PW interaction with the polar vortex has been widely assumed (Andrews et al. 1987). In contrast, the role of GWs in relation to SSWs is not well understood (Yamashita et al. 2010). Recent studies have pointed to an influence of GWs in preconditioning the polar vortex (Albers and Birner 2014), and prior studies even suggested that GWs can trigger SSWs (Pawson 1997). Results from Chapter 4 highlight the requirement of a large PW drag to produce SSWs, while the role of GWs would be limited to modulate the PW drag through the compensation mechanism. If the paradigm of compensation operates in other climate models, it might indicate that improving GW parameterizations can lead to changes in the simulation of resolved PWs which in turn, might help to solve models' deficiencies in reproducing realistic SSW frequencies, as shown in Charlton-Pérez et al. (2013).

Interactions between PWs and GWs have been considered in many modeling studies regarding the so-called SH cold-pole bias (e.g., Austin et al. 2003, Hurwitz et al. 2010, McLandress et al. 2012, Scheffler and Pulido 2015). This bias refers to the lower than normal temperatures simulated by most CCMs (Eyring et al. 2006) in the southern polar vortex. These lower temperatures are accompanied by a stronger polar vortex, delaying the occurrence of the SFW. Using a middle-atmosphere dynamical model, Scheffler and

Pulido (2015) showed that decreasing the GW fluxes from the lower stratosphere leads to an increase of PW drag that resulted in the improvement of the SFW date. What is clear, is that GWs are critical in climate models to reproduce the observed stratospheric variability (Fritts and Alexander 2003), and hopefully, the enhanced resolution of incoming climate models might shed some light on how PWs and GWs interplay.

Similar to SSWs, the BDC is also wave-driven, with the downwelling of its deep branch occurring within the stratospheric polar vortex location. The potential interactions between the deep branch of the BDC and SSWs are assessed in Chapter 5 by using WACCM4 simulations with and without increasing concentrations of GHGs. Consistent with the enhanced Eliassen-Palm (EP) flux convergence before SSWs, there is an increment of up to 50% in the BDC strength, while the opposite is obtained after SSWs. Under climate change conditions (RCP8.5 scenario) the future impact of SSWs on the BDC appears to be stronger, but considering the accelerating trend of the BDC (Chapter 6), the BDC responses to SSWs remain similar to those in the present-day.

Interestingly, the impacts of March SSWs on the BDC resemble those obtained for early (March) SFWs. The fact that early SFWs behave like SSWs was already suggested in Hu et al. (2014) and this has been confirmed by other studies addressing their surface responses over the Euro-Atlantic sector (e.g., Ayarzagüena and Serrano 2009, Palmeiro et al. 2017a). However, Chapter 5 demonstrates that SSWs and early SFWs (referred here as March warmings) have weaker impacts on the BDC than mid-winter SSWs. This might be related to the weaker westerlies in March, such that less forcing is needed to disturb the polar vortex which would also result in weaker NAM anomalies. The results of Chapter 5 suggest that early SFWs should be considered as (March) SSWs and hence, future catalogues should include these events. However, it remains to be explored whether or not March warmings as a whole are distinguishable of (and hence should be separated from) mid-winter SSWs in what concerns their tropospheric impacts and forecast skill.

Given that March warmings also weaken the polar downwelling during their recovery phase in late winter, they can modulate the winter-to-summer transition of the BDC (i.e., the shift from downwelling to upwelling in the polar stratosphere). The overall effect of March warmings is to anticipate the BDC transition by ~10 days, on average. When compared to present-day conditions, the impact of March warmings increases in the RCP8.5, thus anticipating the BDC transition by ~14 days in the future. This amplified effect is due to an overall delay of the BDC transition rather than to a future change in the transition dates of winters with March warmings. Assuming that the beginning of the winter circulation in the stratosphere does not change under increasing GHGs, the future delay of the BDC transition would involve a more extended winter season and hence a longer-lasting control of the stratosphere on the troposphere. Together with the projected acceleration of the BDC, this raises the question of whether the potential skill of the stratosphere in seasonal predictions would also increase in the future. The BDC transition, as defined in this thesis, and the SFW might be interpreted as different measures of the same phenomenon. Although they are both driven by waves, SFWs are also partially driven by the radiative cycle. Forster et al. (1997), showed in fact, that what advances the occurrence of the SFW is wave forcing.

The basis of the interaction mechanism between SSWs and the BDC suggested here relies on the "stratospheric control" of the BDC introduced in Gerber (2012) and the extratropical pump of Holton et al. (1995). This stratospheric control refers to the control that the characteristics of the stratospheric polar vortex exert on wave breaking. Before SSWs, enhanced wave propagation and dissipation into the stratosphere accelerate the BDC downwelling. By mass conservation, this implies an enhancement of the tropical upwelling of the deep branch that induces tropical cooling. The tropical signal of the SSW was previously reported in other studies (e.g., Kodera 2006, Taguchi 2011, Gómez-Escolar et al. 2014). In particular, Gómez-Escolar et al. (2014) showed how the SSWs response in the tropical upwelling is modulated by the phase of the Quasi-Biennial Oscillation (QBO), although they did not look at the deep branch of the BDC directly. It is known that the

116

tropical QBO can affect the strength of the polar vortex (Holton-Tan relationship, Holton and Tan, 1980). In this sense, further analyses on the relationship between the deep branch of the BDC and SSWs regarding the phase of the QBO might elucidate any potential modulation of the QBO on the results of Chapter 5.

Finally, a deeper analysis to characterize the wave driving of the BDC and the anthropogenic induced changes is carried out in Chapter 6 by evaluating the climatology of the BDC in present-day conditions and in three different climate change scenarios (RCP2.6, RCP4.5 and RCP8.5) with WACCM4.

WACCM4 reproduces the shallow and deep branches of the BDC similar to reanalysis data (see e.g. Seviour et al. 2012). Using the downward control principle, the shallow branch in WACCM4 was found to be driven by PWs ($\sim$70%) and GWs ($\sim$30%), similar to most models included in the CMIP5 and to reanalysis (Butchart et al. 2011, Seviour et al. 2012). Although the deep branch is also dominated by PWs, FGWs act to slow down the upwelling in the upper stratosphere.

In response to increasing GHGs, both branches of the BDC accelerate by up to 50% in the RCP8.5, and an expansion of the deep branch tropical upwelling can be observed at the end of the 21st century. In the shallow branch, the acceleration trends in the different scenarios were attributed to similar contributions of both planetary and gravity waves (70% vs 30% respectively). This is in agreement with results from previous versions of WACCM (Garcia and Randel 2008) and other individual modeling studies (e.g., Li et al. 2008, McLandress and Shepherd 2009b). Trends in the upwelling of the deep branch are dominated by changes in FGWs, whose deceleration contribution diminishes in the future, allowing the deep branch upwelling to increase. The mechanism behind this trend relies on the projected strengthening of the subtropical jets under climate change conditions. The stronger subtropical jets filter out the westerly spectrum of GWs and hence, the net spectrum of FGWs becomes more easterly, and thus larger negative wave drag in the upper

stratosphere enhances tropical upwelling in the deep branch.

While trends in the downwelling branch of the NH are also dominated by changes in FGWD, the attribution of trends in the SH is more complicated as the effect of both increasing GHGs and decreasing ODS might affect future changes. In this case, the effects of ozone recovery dominate in the three scenarios, showing a deceleration of the climatological downwelling in the SH, as reported in McLandress and Shepherd (2009b). This response to ozone recovery is consistent with enhanced downwelling reported in austral summer in response to ozone depletion (e.g., Manzini et al. 2003, Li et al. 2008, Calvo et al. 2017). Given the strong repercussions that ozone depletion and recovery have in the global climate system (Arblaster and Gillet et al. 2014), further research on the deep branch of the BDC is essential to determine the time scales at which ODS are processed and removed. In this context, the impact of SSWs in accelerating and decelerating the BDC might involve changes on the ODS and other chemical species in the upper stratosphere. This is not only important in the southern but also in the northern pole, given the uncertainties and expected increase in Arctic ozone holes in the future (Hand 2016).

Chapter 8

Conclusions

The main conclusions of this thesis are listed next:

1. **The comparison of eight different SSW definitions in three reanalysis datasets revealed that the particular details of the definition used to detect SSWs are not relevant as long as the number of minor warmings is minimized. In particular:**

   - The average frequency of SSWs is 6.7, 6.8 and 6.5 events per decade in the ERA, NCEP-NCAR and JRA-55 reanalyses, respectively. This average frequency ranges from 4 to 11 depending on the SSW definition. All methods show a similar intraseasonal distribution but the decadal variability is method-dependent.

   - The exact central dates of SSWs depend on the definition, and those based on relative fields (i.e., long-term anomalies or short-term tendencies) tend to detect SSWs earlier.

   - Regarding the characteristics of the SSWs' lifecycle and the associated benchmarks in the stratosphere, the case-to-case variability among SSWs is larger than the inter-method spread.

   - Minor SSWs are the main source of discrepancy across definitions, showing

weak stratosphere-troposphere coupling and less robust surface precursors and responses.

- A latitudinal belt centered on the vortex edge rather than a given latitude seems to be more appropriate to detect SSWs as zonal-mean zonal wind reversals. In this fashion, the results are more robust and avoid spurious effects.

2. **Analysis of the role of TMS on SSW occurrence in WACCM simulations reveals that a realistic simulation of OGWD, which needs to be parameterized in this model, is essential to reproduce the observed PW forcing and stratospheric variability.**

- With the TMS implementation, WACCM4 is able to reproduce the observed frequencies and intraseasonal distributions of SSWs. The SSW frequency in early winter is drastically reduced in equivalent simulations without TMS.

- The TMS has a direct effect on decreasing the OGWD by decelerating the surface winds. The largest effects of the TMS occur over the Rocky Mountains and the Himalayas.

- The resulting changes in the refractive properties of the subtropical jet region tend to enhance PW propagation towards high latitudes in TMS-on through the entire winter, while the opposite is observed in TMS-off. This mechanism cannot explain why TMS-off reproduces the observed frequencies of March SSWs.

- Compensation between PWs and GWs can explain the TMS differences in the intraseasonal SSW occurrence. Thus, the reduced OGWD induced by the TMS at middle latitudes in early and mid-winter is balanced by an increase in PW drag and hence, improved frequencies of SSWs.

3. **SSW occurrence in WACCM4 affects the deep branch of the BDC. SSWs are associated with a strengthening of the polar downwelling of the deep branch in the NH before the vortex breakdown and a weakening during the vortex recovery.**

120

- Enhanced PW convergence preceding SSWs strengthens the polar downwelling of the deep branch of the BDC by up to 50%. The BDC weakens during the month following the SSW due to the inhibition of PW upward propagation.

- The effects of March SSWs on the BDC are similar to those of early (March) SFWs, and weaker than those of mid-winter SSWs.

- March warmings, including both March SSWs and early SFWs, lead to an anticipated BDC transition to the summer regime.

- These conclusions remain qualitatively similar in the future under a climate change (RCP8.5) scenario, although the quantitative effects are modulated by anthropogenic trends in the polar downwelling of the deep branch of the BDC, which experiences an overall strengthening and a delayed transition to the summer regime.

4. **WACCM4 reproduces the shallow branch and the less investigated deep branch of the BDC similar to reanalysis. The BDC shows an acceleration due to increasing GHG concentrations. While PWs dominate the trends in the upwelling of the shallow branch, FGWs are responsible for trends in the upwelling of the deep branch.**

   - The dominant forcings in driving the climatological tropical upwelling of the deep branch of the BDC in WACCM4 are PWs followed by FGWs, whose contribution is negative (i.e., a positive wave drag and a slowdown of the BDC).

   - There is a projected increase in the tropical upwelling of the deep branch of the BDC of up to 50% in the RCP8.5 scenario.

   - The accelerating trends in the shallow branch are due to increased wave drag from resolved PWs ($\sim$70%) and OGWs ($\sim$30%).

   - The deep branch enhancement entails an upward expansion to the stratopause due to reduced FGWD (> 50%), and from PWs. The upward intensification of the subtropical jets in the future simulations modifies the FGW spectrum,

resulting in a less positive wave drag in the upper stratosphere that accelerates the BDC.

References

Abalos, M., B. Legras, F. P. and W. J., and Randel, (2015): Evaluating the advective Brewer-Dobson circulation in three reanalyses for the period 1979 – 2012. J. Geophys. Res. Atmos., 1–21, doi:10.1002/2015JD023182.

Albers, J. R., and Birner, T. (2014). Vortex preconditioning due to planetary and gravity waves prior to sudden stratospheric warmings. Journal of the Atmospheric Sciences, 71(11), 4028-4054.

Allen, D. R., Bevilacqua, R. M., Nedoluha, G. E., Randall, C. E., and Manney, G. L. (2003). Unusual stratospheric transport and mixing during the 2002 Antarctic winter. Geophysical Research Letters, 30(12).

Ambaum, M. H., Hoskins, B. J., and Stephenson, D. B. (2001). Arctic oscillation or North Atlantic oscillation?. Journal of Climate, 14(16), 3495-3507.

Andrews, D. G., and McIntyre, M. E. (1976). Planetary waves in horizontal and vertical shear: The generalized Eliassen-Palm relation and the mean zonal acceleration. Journal of the Atmospheric Sciences, 33(11), 2031-2048.

——, D. G., and McIntyre M. E. (1978). Generalized Eliassen-Palm and Charney-Drazin Theorems for Waves on Axisymmetric Mean Flows in Comprenssible Atmospheres. J.

Atmos. Sci., 35, 175.

——, D. G., Holton, J. R., and Leovy, C. B. (1987). Middle atmosphere dynamics (No. 40). Academic press.

Arblaster, J.M., and N.P Gillett (Lead Authors), N. Calvo, P.M. Forster, L.M. Polvani, S.-W. Son, D.W. Waugh, and P.J. Young, Stratospheric ozone changes and climate, Chapter 4 in Scientific Assessment of Ozone Depletion: 2014, Global Ozone Research and Monitoring Project – Report No. 55, World Meteorological Organization, Geneva, Switzerland, 2014.

Austin, J., Shindell, D., Beagley, S. R., Brühl, C., Dameris, M., Manzini, E., ... and Rozanov, E. (2003). Uncertainties and assessments of chemistry-climate models of the stratosphere. Atmospheric Chemistry and Physics, 3(1), 1-27.

Ayarzagüena, B., and Serrano, E. (2009). Monthly characterization of the tropospheric circulation over the Euro-Atlantic area in relation with the timing of stratospheric final warmings. Journal of Climate, 22(23), 6313-6324.

Baldwin, M. P., and Dunkerton T. J., (2001). Stratospheric harbingers of anomalous weather regimes. Science, 294, 581–584, doi:10.1126/science.1063315.

——, Stephenson, D. B., Thompson, D. W. J., Dunkerton, T. J., Charlton, A. J., and O'Neill, A. (2003). Stratospheric memory and skill of extended-range weather forecasts. Science, 301, 636–640.

Barriopedro, D., and Calvo, N. (2014). On the relationship between ENSO, stratospheric sudden warmings, and blocking. Journal of Climate, 27(12), 4704-4720.

Bell, C. J., Gray, L. J., Charlton-Perez, A. J., Joshi, M. M., and Scaife, A. A. (2009). Stratospheric communication of El Niño teleconnections to European winter. Journal of Climate, 22(15), 4083-4096.

Birner, T., and Bönisch, H. (2011). Residual circulation trajectories and transit times into the extratropical lowermost stratosphere. Atmospheric Chemistry and Physics, 11(2), 817-827.

Boville, B. A., and Baumhefner, D. P. (1990). Simulated forecast error and climate drift resulting from the omission of the upper stratosphere in numerical models. Monthly weather review, 118(7), 1517-1530.

Brasseur, G. P., and Solomon, S. (2006). Aeronomy of the middle atmosphere: chemistry and physics of the stratosphere and mesosphere (Vol. 32). Springer Science and Business Media.

Brewer, A. W. (1949). Evidence for a world circulation provided by the measurements of helium and water vapour distribution in the stratosphere. Quarterly Journal of the Royal Meteorological Society, 75(326), 351-363.

Butchart, N. (2014). The Brewer-Dobson circulation. Reviews of geophysics, 52(2), 157-184

——, Scaife, A. A., Bourqui, M., De Grandpré, J., Hare, S. H. E., Kettleborough, J. Langematz, U., Manzini, E., Sassi, F., Shibata, K. and Shindell, D. (2006). Simulations of anthropogenic change in the strength of the Brewer–Dobson circulation. Climate Dynamics, 27(7-8), 727-741.

——, Cionni, I., Eyring, V., Shepherd, T. G., Waugh, D. W., Akiyoshi, H., Austin, J., Brühl, C., Chipperfield, M.P., Cordero, E. and Dameris, M. (2010). Chemistry–climate model simulations of twenty-first century stratospheric climate and circulation changes. Journal of Climate, 23(20), 5349-5374.

——, Charlton-Perez, A. J., Cionni, I., Hardiman, S. C., Haynes, P. H., Krüger, K., Kushner, P.J., Newman, P.A., Osprey, S.M., Perlwitz, J. and Sigmond, M. (2011). Multimodel climate and variability of the stratosphere. Journal of Geophysical Research: Atmospheres, 116(D5).

Butler, A. H., Seidel, D. J., Hardiman, S. C., Butchart, N., Birner, T., and Match, A. (2015). Defining sudden stratospheric warmings. Bulletin of the American Meteorological Society, 96(11), 1913-1928.

——, Sjoberg, J. P., Seidel, D. J., and Rosenlof, K. H. (2017). A sudden stratospheric warming compendium. Earth System Science Data, 9(1), 63.

Cagnazzo C. and Manzini E. (2009). Impact of the stratosphere on the winter tropospheric teleconnections between ENSO and the North Atlantic and European region. J Clim 22:1223–1238. doi: 10.1175/2008JCLI2549.1

Calvo-Fernández, N. C., Herrera, R. G., Puyol, D. G., Martin, E. H., GarcÍa, R. R., Presa, L. G., and RodrÍguez, P. R. (2004). Analysis of the ENSO signal in tropospheric and stratospheric temperatures observed by MSU, 1979–2000. Journal of climate, 17(20), 3934-3946.

Calvo, N., Giorgetta, M. A., and Peña-Ortiz, C. (2007). Sensitivity of the boreal winter circulation in the middle atmosphere to the quasi-biennial oscillation in MAECHAM5 simulations. Journal of Geophysical Research: Atmospheres, 112(D10).

——, Giorgetta, M. A., Garcia-Herrera, R., and Manzini, E. (2009). Nonlinearity of the combined warm ENSO and QBO effects on the Northern Hemisphere polar vortex in MAECHAM5 simulations. Journal of Geophysical Research: Atmospheres, 114(D13).

——, Iza, M., Hurwitz, M. M., Manzini, E., Peña-Ortiz, C., Butler, A. H., ... and Garfinkel, C. I. (2017). Northern Hemisphere Stratospheric Pathway of different El Niño flavors in stratosphere-resolving CMIP5 models. Journal of Climate, 30(12), 4351-4371.

Camp, C. D., and K.-K. Tung, 2007: Stratospheric polar warming by ENSO in winter: A statistical study. Geophys. Res. Lett., 34, L04809, doi:10.1029/2006GL028521.

Charlton, A. J., and Polvani, L. M. (2007). A new look at stratospheric sudden warmings. Part I: Climatology and modeling benchmarks. Journal of Climate, 20(3), 449-469.

——, O'neill, A., Lahoz, W. A., and Massacand, A. C. (2004). Sensitivity of tropospheric forecasts to stratospheric initial conditions. Quarterly Journal of the Royal Meteorological Society, 130(600), 1771-1792.

Charlton-Perez, A. J., Baldwin, M. P., Birner, T., Black, R. X., Butler, A. H., Calvo, Davis, N.A., Gerber, E.P., Gillett, N., Hardiman, S. and Kim, J. (2013). On the lack of stratospheric dynamical variability in low-top versions of the CMIP5 models. Journal of Geophysical Research: Atmospheres, 118(6), 2494-2505.

Charney, J. G., and Drazin, P. G. (1961). Propagation of planetary-scale disturbances from the lower into the upper atmosphere. Journal of Geophysical Research, 66(1), 83-109.

Chiodo, G., Calvo, N., Marsh, D. R., and Garcia-Herrera, R. (2012). The 11 year solar cycle signal in transient simulations from the Whole Atmosphere Community Climate Model. Journal of Geophysical Research: Atmospheres, 117(D6).

——, G., D. Marsh, R. Garcia-Herrera, N. Calvo, and J. García (2014), On the detection of the solar signal in the tropical stratosphere, Atmospheric Chemistry and Physics, 14(11), 5251–5269.

Cohen, N. Y., Gerber, E. P., and Bühler, O. (2014). What drives the Brewer–Dobson circulation?. Journal of the Atmospheric Sciences, 71(10), 3837-3855.

Coy, L., Eckermann, S., and Hoppel, K. (2009). Planetary wave breaking and tropospheric forcing as seen in the stratospheric sudden warming of 2006. Journal of the Atmospheric Sciences, 66(2), 495-507.

Davini, P., and D'Andrea, F. (2016). Northern Hemisphere Atmospheric Blocking Representation in Global Climate Models: Twenty Years of Improvements?. Journal of Climate, 29(24), 8823-8840.

Dee, D. P., Uppala, S. M., Simmons, A. J., Berrisford, P., Poli, P., Kobayashi, S., ... and Bechtold, P. (2011). The ERAInterim reanalysis: Configuration and performance of the data assimilation system. Quarterly Journal of the royal meteorological society, 137(656), 553-597.

Dobson, G. M. B. (1956). Origin and distribution of the polyatomic molecules in the atmosphere. Proceedings of the Royal Society of London. Series A, Mathematical and Physical Sciences, 236(1205), 187-193.

Dunn-Sigouin, E., and Shaw, T. A. (2015). Comparing and contrasting extreme stratospheric events, including their coupling to the tropospheric circulation. Journal of Geophysical Research: Atmospheres, 120(4), 1374-1390.

128

Ebita, A., Kobayashi, S., Ota, Y., Moriya, M., Kumabe, R., Onogi, K., ... and Kamahori, H. (2011). The Japanese 55-year reanalysis "JRA-55": an interim report. Sola, 7, 149-152.

Eyring, V., Butchart, N., Waugh, D. W., Akiyoshi, H., Austin, J., Bekki, S., ... and Cordero, E. (2006). Assessment of temperature, trace species, and ozone in chemistryclimate model simulations of the recent past. Journal of Geophysical Research: Atmospheres, 111(D22).

Forster, P. D. F., Freckleton, R. S., and Shine, K. P. (1997). On aspects of the concept of radiative forcing. Climate Dynamics, 13(7), 547-560.

Forster, P., Thompson, D., and Baldwin, M. P. (2011). Stratospheric changes and climate, Chapter 4 in Scientific assessment of ozone depletion: 2010, Global Ozone Research and Monitoring Project–Report no. 52. World Meteorological Organization, Geneva.

Fritts, D. C., and Alexander, M. J. (2003). Gravity wave dynamics and effects in the middle atmosphere. Reviews of geophysics, 41(1).

Fu, Q., Lin, P., Solomon, S., and Hartmann, D. L. (2015). Observational evidence of strengthening of the BrewerDobson circulation since 1980. Journal of Geophysical Research: Atmospheres, 120(19).

Garcia, R. R., and Solomon, S. (1985). The effect of breaking gravity waves on the dynamics and chemical composition of the mesosphere and lower thermosphere. Journal of Geophysical Research: Atmospheres, 90(D2), 3850-3868.

——, and Randel, W. J. (2008). Acceleration of the Brewer–Dobson circulation due to increases in greenhouse gases. Journal of the Atmospheric Sciences, 65(8), 2731-2739.

Garny, H., Dameris, M., Randel, W., Bodeker, G. E., and Deckert, R. (2011). Dynamically forced increase of tropical upwelling in the lower stratosphere. Journal of the Atmospheric Sciences, 68(6), 1214-1233

Gerber, E. P., and Polvani, L. M. (2009). Stratosphere–troposphere coupling in a relatively simple AGCM: The importance of stratospheric variability. Journal of Climate, 22(8), 1920-1933.

——, (2012). Stratospheric versus tropospheric control of the strength and structure of the Brewer–Dobson circulation. Journal of the Atmospheric Sciences, 69(9), 2857-2877.

——, Butler, A., Calvo, N., Charlton-Perez, A., Giorgetta, M., Manzini, E , Perlwitz, J., Polvani, L.M., Sassi, F., Scaife, A.A. and Shaw, T.A. (2012). Assessing and understanding the impact of stratospheric dynamics and variability on the earth system. Bulletin of the American Meteorological Society, 93(6), 845-859.

GómezEscolar, M., Calvo, N., Barriopedro, D., and Fueglistaler, S. (2014). Tropical response to stratospheric sudden warmings and its modulation by the QBO. Journal of Geophysical Research: Atmospheres, 119(12), 7382-7395.

Graf, H., Q. Li, and M. Giorgetta (2007), Volcanic effects on climate: revisiting the mechanisms Atmospheric Chemistry and Physics, 7(17), 4503–4511

Hand, E. (2016). Record ozone hole may open over Arctic in the spring. Science, 351.6274, 650-650.

Hardiman, S. C., Butchart, N., Hinton, T. J., Osprey, S. M., and Gray, L. J. (2012). The effect of a well-resolved stratosphere on surface climate: Differences between CMIP5

simulations with high and low top versions of the Met Office Climate Model. Journal of Climate, 25(20), 7083-7099.

——, Butchart, N., and Calvo, N. (2014). The morphology of the Brewer–Dobson circulation and its response to climate change in CMIP5 simulations. Quarterly Journal of the Royal Meteorological Society, 140(683), 1958-1965.

——, Lin, P., Scaife, A. A., Dunstone, N. J., and Ren, H. L. (2017). The influence of dynamical variability on the observed Brewer-Dobson circulation trend. Geophysical Research Letters, 44(6), 2885-2892.

Haynes, P. H., McIntyre, M. E., Shepherd, T. G., Marks, C. J., and Shine, K. P. (1991). On the "downward control" of extratropical diabatic circulations by eddy-induced mean zonal forces. Journal of the Atmospheric Sciences, 48(4), 651-678.

Holton, J. R., and Tan, H. C. (1980). The influence of the equatorial quasi-biennial oscillation on the global circulation at 50 mb. Journal of the Atmospheric Sciences, 37(10), 2200-2208.

——, (1990). On the global exchange of mass between the stratosphere and troposphere. Journal of the atmospheric sciences, 47(3), 392-395.

——, Haynes, P. H., McIntyre, M. E., Douglass, A. R., Rood, R. B., and Pfister, L. (1995). Stratosphere-troposphere exchange. Reviews of geophysics, 33(4), 403-439

Hu, J. G., R. C. Ren, Y. Y. Yu, and X. HaiMing (2014), The boreal spring stratospheric final warming and its interannual and interdecadal variability, Sci. China Earth Sci., 57, 710–718, doi:10.1007/s11430-013-4699-x.

Hurwitz, M. M., Newman, P. A., Li, F., Oman, L. D., Morgenstern, O., Braesicke, P., and Pyle, J. A. (2010). Assessment of the breakup of the Antarctic polar vortex in two new chemistryclimate models. Journal of Geophysical Research: Atmospheres, 115(D7).

Ineson, S., Scaife, A. A., Knight, J. R., Manners, J. C., Dunstone, N. J., Gray, L. J., and Haigh, J. D. (2011). Solar forcing of winter climate variability in the Northern Hemisphere. Nature Geoscience, 4(11), 753.

IPCC, Climate Change 2013: The Physical Science Basis, Contribution of Working Group I to the Fifth Assessment Report of the Intergovernmental Panel on Climate Change, Technical Summary, 2013.

Ineson, S., and Scaife, A. A. (2009). The role of the stratosphere in the European climate response to El Niño. Nature Geoscience, 2(1), 32.

Iza, M., Calvo, N., and Manzini, E. (2016). The Stratospheric Pathway of La Niña. Journal of Climate, 29(24), 8899-8914.

Karpechko, A. Y., Hitchcock, P., Peters, D. H., and Schneidereit, A. (2017). Predictability of downward propagation of major sudden stratospheric warmings. Quarterly Journal of the Royal Meteorological Society, 143(704), 1459-1470.

Kim, J., Son, S. W., Gerber, E. P., and Park, H. S. (2017). Defining Sudden Stratospheric Warming in Climate Models: Accounting for Biases in Model Climatologies. Journal of Climate, (2017).

Kodera, K. (2006). Influence of stratospheric sudden warming on the equatorial troposphere. Geophysical Research Letters, 33(6).

132

——, Mukougawa, H., Maury, P., Ueda, M., and Claud, C. (2016). Absorbing and reflecting sudden stratospheric warming events and their relationship with tropospheric circulation. Journal of Geophysical Research: Atmospheres, 121(1), 80-94.

Krüger, K., Naujokat, B., and Labitzke, K. (2005). The unusual midwinter warming in the Southern Hemisphere stratosphere 2002: A comparison to Northern Hemisphere phenomena. Journal of the atmospheric sciences, 62(3), 603-613.

Li, F., Austin, J., and Wilson, J. (2008). The strength of the Brewer–Dobson circulation in a changing climate: Coupled chemistry–climate model simulations. Journal of Climate, 21(1), 40-57.

Limpasuvan, V., Hartmann, D. L., Thompson, D. W., Jeev, K., and Yung, Y. L. (2005). Stratosphere-troposphere evolution during polar vortex intensification. Journal of Geophysical Research: Atmospheres, 110(D24).

Limpasuvan, V., Thompson, D. W., and Hartmann, D. L. (2004). The life cycle of the Northern Hemisphere sudden stratospheric warmings. Journal of Climate, 17(13), 2584-2596

Lin, P., and Fu, Q. (2013). Changes in various branches of the Brewer–Dobson circulation from an ensemble of chemistry climate models. Journal of Geophysical Research: Atmospheres, 118(1), 73-84.

Madhu, V. (2016). Effects of Sudden Stratospheric Warming Events on the Distribution of Total Column Ozone over Polar and Middle Latitude Regions. Open Journal of Marine Science, 6(02), 302.

Manzini, E., Steil, B., Brühl, C., Giorgetta, M. A., and Krüger, K. (2003). A new interac-

tive chemistryclimate model: 2. Sensitivity of the middle atmosphere to ozone depletion and increase in greenhouse gases and implications for recent stratospheric cooling. Journal of Geophysical Research: Atmospheres, 108(D14).

Manzini, E., Giorgetta, M. A., Esch, M., Kornblueh, L., and Roeckner, E. (2006). The influence of sea surface temperatures on the northern winter stratosphere: Ensemble simulations with the MAECHAM5 model. Journal of climate, 19(16), 3863-3881.

Marsh, D. R., Mills, M. J., Kinnison, D. E., Lamarque, J. F., Calvo, N., and Polvani, L. M. (2013). Climate change from 1850 to 2005 simulated in CESM1 (WACCM). Journal of Climate, 26(19), 7372-7391.

Matsuno, T. (1970). Vertical propagation of stationary planetary waves in the winter Northern Hemisphere. Journal of the atmospheric sciences, 27(6), 871-883.

——, (1971). A dynamical model of the stratospheric sudden warming. Journal of the Atmospheric Sciences, 28(8), 1479-1494.

Matthes, K., Langematz, U., Gray, L. L., Kodera, K., and Labitzke, K. (2004). Improved 11-year solar signal in the Freie Universität Berlin climate middle atmosphere model (FUB-CMAM). Journal of Geophysical Research: Atmospheres, 109(D6).

——, D. Marsh, R. Garcia, D. Kinnison, F. Sassi, and S. Walters (2010), Role of the QBO inmodulating the influence of the 11 year solar cycle on the atmosphere using constant forcings, J. Geophys. Res., 115(D18), D18,110, doi:10.1029/2009JD013020.

Maycock, A. C., and Hitchcock, P. (2015). Do split and displacement sudden stratospheric warmings have different annular mode signatures?. Geophysical Research Letters, 42(24).

134

McInturff, R. M. (1978). Stratospheric warmings: Synoptic, dynamic and general-circulation aspects.

McIntyre, M. E. (1982). How well do we understand the dynamics of stratospheric warmings?. Journal of the Meteorological Society of Japan. Ser. II, 60(1), 37-65.

——, and Palmer, T. N. (1983). Breaking planetary waves in the stratosphere. Nature, 305(5935), 593-600.

McLandress, C. (1998). On the importance of gravity waves in the middle atmosphere and their parameterization in general circulation models. Journal of Atmospheric and Solar-Terrestrial Physics, 60(14), 1357-1383.

——, and Shepherd, T. G. (2009a). Impact of climate change on stratospheric sudden warmings as simulated by the Canadian Middle Atmosphere Model. Journal of Climate, 22(20), 5449-5463.

——, and Shepherd, T. G. (2009b). Simulated anthropogenic changes in the Brewer–Dobson circulation, including its extension to high latitudes. Journal of Climate, 22(6), 1516-1540.

——, Shepherd, T. G., Polavarapu, S., and Beagley, S. R. (2012). Is missing orographic gravity wave drag near 60° S the cause of the stratospheric zonal wind biases in chemistry–climate models?. Journal of the Atmospheric Sciences, 69(3), 802-818.

Mitchell, D. M., Gray, L. J., and Charlton-Perez, A. J. (2011). The structure and evolution of the stratospheric vortex in response to natural forcings. Journal of Geophysical Research: Atmospheres, 116(D15).

Mitchell, D. M., Gray, L. J., Anstey, J., Baldwin, M. P., and Charlton-Perez, A. J. (2013). The influence of stratospheric vortex displacements and splits on surface climate. Journal of Climate, 26(8), 2668-2682.

Nakagawa, K. I., and Yamazaki, K. (2006). What kind of stratospheric sudden warming propagates to the troposphere?. Geophysical research letters, 33(4).

Nishii, K., and Nakamura, H. (2004). Tropospheric influence on the diminished Antarctic ozone hole in September 2002. Geophysical research letters, 31(16).

Oberländer, S., Langematz, U., and Meul, S. (2013). Unraveling impact factors for future changes in the BrewerDobson circulation. Journal of Geophysical Research: Atmospheres, 118(18).

Omrani, N. E., Keenlyside, N. S., Bader, J., and Manzini, E. (2014). Stratosphere key for wintertime atmospheric response to warm Atlantic decadal conditions. Climate dynamics, 42(3-4), 649-663.

Palmer, T. N., Shutts, G. J., and Swinbank, R. (1986). Alleviation of a systematic westerly bias in general circulation and numerical weather prediction models through an orographic gravity wave drag parametrization. Quarterly Journal of the Royal Meteorological Society, 112(474), 1001-1039.

Palmeiro, F. M., Calvo, N., and Garcia, R. R. (2014). Future changes in the Brewer–Dobson circulation under different greenhouse gas concentrations in WACCM4. Journal of the Atmospheric Sciences, 71(8), 2962-2975.

——, Barriopedro, D., García-Herrera, R., and Calvo, N. (2015). Comparing sudden stratospheric warming definitions in reanalysis data. Journal of Climate, 28(17), 6823-

——, Iza, M., Barriopedro, D., Calvo, N., and García-Herrera, R. (2017a). The complex behavior of El Niño winter 2015–2016. Geophysical Research Letters, 44(6), 2902-2910.

——, Garcia, R. R., Calvo, N. and , Barriopedro, D. (2017b) On how turbulent mountain stress influences the sudden stratospheric warming frequency in WACCM. Journal of Climate, (submitted)

Pawson, S. (1997). Effects of gravity wave drag in the Berlin troposphere-stratosphere-mesosphere GCM. In Gravity Wave Processes (pp. 327-336). Springer, Berlin, Heidelberg.

Plumb, R. A. (2002). Stratospheric transport. Journal of the Meteorological Society of Japan. Ser. II, 80(4B), 793-809

Polvani, L. M., and Waugh, D. W. (2004). Upward wave activity flux as a precursor to extreme stratospheric events and subsequent anomalous surface weather regimes. Journal of climate, 17(18), 3548-3554.

Ray, E. A., Moore, F. L., Rosenlof, K. H., Davis, S. M., Boenisch, H., Morgenstern, O., ... and Manzini, E. (2010). Evidence for changes in stratospheric transport and mixing over the past three decades based on multiple data sets and tropical leaky pipe analysis. Journal of Geophysical Research: Atmospheres, 115(D21).

Richter, J. H., Sassi, F., and Garcia, R. R. (2010). Toward a physically based gravity wave source parameterization in a general circulation model. Journal of the Atmospheric Sciences, 67(1), 136-156.

——, Matthes, K., Calvo, N., and Gray, L. J. (2011). Influence of the quasi-biennial oscillation and El Niño–Southern Oscillation on the frequency of sudden stratospheric warmings. Journal of Geophysical Research: Atmospheres, 116(D20).

Rienecker, M. M., Suarez, M. J., Gelaro, R., Todling, R., Bacmeister, J., Liu, E., ... and Bloom, S. (2011). MERRA: NASA's modern-era retrospective analysis for research and applications. Journal of climate, 24(14), 3624-3648.

Robock, A., and Mao, J. (1995). The volcanic signal in surface temperature observations. Journal of Climate, 8(5), 1086-1103.

Roff, G., Thompson, D. W., and Hendon, H. (2011). Does increasing model stratospheric resolution improve extendedrange forecast skill?. Geophysical Research Letters, 38(5).

Scheffler, G., and Pulido, M. (2015). Compensation between resolved and unresolved wave drag in the stratospheric final warmings of the southern hemisphere. Journal of the Atmospheric Sciences, 72(11), 4393-4411.

Scherhag, R., (1952). Die explosionsartige Stratosphdrenerwarmung des Spdtwinters 1951/52. Ber. Deut. Wetterdieustes, 6, 51–63.

Schmidt, U., and Khedim, A. (1991). In situ measurements of carbon dioxide in the winter Arctic vortex and at midlatitudes: An indicator of the 'age'of stratopheric air. Geophysical Research Letters, 18(4), 763-766.

Schoeberl, M. R., and Hartmann, D. L. (1991). The dynamics of the stratospheric polar vortex and its relation to springtime ozone depletions. Science, 251(4989), 46-53.

Scott, R. K., Dritschel, D. G., Polvani, L. M., and Waugh, D. W. (2004). Enhancement of

Rossby wave breaking by steep potential vorticity gradients in the winter stratosphere. Journal of the atmospheric sciences, 61(8), 904-918.

Seviour, W. J., Butchart, N., and Hardiman, S. C. (2012). The Brewer–Dobson circulation inferred from ERA-Interim. Quarterly Journal of the Royal Meteorological Society, 138(665), 878-888.

Shaw, T. A., and Perlwitz, J. (2013). The life cycle of Northern Hemisphere downward wave coupling between the stratosphere and troposphere. Journal of climate, 26(5), 1745-1763.

Shepherd, T. G. (1990). Symmetries, conservation laws, and Hamiltonian structure in geophysical fluid dynamics. Advances in Geophysics, 32, 287-338.

——, (2002). Issues in stratosphere-troposphere coupling. Journal of the Meteorological Society of Japan. Ser. II, 80(4B), 769-792.

——, (2007). Transport in the middle atmosphere. Journal of the Meteorological Society of Japan. Ser. II, 85, 165-191.

Sigmond, M., and Scinocca, J. F. (2010). The influence of the basic state on the Northern Hemisphere circulation response to climate change. Journal of Climate, 23(6), 1434-1446.

——, J. F. Scinocca, V. V. Kharin, and T. G. Shepherd, 2013: Enhanced seasonal forecast skill following stratospheric sudden warmings. Nat. Geosci., 6, 98–102, doi:10.1038/ngeo1698.

Solomon, S. (1999). Stratospheric ozone depletion: A review of concepts and history. Reviews of Geophysics, 37(3), 275-316.

Stiller, G. P., Clarmann, T. V., Haenel, F., Funke, B., Glatthor, N., Grabowski, U., ... and López-Puertas, M. (2012). Observed temporal evolution of global mean age of stratospheric air for the 2002 to 2010 period. Atmospheric Chemistry and Physics, 12(7), 3311-3331.

Taguchi, M. (2011). Latitudinal extension of cooling and upwelling signals associated with stratospheric sudden warmings. Journal of the Meteorological Society of Japan. Ser. II, 89(5), 571-580.

Thompson, D. W., and Wallace, J. M. (1998). The Arctic Oscillation signature in the wintertime geopotential height and temperature fields. Geophysical research letters, 25(9), 1297-1300.

——, and Wallace, J. M. (2000). Annular modes in the extratropical circulation. Part I: Month-to-month variability. Journal of climate, 13(5), 1000-1016.

——, Furtado, J. C., and Shepherd, T. G. (2006). On the tropospheric response to anomalous stratospheric wave drag and radiative heating. Journal of the atmospheric sciences, 63(10), 2616-2629.

——, Solomon, S., Kushner, P. J., England, M. H., Grise, K. M., and Karoly, D. J. (2011). Signatures of the Antarctic ozone hole in Southern Hemisphere surface climate change. Nature Geoscience, 4(11), 741.

Uppala, S. M., Kållberg, P. W., Simmons, A. J., Andrae, U., Bechtold, V. D., Fiorino, M., ... and Li, X. (2005). The ERA40 reanalysis. Quarterly Journal of the royal meteorological society, 131(612), 2961-3012.

Van der Leun, J., Tang, X., and Tevini, M. (1995). Environmental effects of ozone deple-

tion: 1994 assessment. AMBIO-STOCKHOLM-, 24, 138-138.

Van Loon, H., Jenne, R. L., and Labitzke, K. (1973). Zonal harmonic standing waves. Journal of Geophysical Research, 78(21), 4463-4471.

——, and Labitzke, K. (1987). The Southern Oscillation. Part V: The anomalies in the lower stratosphere of the Northern Hemisphere in winter and a comparison with the quasi-biennial oscillation. Monthly Weather Review, 115(2), 357-369.

Waugh, D. W., and Polvani, L. M. (2010). Stratospheric polar vortices. The Stratosphere: Dynamics, Transport, and Chemistry, Geophys. Monogr. Ser, 190, 43-57.

Webster, S., Brown, A. R., Cameron, D. R., and Jones, C. P. (2003). Improvements to the representation of orography in the Met Office Unified Model. Quarterly Journal of the Royal Meteorological Society, 129(591), 1989-2010.

Wexler, H. (1959): The Antarctic convergence or divergence. The Atmosphere and Sea in Motion (Rossby Memorial Volume), 107-120.

Yamashita, C., Liu, H. L., and Chu, X. (2010). Gravity wave variations during the 2009 stratospheric sudden warming as revealed by ECMWFT799 and observations. Geophysical Research Letters, 37(22).